

Feedback Controlled Deformable Membrane Micropumps for Fluidic Delivery Applications

By:

MATTHEW L. CANTWELL

B.S., Mechanical Engineering, University of Illinois at Chicago, 2008

B.S., Electrical Engineering, University of Illinois at Chicago, 2008

THESIS

Submitted as partial fulfillment of the requirements
for the degree of Doctor of Philosophy in Mechanical
Engineering in the Graduate College of the
University of Illinois at Chicago, 2013

Chicago, Illinois

Defense Committee:

Dr. Farid Amirouche, Chair and Advisor

Dr. Michael Scott, Mechanical Engineering

Dr. Vitali Metlushko, Electrical Engineering

Dr. Michael Stroschio, Electrical Engineering

Dr. Elisa Budyn, Mechanical Engineering

Acknowledgements

I would like to acknowledge several people for helping me complete my doctoral research. Foremost, I would like to thank my advisor, Dr. Farid Amirouche, for his patience, motivation and continued support throughout my research work. Without his support this dissertation would not have been possible.

My sincere thanks are also extended to the members of my thesis committee: Dr. Michael Scott, Dr. Vitali Metlushko, Dr. Michael Stroschio, and Dr. Elisa Budyn for their support and assistance. I am honored to have been accepted by a panel of such distinguished scholars and scientists and humbled by their willingness to set aside time on my behalf.

Last but not least, I would like to thank my parents and family for kindling my dreams and passions for engineering and scientific study. Specifically, I would like to thank my father for his continued patience and efforts throughout my life in answering all of my engineering questions and helping to always point me in the right direction for continued success; and my mother for her constant love, support, and aid in all ways possible.

MLC

Table of Contents

Acknowledgements.....	ii
Table of Contents.....	iii
List of Tables.....	vii
List of Figures.....	viii
Summary.....	xi
CHAPTER 1 - Introduction and Background Study.....	1
Objectives and Motivation.....	1
Thesis Organization.....	3
CHAPTER 2 - Literature Review.....	5
Applications and Classifications.....	5
Actuation.....	6
Chamber Configuration.....	7
Two-chamber.....	8
Three-chamber.....	10
Summary.....	12
PART I.....	14
CHAPTER 3 - Concept, Modeling, and Design Optimization.....	15
Mathematical Model.....	15

Electromagnetic Actuation Challenges	18
FEM Magnetic Model	19
Enhancements and Optimizations	23
Pump Chamber Design.....	24
CHAPTER 4 – Prototype v1.0, Results, Analysis, and Discussion.....	27
Valve design.....	28
Membrane issues	29
Smaller More Accurate Volumetric Deliveries.....	30
PART II.....	33
CHAPTER 5 – Prototype v2.0 Open-Loop Results and Discussion	34
Design Overview and enhanced features of Micropump v2.0	34
Pump Architecture and Principles of Operation.....	35
Design Principles.....	36
Membrane	38
Magnets	39
Electromagnetic Coils.....	40
Valves	41
Free-Floating Membrane Valve Design.....	41
Device Operation.....	42
Physical Description	44

Membrane selection and analysis.....	45
Objectives	45
Materials	46
Device	46
Protocol.....	46
Results	48
Fabrication.....	56
Pump Body and Clamshell	57
Check Valves.....	57
Electromagnetic Coils.....	57
Electronic Driver Circuit	58
Assembly	58
Results and characterization.....	59
CHAPTER 6 – Closed-Loop Sensing and Control.....	64
Methods and Design.....	64
Electronics	65
Hardware	67
Sensing Principle from Theoretical Study	67
Laboratory Verification of Sensing Principles	71
Control Principle	75

Electromagnetic Noise Suppression	76
Determination of Position.....	81
Control Implementation.....	86
Results and limitations	88
Unloaded System Response.....	88
Loaded System Response	89
Discussion and Limitations	93
CHAPTER 7 – Future Work.....	97
Reduced Scale Pump.....	97
Prototype, Results and Discussion	98
Valve Scaling Issues.....	100
Machining Burrs	101
Valve Membrane Stiction.....	102
Valve Scaling Conclusion	102
Acknowledgement.....	102
Bibliography	104

List of Tables

Table 1 - Material properties of selected membranes.	39
Table 2 - Material properties of selected membranes.	46
Table 3 - Reproducibility data for a fixed drive current.	48
Table 4 - Reproducibility data for a fixed drive frequency.	49
Table 5 - Fluid pressure as a function of drive current.	53
Table 6 - Maximum strain attained during the deformation of the selected membranes.	55
Table 7 - Comparison of selected parameters for each membrane tested.	55
Table 8 - The current and power consumption of each membrane for selected flow rates.	56
Table 9- Fluid pressure as a function of drive current.	62
Table 10 - Summary: performances of Micropump v2.0.	63

List of Figures

Figure 1 - Diagram of a reciprocating electromagnetically actuated pump.....	20
Figure 2 - Magnetic field lines for an electromagnet and permanent magnet of identical geometry.	21
Figure 3 - FEM depiction of the interaction between an electromagnet and permanent magnet.	22
Figure 4 – Magnetic distance versus force results.	23
Figure 5 - FEM simulation derived force results for a dual coil pump.....	24
Figure 6 - Diagram of proposed pump chamber design.	25
Figure 7 - Assembled and exploded view of the Micropump v1.0 prototype.	27
Figure 8 - Micropump v1.0 with evaluation check valve assembly.	28
Figure 9 - FEM depiction of the membrane stress and deformation for Micropump v1.0.....	30
Figure 10 - Exploded view of proposed Micropump v2.0 prototype.	34
Figure 11 - Operational principles of the micropump.	36
Figure 12 - Architectural principles of the micropump: Two separate parts for low-cost disposable use.	36
Figure 13 - Fabricated and tested ball and slider style valves.	42
Figure 14 - Diagram and operating principle of a membrane based check valve.....	43
Figure 15 - Discrete check valve components and assembly.	44
Figure 16 - The experimental results of five consecutive hysteresis measurements performed on the same membrane.....	49
Figure 17 - The experimental results of Flow rate vs. Frequency trials for each of the four membranes tested (200mA per coil).	50
Figure 18 - The experimentally determined volumetric flow rate vs. drive current.	51

Figure 19 - The experimentally determined hysteresis curves for each of the membranes tested.	52
Figure 20 - The experimentally determined volumetric flow rate vs. power consumption.....	53
Figure 21 - Strain distribution inside the membrane at maximum deformation.....	54
Figure 22 - Electronic driver printed circuit board.	58
Figure 23 - Complete micropump and clamshell with all parts assembled.	59
Figure 24 - The experimental results of flow rate vs. frequency trials for each of the membranes tested (200mA per coil).	61
Figure 25 - The experimentally determined volumetric flow rate vs. drive current.....	61
Figure 26 - The experimentally determined hysteresis curves for each of the top performing membranes tested.....	62
Figure 27 - Laboratory test setup.....	63
Figure 28 - Schematic of custom electronic driver circuit.....	67
Figure 29 - The sensor location has been selected for an optimized signal to noise ratio. In this orientation, the sensor is only sensitive to the Br component of the magnetic field.	68
Figure 30 - Cartography around the pump depicting the magnitude of Br created by the coils...	69
Figure 31 - Cartography around the pump depicting the magnitude of Br created by the magnets. In this particular sensor location, Br(coil) is negligible and Br(magnet) is maximized.	69
Figure 32 - Graphical depiction of the theory of applied sensing principles.....	70
Figure 33 - Effect of the magnetic perturbation of the coils on the sensor measurement for a sensor located at the side location (red) vs. a centered classical symmetrical location (blue).	71
Figure 34 - Magnetic field as a function of the position of the magnet for a sensor located at the side location (red) vs. a centered classical symmetrical location (blue).....	72

Figure 35 - Measurement of the magnetic perturbation due to the coils with the sensor being at side location.	74
Figure 36 - Measurement of the magnetic field resulting from the displacement of the armature magnets, with the sensor positioned at the theoretically idealized location.	75
Figure 37 - Sensor response to voltage/current pulses.....	80
Figure 38 - Measurement of the electromagnetic coil perturbation using three different techniques.	81
Figure 39 - The experimentally measured magnetic field as a function of the position of the magnets; compared with the simulation, the corrected simulation, and the real-time sensing system results.	85
Figure 40 - The experimentally determined mechanical hysteresis as compared to the simulated function model.	86
Figure 41 - Flow chart of the sensing and control strategy.....	87
Figure 42 - Controller performances (blue) evaluated for a variety of classical set-point progressions (red).....	89
Figure 43 - Micropump v2.0 pumping distilled water.....	90
Figure 44 - Pump response to various ramp commands while pumping distilled water.	91
Figure 45 - Pump response to step commands while pumping distilled water.....	92
Figure 46 - Comparison of design between Micropump v2.0 and Micropump v2.1.....	98
Figure 47 - Photograph of Micropump v2.1 prototype.....	99
Figure 48 - Flow rate as a function of excitation frequency for the Micropump v2.1 prototype.	100
Figure 49 – 40x magnified view of a micro-machined valve used in Micropump v2.1.....	101

Summary

In recent years, there has been a surge in studies conducted to explore a multitude of micropump technologies [1]. This trend has been motivated in part by the introduction of a broad range of modern, technologically advanced engineering systems which require the manipulation of fluid volumes on the order of one milliliter and below [2]. Despite these efforts, gaps of knowledge still exist as to how one can accurately control pump dynamics to obtain sub-stroke volumetric deliveries, how to determine the membrane or flexible disc which is optimally suited for a reciprocating micropump, how to effectively mitigate the pulsatile nature of fluidic flows generated by reciprocating micropumps, or even how to efficiently reduce the scale of electromagnetic drivers (the most common and time-proven actuation scheme for macroscopic pumps).

This lack of knowledge can largely be attributed to the absence of even a single pump model which can both accurately and broadly simulate the operation of a micropump as a whole. The difficulty of obtaining such model lies in the complexity of interactions between several types of mechanics; including electromechanical forces, solid mechanics, and fluid mechanics. To this end, a compressive study is proposed to fill the previously discussed “gaps in knowledge”. With the majority of today's reported micropumps being reciprocating in nature [2], the greatest impact will be obtained through the enhancement of these technologies and therefore the focus of the study will be directed towards this class of micropumps. More specifically, electromagnetically actuated reciprocating pumps will be studied. The explicit intentions as well as the specific steps proposed to accomplish these goals are outlined below.

Reciprocating micropumps typically consist of an armature which operates between two distal extremes, often the walls of the pump chamber. The system is driven without feedback

and as a consequence will deliver a minimum fluid volume consisting of the fluid displaced by a single stroke. To enhance the accuracy, precision, and minimum deliverable volume of a reciprocating micropump, a method of accurate armature position sensing was devised and incorporated into a prototype. The effects of implementing a closed-loop feedback system using position sensing elements such that the armature can be commanded to multiple discrete locations between the pump chamber walls was investigated and is discussed. The sensors real-time armature position signal is fed into an embedded proportional-integral-differential feedback control system; a lab prototype has been tested to demonstrate the system's performance.

A key component of any diaphragm based reciprocating pump is the design and material composition of the membrane. It is well established that a thinner more elastic membrane reduces the force overhead of moving the armature and therefore reduces time averaged power consumption. Unfortunately, an overly elastic pump membrane results in excessive bowing of the exposed membrane surfaces which reduces accuracy of the delivered fluid volume. These conflicting requirements provide a complex multiphysics problem which is well suited for a computer based FEM model analysis and validation through laboratory testing. The membrane research focused on four key design goals addressed as follows: First, a membrane made of latex was tested and characterized along with potential substitutes. Second, an investigation was conducted using the identified membrane design characteristics and an FEM computer model was developed to obtain an optimized solution. Third, based on the optimized solution, a set of four "ideal" membranes were obtained and tested in a prototype pumping mechanism to evaluate performance. Finally, membranes with biocompatible materials were selected for potential medical use.

Reciprocating actuation solves a great number of problems associated with the scaling and complexity of other actuation schemes and offers an elegant simplicity of operation. However, reciprocating actuation also introduces a pulsed output flow which can be detrimental to certain delivery applications. To address this issue, work has been performed using fluid capacitors [3]; however these solutions suffer from frequency and backpressure dependencies. In this thesis research, we investigate the effects of implementing a dual chamber design to mitigate pulsatile effects while eliminating the dependencies on operating frequency and backpressures experienced previously. A dual chamber prototype was produced and the selected membranes were tested to evaluate the extent of attainable flow continuity.

Magnetically actuated reciprocating micropumps suffer from lower armature forces due to a greater air gap in the magnetic circuit as compared to their rotary counterparts. In the past, armature forces have typically been addressed by physically reducing the magnetic gap at the expense of stroke length. A study was conducted to alleviate these restrictions by introducing a twin opposed electromagnetic drive mechanism to boost armature force and increase stroke length. Furthermore, in membrane based reciprocating micropumps the surface of the magnetic armature is in direct contact with the fluid, as a result, the pressure generated is a function of both the surface area and the force imparted on the armature. This limits the maximum achievable pressure for a given attainable electromagnetic flux density. An appropriate FEM model was developed to investigate the effects of the armature magnets size to ultimately optimize the system in an effort to reduce the scale and overall physical size of the pump without sacrificing performance.

With the vast majority of micropumps being reciprocating in nature [2], this study provides a systematic approach to addressing a microfluidic problem which has a broader

interest. The implemented deformable membrane feedback control system allows for the potential development of smaller more efficient pumps which needs to be further explored.

CHAPTER 1 - Introduction and Background Study

This chapter provides a background and introduction to previous work with micropumps and outlines the objectives and motivation behind this research. An outline of the organization of this thesis is presented categorizing the parts and chapters contained in this document as well as a brief summary of each.

Objectives and Motivation

The inability of current pump models to broadly and accurately simulate the operation of a micropump as a whole has led to a large range of optimization problems which have proven difficult, costly, or even impossible to solve by other methods. Furthermore, while the majority of reported micropumps are reciprocating in nature [2], effective methods for aiding in the design and optimization process of several important pump characteristics are still non-existent. For instance, accurate control of micropump armatures for delivering sub-stroke volumes, selection of optimal reciprocating pump membranes, effective design strategies for mitigating pulsatile effects, and efficient methods for reducing the scale of electromagnetic actuation systems are still unknown.

Despite being a critical component of the vast majority of reciprocating micropumps, the material and geometric shape of the membrane or flexible disc used for actuation is often selected and then tested through trial and error, or worse yet, selected out of convenience favoring some fabrication process. The elasticity of a membrane can have a strong effect on the effort required to displace the pump armature and as a result, a thinner more elastic membrane reduces the force overhead of moving the armature and therefore reduces time averaged power consumption. Unfortunately, an overly elastic pump membrane results in excessive bowing of

the exposed membrane surfaces which reduces accuracy of the delivered fluid volume. These conflicting requirements provide a complex problem set which is well suited for a computer based FEM model and subsequent real-world testing. The objective is therefore to create an FEM model which can simulate these complex interactions to yield a set of geometric and material characteristics which define an ideal membrane for a given application. A set of real-world materials which best approximate the simulation results will subsequently be fabricated and tested in laboratory prototypes to confirm the validity of the findings.

Virtually all of the reported reciprocating micropumps operate by actuating an armature between two distal walls of a pump chamber. The resulting pulsatile flow is therefore delivered in increments of single-stroke volumes. The obtainable accuracy, precision, and minimum deliverable volume can therefore be enhanced by developing a system which can detect and position the armature at discrete positions between the pump chamber walls. A proposed research objective is to design and implement a real-time closed-loop feedback control system to accomplish these goals. A laboratory prototype implementing this system will be fabricated and the entire micropump will be tested to prove the systems performance and ability to accurately deliver sub-stroke volumes.

Another objective is to overcome some of the challenges previously encountered using electromagnetic actuation. Rotary motion designs typically require motors and gear trains which increase the complexity, size, noise and reduce accuracy. Electromagnetic linear drive systems overcome these limitations but introduce a new set of their own such as pulsed fluidic deliveries and reduced armature forces due to a greater air gap in the magnetic circuit. Efforts have been made to reduce the pulsatile effects of reciprocating pumps by introducing fluid capacitors [3] however these solutions suffer from frequency and backpressure dependencies. Armature forces

have also been addressed, typically by physically reducing the gap at the expense of stroke length. In the proposed work, I intend to investigate the effects of implementing a dual chamber design to mitigate pulsatile effects while eliminating the dependencies on operating frequency and backpressures experienced by others. Furthermore, I propose the study and subsequent implementation of a twin opposed electromagnetic drive mechanism which I postulate will boost armature forces while allowing for increased stroke lengths.

Thesis Organization

This thesis is organized into seven chapters covering the following topics:

- **Chapter 1** provides a background and introduction to previous work with micropumps and outlines the motivation for this research.
- **Chapter 2** presents a detailed review of current micropump technologies and actuation schemes.
- **PART I** contains chapters three and four and focuses on the research, development, and testing as it relates to the first prototype “Micropump v1.0”.
- **Chapter 3** proposes the design of a novel electromagnetic actuation scheme for providing superior performance to existing technologies. A conceptual design is discussed and a mathematical as well as computer model is developed and presented.
- **Chapter 4** presents the design and fabrication of the first micropump prototype. Valve design and membrane issues are presented and discussed as well as proposed methods for producing smaller more accurate volumetric deliveries. Chapter 4 concludes with optimization and design recommendations for a next generation prototype.

- **PART II** contains chapters five through seven and focuses on the research, development, and testing as it relates to the second prototype “Micropump v2.0”.
- **Chapter 5** describes the testing performed on various pump membranes in an effort to characterize the effects of real world membranes on pump performance and presents the open-loop performance results of the second generation micropump prototype.
- **Chapter 6** presents a feedback control system implementation for precise pump operation. Methods and design as well as the results and limitations of such implementation are presented and discussed.
- **Chapter 7** presents future directions and further reduction in the scale and overall dimensions of the preceding prototype. Scaling, fabrication and operational issues are further discussed. Finally, a summary of this contribution is presented.

CHAPTER 2 - Literature Review

An overview of current research and development of micropump technologies is presented in this section with an emphasis on the advances over the past two decades. Working principles, actuation schemes, pump chamber configurations, performance characterization, physically realized size, and biocompatibility are reviewed and compared to recognize the advantages and limitations of each technology. Due to the nature of this report, reviewed systems which have limitations and characteristics that are deemed to possess irreconcilable attributes with respect to the research goals are excluded from further examination after mention.

Applications and Classifications

An increasing number of today's technologically advanced embedded systems require micropump mechanisms capable of handling small and precise volumes of fluids. The vast range of applications include drug delivery systems, blood transport and pressurization units, microelectronics cooling elements, μ TAS (Micro Total Analysis System) implementations, and even space exploration systems [2] [4] [5]. As one of the main components of these systems, micropumps are often the limiting factor for size, weight and cost [1]. To satisfy the demand for ever smaller and diversely capable micropumps, a large number of pumps have been designed and fabricated utilizing a variety of different technologies [2] [1] [6].

The vast majority of micropump designs may be roughly divided into two distinct groups: reciprocating based micropumps and continuous flow micropumps [6]. Reciprocating micropumps employ pistons or diaphragms. Piston pumps are commonly employed in macroscale reciprocating displacement pumps however difficulties with scaling and complexity have prevented their use in micropumps. Diaphragm pumps on the other hand which utilize a thin membrane or deformable plate form the vast majority of all micropumps produced [2].

Continuous flow micropumps utilize the direct transfer of energy to obtain dynamic operation and employ either centrifugal, electro- or magneto-kinetic actuation techniques [1] [7]. Selecting the most desirable pump is a choice which depends largely on the specific requirements of the application. For example, for high flow rate applications, it is desirable to use a large force and long displacement external actuator, however, this type of pump selection typically requires the sacrifice of size at the same time [7]. A great deal of research has therefore been conducted to try and increase the utility of a given class of micropumps without sacrificing performance.

Actuation

All micropump technologies feature some form of actuation mechanism which provides the driving force for fluidic propulsion. An ideal actuator will have the following characteristics: large force, long stroke, fast response time, low power consumption, easily constructed, and exhibit high energy efficiency [8]. The numerous micropump actuation schemes which have been employed can be generally divided into two categories: mechanical and non-mechanical [9] [1]. Mechanical micropumps utilize a physical actuator to impart oscillatory or rotational forces on the working fluid while non-mechanical pumps directly transform certain types of available non-mechanical energy into kinetic momentum [1] [9]. Non-mechanical micropumps have scientific interest and are suited for a limited number of very specific applications but do not meet the intended broader impacts discussed in the project summary are therefore not discussed in great detail [7] [2].

The exclusion of non-mechanical actuation techniques does not severely limit the variety of pumps considered; indeed mechanical micropumps alone can be further subdivided into peristaltic micropumps, rotary micropumps, check-valve micropumps, valveless micropumps, ultrasonic micropumps and centrifugal micropumps [10] [11]. Furthermore, the actuation

systems which power these devices can be subdivided into electrostatic, piezoelectric, electromagnetic/magnetic, pneumatic, thermo-pneumatic, bimetallic, shape memory alloy, ionic conductive polymer film, and irreversible [1] [2] [9].

Bimetallic, shape memory alloy, ionic conductive polymer film, and irreversible actuation mechanisms have found use in only highly specific applications which seek a specific benefit provided by that actuation technology alone and therefore have a willingness to sacrifice other attributes such as attainable forces and pressures, efficiency, repeatability, and/or reusable use [9] [12] [13] [1]. While more versatile, the remaining actuation systems also possess their own unique set of characteristic advantages and limitations which are outlined as follows: Electrostatic actuation typically exhibits fast response times and low power consumption but suffers from very small developed forces and short attainable stroke lengths [14] [15]. Piezoelectric systems are characterized by large actuation forces and fast response times but typically require extremely high voltages for operation and deflect over very small distances [16] [17] [18]. Electromagnetic actuation systems typically produce large forces, large deflections, fast response times, and low power consumption, but are often accompanied by a large physical size reducing their ease of integration [19] [20] [21] [22]. Finally, reported systems which utilize thermal expansion exhibit comparatively mid-range force generation, mid-range deflections and low input voltages but have a slow response time and require a complicated fabrication process [23] [24].

Chamber Configuration

The design and configuration of fluidic pump chambers has been shown to significantly influence the pressure characteristics, stroke volume, bubble susceptibility, and nozzle-diffuser loss coefficients of a given micropump [7] [1]. The majority of early micropumps reported

possessed a single fluidic chamber and there have been a multitude of studies which implemented a wide range of geometric designs to optimize or enhance certain functional characteristics. Since then, attempts to further improve pump performance have adapted two and even three-pump-chamber configurations and have reported significant gains [7]. It should however be realized that performance benefits obtained by utilizing a multi-chamber configuration must be balanced against increases in size and complexity inherent to this approach [2]. A study conducted by Olsson *et al* suggests that two-chambered micropumps are particularly effective when used in conjunction with fixed-geometry valves [2] [25]. Other studies such as one conducted by Smits reveals the benefits of three-chambered pumps such as eliminating the need for flow rectifying valves [26]. A semi-comprehensive review covering a number of reported multi-chamber configurations as well as reported performance characteristics follows.

Two-chamber

In 1990, the first two-chamber micropumps were reported by Shoji *et al* [27]. Their micropumps utilized established piezoelectric actuation and passive check valve technologies; however, they were constructed such that performance evaluations could be made with the twin chambers connected in a series as well as a parallel configuration. A revelation ensued following their test results which reported effective operation at higher frequencies than similar single chambered devices as well as rippleless flow. In a series chambered configuration, the team achieved a maximum flow rate of 18 $\mu\text{l}/\text{min}$ and maximum pressure differential of 10.7 kPa operating at 25 Hz and 100 Volts while pumping water. The parallel configuration produced a flow of 42 $\mu\text{l}/\text{min}$ operating at 50 Hz and 100 Volts and was found to significantly reduce output flow oscillation due to periodic driver operation [27] [2].

Further work on two-chamber pumps was conducted by Olsson *et al* with publications released in 1995, 1996 and 1998 [28] [29] [30]. In the early research, Olsson and his team developed two-chamber four-diaphragm micropumps which operated in parallel with an individual driver attached to both the top and bottom surface of each chamber. The body was produced from a precision machined piece of brass and was manufactured to be planar. The resulting overall package size was 1.6 cm^3 and developed a maximum flow rate of 16 ml/min and a maximum pressure differential of 16.2 kPa operating at 540 Hz and 130 Volts. In later work, Olsson presented a first-in-class nozzle-diffuser based valveless micropump fabricated on a silicone substrate. In this design, the two chambers worked in parallel while being actuated 180° out of phase. He reports a maximum flow rate of 230 $\mu\text{l}/\text{min}$ and a maximum pressure differential of 16.7 kPa operating at 120 Volts while pumping water.

Yun *et al* reported in 2002 the design and fabrication of a reciprocating displacement micropump which operated utilizing a series, two-chamber configuration [31]. This pump was produced using microfabrication techniques and driven by surface-tension-induced motion of a mercury drop excited by electrowetting. Pumping water, the team achieved a maximum flow rate of 70 $\mu\text{l}/\text{min}$ and maximum pressure differential of 700 Pa operating at 25 Hz and 2.3 Volts while consuming about 170 μW of power. This equates to an overall estimated thermodynamic efficiency of 0.12%.

In 2003 Berg *et al* demonstrated the feasibility of a series connected two-chamber phase actuated design which operated without the use of check valves [32]. The pump utilized an external source of compressed nitrogen gas to provide the actuation energy. While this proof of concept design is of great academic interest, it is important to note that this design is only

considered suitable for low backpressure conditions where the available on-chip area or number of allowable external connections are limited.

Zordan and Amirouche reported in 2007 the design and fabrication of a superimposed two-chamber parallel-connected micropump [33]. The two chambers are separated by a membrane which bends to alternately place each chamber into compression or expansion mode. The overall package size of the prototype was reported as $22 \times 22 \times 6 \text{ mm}^3$ and developed a maximum flow rate of 135 ml/min and a maximum pressure differential of 650 Pa while consuming about 3 Watts of power. They also report that the two-chambered design provides a 140 percent increase in maximum flow rate as compared to a single chamber design.

Three-chamber

Coincident to the timeline of the two-chamber designs, the first three-chamber micropump was also reported in 1990 but by an individual working at Boston University named Jan Smits [26]. Since then a number of other studies have been conducted on three-chambered pumps. Unlike the two-chamber designs which feature a range of different geometries, connection schemes, and operating principles, virtually all of the reported three-chamber designs are peristaltic in nature. Often the most distinguishing characteristic is therefore the actuation scheme employed which varies among the reported pumps to include practically all of the previously discussed actuation methods.

The pump introduced by Smits was powered using piezoelectric actuators [26]. Each of the three series connected chambers has its own independent piezoelectric element which drives the chambers diaphragm. Activating the set of three actuators 120 degrees out of phase results in a net flow through the pump and eliminates the requirement for rectifying valves. The overall package size of the prototype was reported as 1.5 cm^3 and developed a maximum flow rate of

100 $\mu\text{l}/\text{min}$ and a maximum pressure differential of 600 Pa while operating at 15 Hz and 100 Volts peak-to-peak.

In 2004 a magnetically driven three chamber peristaltic micropump was introduced by Pan *et al* [34]. The main pump body was fabricated from PDMS and contains three small permanent magnets (one in each chamber) arranged in alternating polarity. The actuation was accomplished by utilizing a small external DC motor with a radially magnetized shaft and mounted such that as the motor spins it creates a field of alternating magnetic polarity in the vicinity of the chamber magnets. This alternating change in magnetic field induces forces on the magnets which open and close each chamber out of phase with one another. The team reports a maximum flow rate of 24 $\mu\text{l}/\text{min}$ and a maximum pressure differential of 330 Pa operating at around 29 Hz and less than 1 Volt while consuming 11 mW of power.

Electrostatically actuated three-chamber pumps were reported in 2002 and 2007 by Teymoori *et al* [35] and Lin *et al* [36] respectively. The former was fabricated using microfabrication techniques and utilized an unsymmetrical rectangular driving voltage of 20V and frequency 125Hz. Laboratory test data was not reported however a claim is made that “simulation results indicate proper performance of the device for drug delivery”. The latter micropump consists of a series-connected three chamber architecture, with each chamber having its own compliant membrane. Laboratory results obtained from the manufactured prototype yielded a maximum flow rate of 1.66 nl/min and a maximum pressure differential of 1.35 kPa operating at around 140 Volts.

In 2006 Wang *et al* produced a pneumatic micropump from PDMS utilizing MEMS based fabrication techniques [37]. The design incorporates a serpentine shaped pneumatic channel which crosses the linear fluidic channel at three or more locations. Applying a pulsed

pressure through the serpentine channel causes a deflection in the thin membranes present at each of the intersections resulting in a net flow. The design also incorporates a novel embedded flow sensor which is useful for determining the real time flow rate through the device. The team reports a maximum flow rate of 7.3 $\mu\text{l}/\text{min}$ while operating at 9 Hz using an input of 20 psi of pneumatic pressure.

A series of thermopneumatically actuated micropumps were reported in 2009 by Yang *et al* [38]. The three chamber device works by actuating each chamber with a three phase 40% duty cycle driving current. This method was later extended to five and seven chambered similar devices. The overall package size of the three chamber prototype was reported as $16 \times 18 \times 5.5$ mm^3 and developed a maximum flow rate of 9.18 $\mu\text{l}/\text{min}$ and a maximum pressure differential of 397 Pa. The five and seven chamber devices exhibited modest reductions in flow rates and a 15 and 29 percent gain in maximum generated pressure differential respectively, as compared to the three chamber device.

Summary

A surprisingly large diversity of actuation technologies exist for powering micropumps. Selecting the optimal action scheme for a particular pump can be highly application dependent, however, some schemes exhibit a broader range of utility than others. Largely due to simplicity and scalability, the vast majority of reported micropumps are classified as reciprocating diaphragm pumps. In the early days, virtually all pumps in this class consisted of a single deformable membrane and pump chamber. To improve on these devices, researchers began to investigate the benefits of utilizing multi-chambered designs. A multitude of two-chamber designs were reported which featured a range of different geometries, connection schemes, and operating principles. Each of these devices reported significant gains over similar single

chamber based devices. The reviewed three-chamber peristaltic pumps have a major advantage of not requiring rectifying valves which reduces the pumps susceptibility to failure due to sticking or clogging of passive valves. Unfortunately, these pumps face several other major problems such as a significantly lower differential pressure generation, the continual risk of reverse leakage [7], flow rates which exhibit large fluctuations [36], and the ability to pump only a single liquid since the same fluid passes through each chamber.

PART I

Micropump v1.0

CHAPTER 3 - Concept, Modeling, and Design Optimization

The aim of this chapter is to outline the work which was conducted to develop mathematical and computer models capable of simulating pump operation and to describe further proposed research and development inspired by these models which is intended to achieve the objectives set forth in previous chapters. The complexity of the various problems is first laid out; the methods used or proposed to investigate solutions are subsequently presented.

Mathematical Model

To develop an optimized solution to the earlier stated objectives, a mathematical model of the system is created. This model is necessary in order to investigate and better understand the operation and dynamics of the system. To this end, we must relate the input of electric power to the output force or pressure developed. Due to the complexities of the interactions, the model is most readily derived by splitting the physical interactions into two categories, electromagnetics and fluid dynamics. Once derived, the overall system is modeled by coupling the two mathematical subsystems into an overall multiphysics solution. Finally, due to the complex geometries involved, many portions of the system are modeled in COMSOL and intensive use of computer aided finite element analysis is employed to arrive at a nontrivial and insightful solution set.

Since the surface of the magnetic armature is in direct contact with the fluid, the pressure generated will be a function of both the surface area and the force imparted on the armature. These limitations may be characterized by the equation:

$$F = p \pi \left(\frac{D_m}{2} + \frac{2}{L_s} \int_{\frac{D_m}{2}}^{\frac{D_c}{2}} f(r) dr \right)^2$$

where F is the force of the armature, p is the pressure, D_m is the diameter of the magnet, L_S is the stroke length, D_C is the chamber diameter, and $f(r)$ is a function which describes the geometry of the membrane in its fully deflected state [39] [40]. The expression within the parenthesis represents the effective radius of the free pumping surface.

The preceding equation is limited in validity to only free pumping surfaces with a constant effective radius. A more generalized derivation can be obtained by taking the double integral of a function which describes the geometry of the membrane in its fully deflected state as a function of θ in cylindrical coordinates, namely:

$$F = p \int_0^{2\pi} \int_0^r f(r, \theta) dr$$

Of course, either of the two preceding equations can be rearranged to express the pressure in terms of the force delivered to the armature. Furthermore, since the force developed can be related to the magnetic field strength, this limits the maximum achievable pressure for a given attainable electromagnetic flux density. In creating the magnetic models, it is noted that the system contains both permanent magnets and electromagnets. Typically, scientists dealing with permanent magnets calculate the magnetic field either from a derived form of the magnetic scalar potential or directly from Coulomb's law [41] [42]. The coulombian approach simplifies the model of the pumps cylindrical magnets to two charged planes S_1 (the positively charged source) and S_2 (the negatively charged source):

$$\vec{H}(\vec{r}) = \frac{J}{4\pi \mu_0} \iint_{S_1} \frac{1}{|\vec{r} - \vec{r}'|^2} ds_1 - \frac{J}{4\pi \mu_0} \iint_{S_2} \frac{1}{|\vec{r} - \vec{r}'|^2} ds_2$$

where \vec{r} is the position of the observation point and \vec{r}' is the position of the elementary source on the charged surface. [42] [41] [43] [44]. On the other hand, scientists dealing with

electromagnetic coils typically calculate the magnetic field from an amperian approach using the curl of the vector potential or directly from Biot-Savart's law:

$$\vec{B}(\vec{r}) = \frac{\mu_0}{4\pi} \iint_S \frac{\vec{K} \times (\vec{r} - \vec{r}')}{|\vec{r} - \vec{r}'|^3} ds$$

where \vec{K} is defined as \vec{j}/μ_0 [42] [41] [45]. Furthermore, it is to be understood that the H-field and B-field developed in the preceding to equations are related by $B = \mu_0(H + M)$ and therefore can be used to describe the same phenomena where H is termed the magnetic field intensity, B is termed the magnetic flux density, μ_0 is the magnetic permeability of free space and M is the magnetization vector field.

Nevertheless, it is important to understand that there is equivalence among all of the various source models, however some may lead more easily to analytical solutions than others [42] [41]. Furthermore, as described earlier, the force exerted on the permanent magnet as a result of the currents passed through the electromagnetic coil are related to the pressure. This force can be described analytically using the amperian model developed in this section and Lorentz's force:

$$\vec{F} = \iint_S (\vec{K}_b \times \vec{B}_a) ds$$

While a Lorentz force calculation is relatively easy to evaluate for simple models and geometric arrangements, more complex systems can lead to impossibly difficult derivations. Alternate methods do exist which utilize virtual work [46] [47], however a far more generalized approach which utilizes tensor arithmetic to simplify the computational cost is the Maxwell stress tensor. As a result, the Maxwell stress tensor is frequently employed throughout this research as a means of deriving forces resulting from electromagnetic interactions, it should be

noted however that evaluation of force models using the Maxwell stress tensor has its own set of challenges. These challenges and a developed set of modeling guidelines are discussed in great detail in sections which follow and careful adherence to these practices have nevertheless proven to yield accurate results. Formally, the Maxwell stress tensor may be defined as:

$$\vec{F} = \iint \left[\frac{1}{\mu_0} \vec{B}(\vec{B} \cdot \vec{n}) - \frac{1}{2\mu_0} B^2 \vec{n} \right] dS$$

where \vec{n} is the normal vector to the surface S and \vec{B} is the magnetic flux density [48].

I model the interaction between the permanent magnets and the electromagnetic coils using an amperian approach and utilize finite element analysis for the evaluation of each model. These forces are then coupled to the derived models which relate the armature force to output pressure allowing for the evaluation of the overall system effectiveness. The effort will be focused on obtaining smaller overall dimensions and a boost in efficiency to reduce energy consumption. Subsequent to this research, a newly developed conceptual pump prototype will be tested to evaluate the validity and performance of this study.

Electromagnetic Actuation Challenges

Research and development of electromagnetically actuated systems provide a host of challenges including: the development of accurate models which reflect a real-world degree of complexity, obtaining armature forces which scale to provide usable pump pressures, permeability losses, and heat generation which limits the current density of the coils. These constraints provide a set of challenging and in some instances conflicting requirements which need to be overcome through careful consideration, novel design, and a balance of tradeoffs to achieve the device objectives. An in depth study has therefore been undertaken in which appropriate FEM models were developed to investigate the effects of changing the parameters and geometry of the magnets

with the ultimate intent of optimizing the system to reduce the scale and overall physical size of the pump without sacrificing performance.

FEM Magnetic Model

While the forces and notion of magnetic interactions often feel intuitive from the days of youth playing with small permanent magnets, the complexities of developing accurate mathematical models of these seemingly magical devices escape all but the most cunning of intellectual imaginations. James Clerk Maxwell possessed one such imagination and through great discipline developed the equation which later was named the Maxwell stress tensor [48] [49]. Fortunately this equation, which was presented in the previous section, is both readily adaptable to finite element analysis as well as being general enough for the analysis of complex system geometries [50].

With all the glory of this method however, it is very important to note that the finite element approach to modeling Maxwell stress tensor problems are highly mesh dependent. With even the slightest loss of care in mesh generation, the stress tensor routinely returns force results which are both inaccurate and often entirely wrong in polarity. The implications of such methods are disastrous, however an applied understanding of their failure mechanisms allow for the valid implementation into these models. The fundamental shortfall of these inaccuracies resides in the fact that the Maxwell stress tensor is a surface analysis technique. The stress tensor approach integrates the divergence of the magnetic field along the surface boundaries to derive the force results [50] [51].

In a typical magnetic model, the resulting forces can be rather large on a given side of a magnetic domain, however these large values will often cancel out with nearly identical but opposite values on the opposing face. The result is an accumulation of classical floating point

numerical error (or loss of significance) from the subtraction of two large nearly identical numbers [52] [53]. As such, the mesh on opposing faces of a given magnet should be constructed with a high degree of regularity and symmetry.

An initial set of finite element models were created to mathematically evaluate the performance characteristics of a simple electromagnetically actuated reciprocating micropump. A two-dimensional representation of the basic structure of such a device is depicted in Figure 1. It is well established that the composition and nature of magnetic fields are independent of the source model, in fact a multitude of publications have been written solely to emphasize this fact [41] [42]. As a result, the first set of models were created to define the size and shape of the representative electromagnet and permanent magnet, however both were modeled as permanent magnets, defining only a remanent flux density within the domain. It should be immediately noted that while the resulting models provided an intuitively correct relationship between force and distance, the results later disagreed with real-world laboratory test results. The discrepancy was found to be a result of the real-world geometries of the modeled electromagnets and not the nature of the magnetic fields involved.

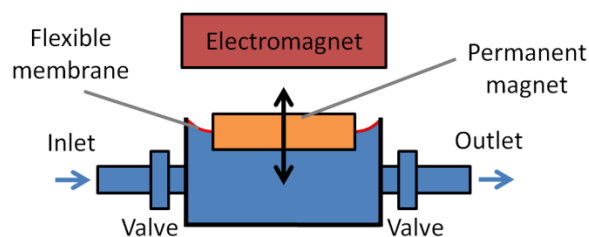


Figure 1 - Diagram of a reciprocating electromagnetically actuated pump.

Although the natures of the magnetic fields are identical regardless of the source model, the shape, flux density, and flux path may vary. This concept is illustrated in Figure 2 where the magnetic field lines are plotted for an electromagnet and permanent magnet of identical

geometry. The illustration is a cross-sectional view depicting a ring permanent magnet and an electromagnet coil. Further investigation reveals that the observed contradiction in magnetic flux direction near the center of the magnets can be eliminated by using a comparably sized permanent magnet with the center filled (a disc magnet). A distinction however extends even to this case, as the flux lines can return to any area of the permanent magnets polar surfaces while the flux lines are forced to the center in the case of an electromagnet. It has therefore been established that for these models where the magnets are in close proximity (i.e. gap distance is less than the diameter of the magnets), separate magnetic modeling techniques must be used for each type of magnet.

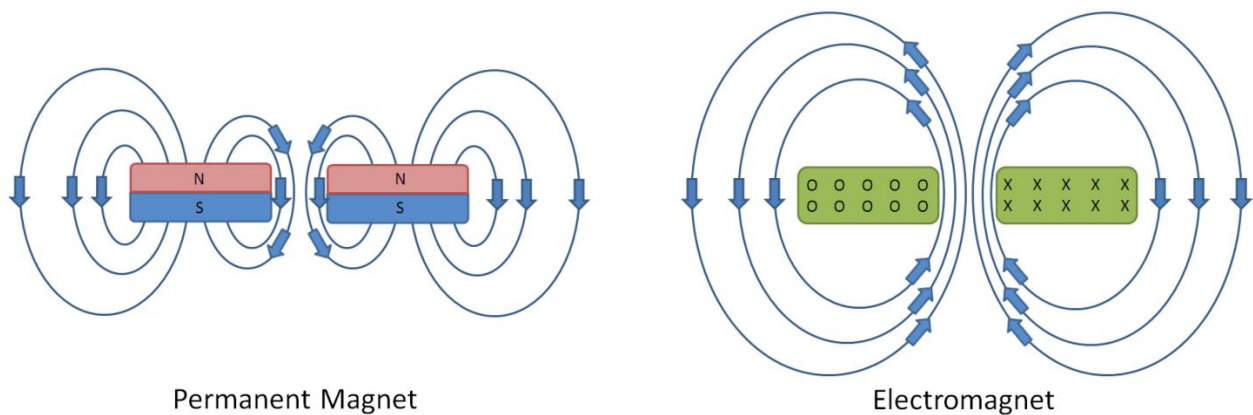


Figure 2 - Magnetic field lines for an electromagnet and permanent magnet of identical geometry.

Utilizing all of the techniques and strategies discussed in these sections, finite element magnetic interaction models were developed and simulated using COMSOL multiphysics to mimic the most basic interactions between the electromagnet and the permanent magnets. Since these models will form the basis for further complex modeling and simulation, it was necessary to thoroughly test the validity of the finite element results. To this end, a real-world experiment was set up and performed to evaluate the effectiveness and accuracy of the model. An example of the simulated interaction is depicted in Figure 3.

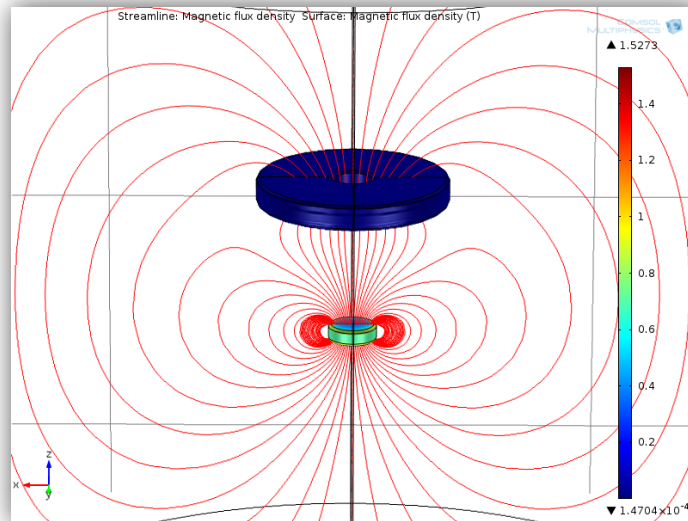


Figure 3 - FEM depiction of the interaction between an electromagnet and permanent magnet.

For the experimental testing, the electromagnet was positioned at an initial distance from the permanent magnet d_{\max} . The force imparted on the permanent magnet as a result of the energized electromagnet was then recorded. Subsequently, the electromagnet was moved a fixed distance Δd and another recording was made. This process was repeated for each Δd until the air gap between the electromagnet and the permanent magnet arrived at d_{\min} . The test setup consists of a piezoelectric based force gauge on which the permanent magnets are affixed through non-magnetic support. The supports separate the magnets from the force gauge a sufficient distance such that magnetic interactions are negligible and the supports were designed to be sufficiently stiff such that deflections in the support as a result of the forces generated could also be neglected. The electromagnet was suspended by a ridged but adjustable non-magnetic support structure which allowed for precise changes in the separation distance. The results obtained from both the COMSOL FEM simulations as well as the real-world experimental values are plotted below:

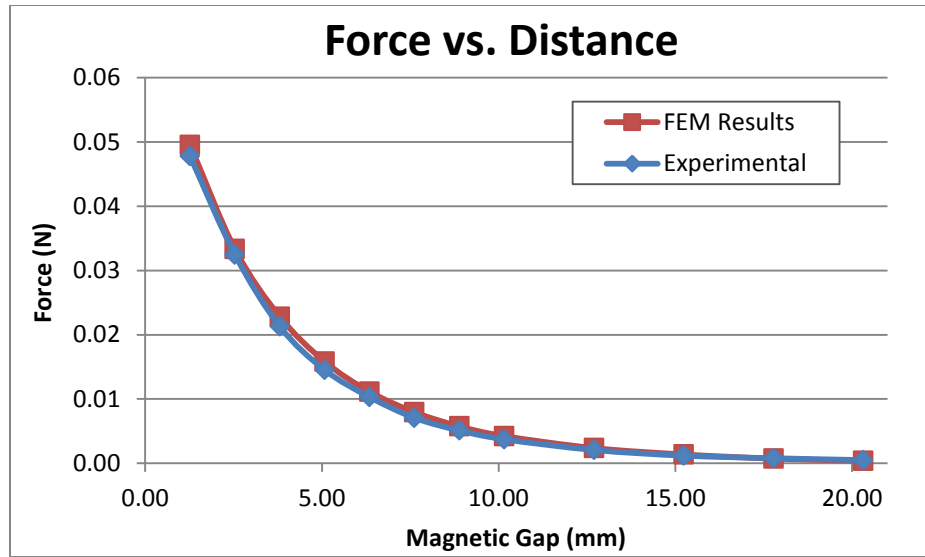


Figure 4 – Magnetic distance versus force results.

Enhancements and Optimizations

The excellent agreement between the simulated and experimental results reinforces the validity of the data and supports the observed exponential loss in armature force as a function of magnetic gap (see Figure 4). The desire to produce an efficient electromagnetically actuated pump with a large stroke length therefore yields conflicting requirements. It is proposed that this conflict may be reconciled through the novel implementation of a second, axially aligned and linearly displaced electromagnet with opposing polarization. Such a design should enjoy the benefits of a small gap under both attractive and repulsive conditions at each extreme of stroke length. The minimum force will therefore be encountered at the midpoint of the armatures stroke length which is a state that typically enjoys the benefits of dynamic equilibrium.

To confirm this hypothesis and quantify the expected benefits, another FEM model was created which included an additional electromagnet. The model also includes the addition of another permanent magnet which allows the two permanent magnets to sandwich the flexible membrane thereby becoming affixed without the need for adhesive. A diagram of the

components and relative orientation of the model is depicted in Figure 6. The results of the study are plotted below in Figure 5 which shows the force imparted on the armature as well as the relative force contributions of each electromagnet. The data strongly supports the hypothesis and suggests a staggering improvement in linear force distribution over single coil designs. An experimental prototype was proposed to test the real-world validity of such a device and is discussed in detail in *CHAPTER 4 – Prototype v1.0, Results, Analysis, and Discussion*.

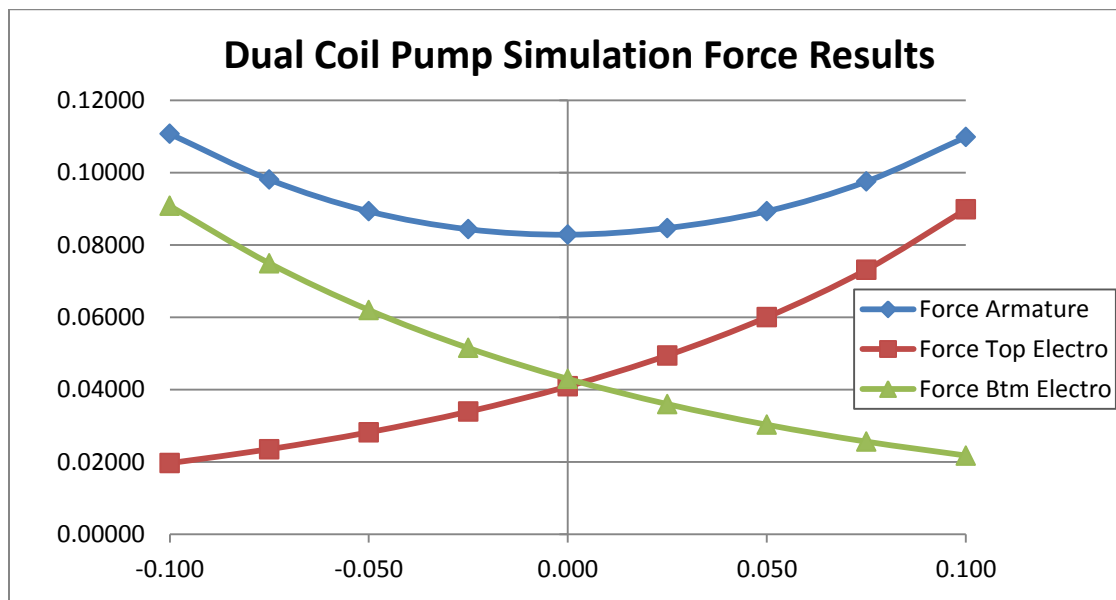


Figure 5 - FEM simulation derived force results for a dual coil pump.

Pump Chamber Design

As discussed earlier, to meet the stated objectives the preferred method of actuation will be electromagnetic. While many designs have been considered which utilize this method of actuation, the most suitable arrangements fall into the class of reciprocation based pumps. For high flow rate applications in a reciprocating pump design, it is proposed that we can better approximate a continuous flow by utilizing both sides of the pump membrane. This leads to a design which is effectively dual chambered. The advantages are two-fold, first as noted earlier

utilizing both sides of the membrane as a free pumping surfaces better approximates continuous flow as one side of the pump will always be in the exhaust stroke. Second, the membrane itself acts as a fluidic barrier between the two chambers allowing for the possibility of pumping two dissimilar fluids simultaneously without mixing. Furthermore, the pump chamber architecture has been tailored to incorporate the dual coil design proposed in the previous section to enhance the forces imparted upon the armature.

A diagram depicting the major elements and operation of the proposed pump chamber design is presented in Figure 6. The figure can be thought of as depicting the pump in its three distinct states of operation; from left to right, a.) the pump is depicted in its de-energized state with the membrane at rest and undeflected, b.) the pump has been energized producing a magnetic force which results in the upward movement of the magnets and membrane, c.) the pump has been energized in a reversed polarity producing a magnetic force which results in the downward movement of the magnets and membrane.

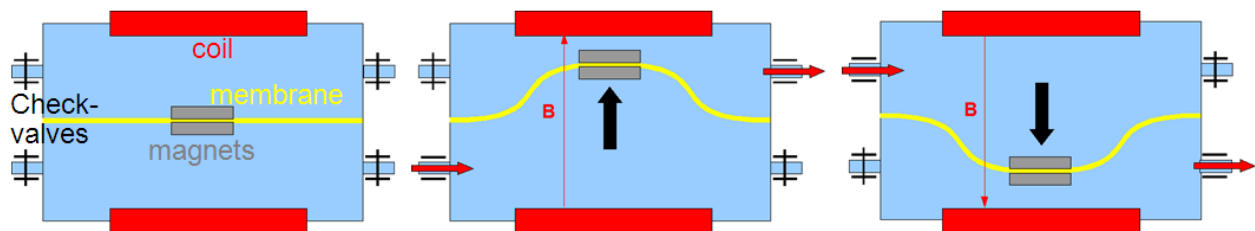


Figure 6 - Diagram of proposed pump chamber design.

In the initial unenergized state, the membrane and fluid within the pump chamber is at rest and all four check valves are in a closed position. However, the application of a current through the electromagnetic coils disrupts this balance as the magnets and membrane are driven upwards. The result of the displacement is an increase in pressure within the upper chamber and a decrease in pressure in the lower chamber. Since the check valve pair connected to each

chamber are affixed with opposing bias directions, the result of any pressure change results in unidirectional rectification. Therefore, as the armature magnets and membrane are driven upwards, the inlet valve of the upper chamber becomes strongly reverse biased preventing any fluid flow through the inlet while the outlet valve of the upper chamber becomes forward biased allowing the fluid to exit the chamber. At the same time, converse conditions exist in the lower chamber resulting in the outlet valve of the lower chamber becoming reverse biased preventing any fluid flow through the outlet while the inlet valve of the lower chamber becomes forward biased allowing fluid to enter the chamber.

Reversing the current which flows through the electromagnetic coils reverses the force vectors acting on the armature and membrane thereby reversing the states of check valves and direction of flow. This allows for both the exhaust and replenishment of fluid in each chamber over the period of one full cycle, or two strokes. Furthermore, during any point for which the armature and membrane are in motion, a fluid flow exists out of one of the two outlet ports. Theoretically this allows for the generation of a nearly continuous flow, halting velocity only for infinitesimally short periods of time required to reverse the direction of travel.

CHAPTER 4 – Prototype v1.0, Results, Analysis, and Discussion

A dual chambered, twin coil micropump prototype was fabricated to test the validity and functionality of the proposed actuation concept. The necessity for such prototype arises from the fact that although other electromagnetically actuated micropumps exist in literature, twin electromagnetic actuation in the context of micropumps has never before been validated. To alleviate the need for complex microfabrication techniques which have burdened previous designs with excessive cost and manufacturing time requirements, this pump has been designed to be manufacturable with traditional micromachining techniques. The design is a culmination of the research and innovation outlined in the previous sections. Its geometry and components are depicted in Figure 7 while a photograph of the actual device is depicted in Figure 8.

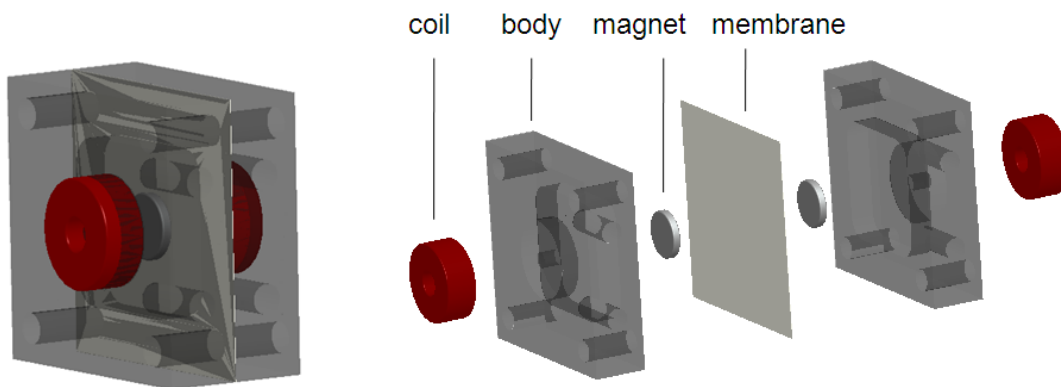


Figure 7 - Assembled and exploded view of the Micropump v1.0 prototype.

The prototype proved successful demonstrating that driving the electromagnets with an alternating current resulted in the expected deflection of the armature and membrane. While the actuation performed to a high level of satisfaction, rectifying the developed flow became an issue. The problem resides in the relatively high cracking pressures and large physical sizes of commercially available check valves. To address these issues, a valve study has been conducted and is presented next.

Valve design

As discussed in the previous section, commercial spring and poppet check valves proved to have cracking pressures which are much too high rendering them unusable. Automotive vacuum valves were found to have reasonable cracking pressures and therefore performed the task of rectification, however, these valves were physically too large and had a relatively high flow hysteresis. Ultimately it was deemed necessary to create a custom check valve which could simultaneously address each of these issues and arrive at an optimal design for this application.

A multitude of various valve designs were therefore conceived, fabricated and experimentally tested. Many of the designs worked but exhibited new problems as a result of their physical size such as stiction and reliability. The design which demonstrated a reasonably high level of performance when paired with this pump was a flap valve based design. The pump prototype and accompanying custom check valve housing are shown in Figure 8.

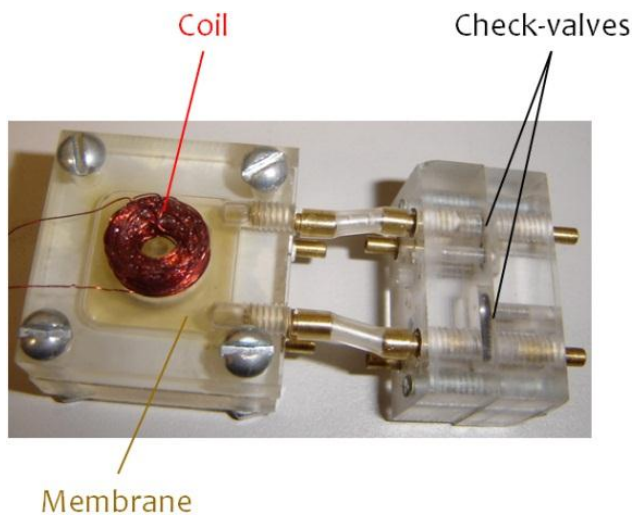


Figure 8 - Micropump v1.0 with evaluation check valve assembly.

While the miniature flap valve based designs provided a reasonably high level of performance, they also had some issues with sealing. A newly designed and tested valve has therefore been

produced which utilizes a free-floating membrane and rosette pattern of microchannels to eliminate these issues. This new design has been incorporated into the next generation of micropump which is discussed in PART II.

Membrane issues

A key component of any diaphragm based pump is the design and material composition of the membrane. This selection process is especially important for the micropumps presented where fluid contamination and performance are of paramount importance. It is well established that the membrane elasticity effects the ease of displacing the pump magnets and as a result, a thinner more elastic membrane reduces the force overhead of moving the armature and therefore reduces time averaged power consumption. Unfortunately, an overly elastic pump membrane results in excessive bowing of the exposed membrane surfaces which reduces accuracy of the delivered fluid volume. These conflicting requirements provide a complex problem set which is well suited for a computer based FEM model and subsequent real-world testing.

The proposed membrane research will focus on four key research goals. First, the current membrane will be tested and characterized to provide starting data for evaluating pump performance in the model. Second, an ideal set of geometric and material characteristics will be devised to minimize the bowing while maximizing elasticity. Third, an intensive investigation will be conducted utilizing the derived membrane characteristics and the FEM computer model to arrive at an optimization solution. Finally, a small set of real world material candidates will be selected which best approximate the “ideal” membranes. Using these materials, membranes will be fabricated and tested in the micropump prototype to fully characterize their performance.

Initial models and simulation have already revealed a desirable change in pump chamber geometry. The filleted square chamber configuration used in the Micropump v1.0 prototype was

designed to maximize displacement in a square package but was shown through simulation to result in uneven membrane stress distributions. These nonhomogeneous stresses result in membrane bulging which can lead to tilting of the armature. The change to a cylindrical pump chamber has therefore been proposed and included in the design for Micropump 2.0. An example of the simulated stress distribution and deformation is depicted in Figure 9.

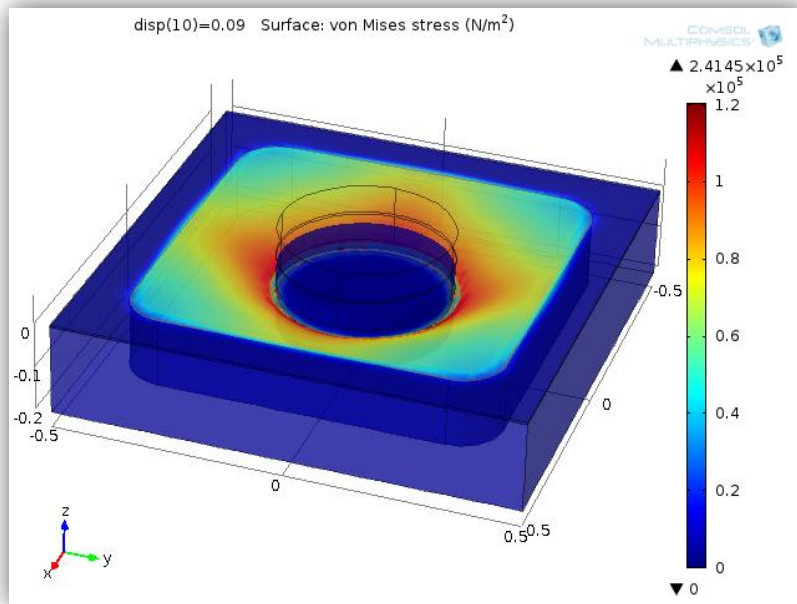


Figure 9 - FEM depiction of the membrane stress and deformation for Micropump v1.0.

Smaller More Accurate Volumetric Deliveries

To deliver smaller and more accurate volumetric deliveries, three improvements are proposed for the developed micropumps. First, the introduction of a feedback control system which would allow the delivery of sub-stroke volumes. Second, a reduction in the pump chamber diameter. Finally, smaller deliveries can be produced with a reduction in stroke length.

In the current prototype embodiments outlined in the previous sections, the pumps operate open-loop without the use of any type of positional armature feedback. As a

consequence, the magnet can only be controlled to traverse from one side of the pump chamber to the other, positions in between are unattainable. To achieve sub-stroke volumes, where the volume of a single stroke is defined as:

$$V_{Stroke} = L_s \left(1 - \frac{r^2}{R^2}\right)^2$$

where L_s is the center deflection of the membrane caused by the magnet, r is the radius of the magnet, and R is the radius of the membrane [39], a feedback system must be incorporated within the pump. A closed-loop feedback system using position sensing elements so that the membrane can be commanded to multiple additional discrete locations between the pump chamber walls will enhance the accuracy, precision, and minimum deliverable volume of the micropump. To this end, a method of accurate membrane position sensing will be devised and incorporated into a prototype. The resulting signal will be fed into an embedded proportional-integral-differential feedback control system, and the entire micropump will be tested to prove the systems validity and performance.

In both open and closed loop designs, a reduction of pump chamber diameter will improve the accuracy of small volumetric deliveries. In the open loop case a smaller pump chamber, and therefore a smaller free pumping surface, will invariably deliver a smaller volume for a given stroke length. In the closed loop case, a smaller pump chamber will result in a reduced output volume for a given step size (defined as the minimum resolvable length of motion). A study is therefore proposed which will investigate the effects of reducing the size of the armature magnets on the maximum producible pressure. A magnetic model will be simulated for a variety of smaller magnet diameters and lab testing will be performed to verify

the validity of the results. The goal will be to find the optimal size which will deliver minute fluid volumes while maximizing pressure and accuracy.

The final proposed design improvement is to reduce the overall stroke. The expected benefit of stroke length reduction is a twofold improvement in pump performance. First, it will result in a linear reduction of single stroke volumetric deliveries. Second, it will further reduce the magnetic gap which will boost output pressures.

PART II

Micropump v2.0

CHAPTER 5 – Prototype v2.0 Open-Loop Results and Discussion

This chapter presents the design optimizations and enhancements which follow from the study of Part I integrated into the next generation prototype “Micropump v2.0”. An extensive laboratory study which evaluates the performance of several different membranes compositions and thickness is also included. Finally the results and characterization of overall pump performance while operating in an open-loop configuration is discussed.

Design Overview and enhanced features of Micropump v2.0

The proposed next generation prototype is designed to build off the established foundation of the dual chambered, twin coil micropump prototype fabricated earlier. The new device promises further reductions in size and performance with integrated free-floating check valves, enhanced high-flow-rate armature magnets, magnetic gap reductions for improved pressure generation, and mitigated pulsatile effects due to the implementation of oversized flow channels to reduce fluidic drag. A conceptual rendering of the proposed prototype is depicted in Figure 10.

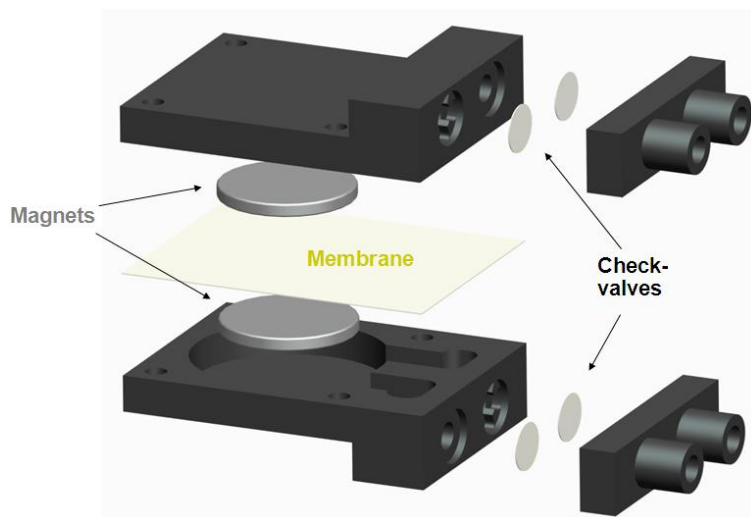


Figure 10 - Exploded view of proposed Micropump v2.0 prototype.

In addition to these benefits, the desired broader impacts of this research work can be furthered by noting that the use of non-contact electromagnetic actuation allows us to separate the pump into two distinct parts for disposable use. One part will be reusable and will contain the coils and electronics, while the other portion will be disposable and will house the inexpensive pump body and internal components therein.

Pump Architecture and Principles of Operation

The general pump operation is similar to the operation of the pump described in Part I. That is, the pump operates by electromagnetically driving the membrane magnets in a reciprocating motion within the pump body. As the magnets and consequently the membrane are displaced, a volumetric change occurs within the pumping chambers. This change in volume results in an increased pressure on one side of the membrane and simultaneously a pressure reduction on the other. These pressure fluctuations drive a set of passive check valves installed in each chamber. The check valves are installed so as to be directionally opposed, which results in a net flow. The high pressure side of the membrane forces the corresponding intake valve closed and drives the fluid through the forward biased outlet valve. At the same time, the low pressure side of the membrane forces the corresponding outlet valve closed and draws fluid in through the forward biased inlet valve. When the direction of the membrane is changed, the role of each chamber is reversed. Figure 11 and Figure 12 depict the architectural principles which have been selected for the micropump.

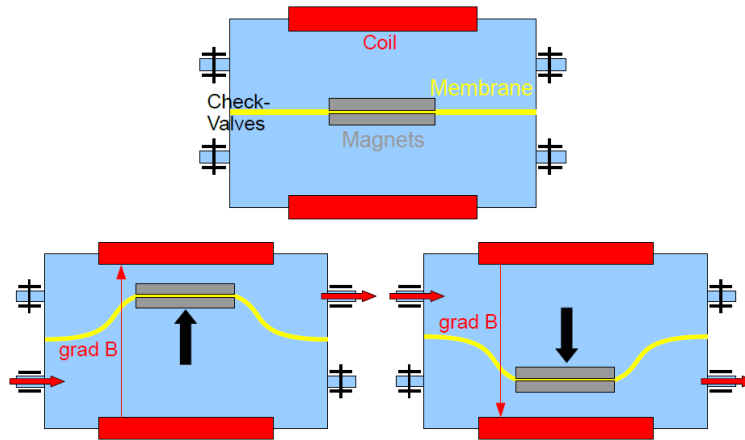


Figure 11 - Operational principles of the micropump.

Referring to Figure 11, the operational principles of the micropump can be summarized as follows: *Top*: Undeformed membrane in relaxed state; *Bottom left*: The pressure increase in the top chamber drives fluid out through the outlet valve while the pressure decrease in the bottom chamber draws fluid in; *Bottom right*: Operating conditions with the membrane motion reversed.

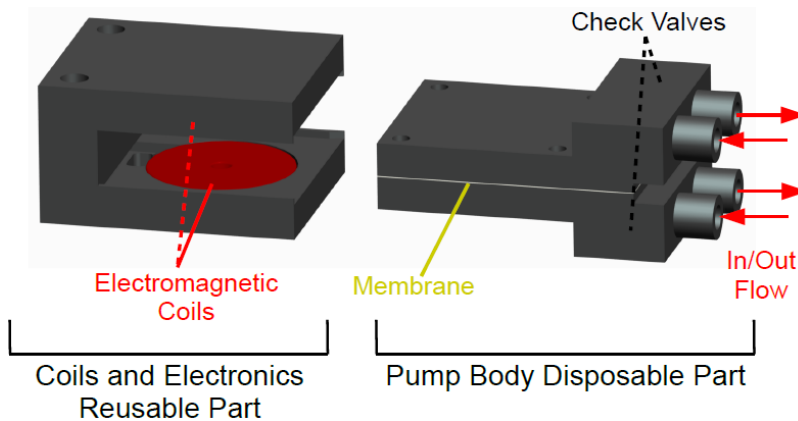


Figure 12 - Architectural principles of the micropump: Two separate parts for low-cost disposable use.

Design Principles

The design incorporates a membrane-based electromagnetic actuation system (Figure 11). Several micropumps already exist which operate based on similar principles [17] [2] [54], however, none of these have been engineered with a low-cost objective in mind. Nevertheless,

even in regards to the general architectural design, this concept is in many ways very different from what is typically encountered:

- *Double coils:* Two discrete electromagnetic coils are required. This arises from the fact that magnetic forces \mathbf{F} and torques Γ between a coil and a magnet are defined as:

$$\mathbf{F} = \int_{V_{mag}} \mathbf{M} \cdot [\mathit{grad}(\mathbf{B}_{ext})] dV$$

$$\Gamma = \int_{V_{mag}} \mathbf{M} \times \mathbf{B}_{ext} dV$$

where dV is an elementary volume of the total magnet volume V_{mag} . \mathbf{M} is the magnets volume magnetization: $\mathbf{M} = \mu_0 \mathbf{B}_{rem}$ where \mathbf{B}_{rem} is the remanent magnetic field inside the material. \mathbf{B}_{ext} is the external magnetic field (i.e. due to all possible sources except the magnet. In this case it represents the magnetic field due to the coils.)

The actuation force \mathbf{F} is usable only when the position of the magnet (facing the coil) is stabilized by the torque Γ (i.e. when \mathbf{B}_{ext} and \mathbf{M} have the same direction). Otherwise, the induced torque tends to flip the magnet. With two coils, the magnet will always be attracted by one of the coils and be drawn to it in a stable configuration. The use of two coils also significantly improves the efficiency of actuation (as discussed in Chapter 3).

- *Double chambers:* As the pump has two opposing coils, it is possible to use a double chambered architecture with the coils providing symmetric forces instead of the classical single-chamber configuration. This permits the exploitation of both directions of membrane travel, and hence, allows for a nearly continuous output flow.
- *Dual magnets:* Double chamber designs inherently favor symmetric components. A thin membrane with a single magnet on each side has been selected as a chamber divider and

actuation system. This not only provides a symmetric feature but also eases the assembly process by allowing the magnets to be attached to the membrane and held in place by their own magnetic attraction alone. Furthermore, affixing the magnets to the outside of the membrane permits changes to be made to the sizes or shapes of the membrane and magnets independently.

- *Separate reusable/disposable parts:* Figure 12 shows the two separate parts of the system. The reusable part contains the majority of components: the coils, sensor and electronics. The disposable part contains the fluid, valves, membrane and magnets; everything is sealed with the focus on cost reduction. There is no physical contact between the reusable section and the magnets (or the fluid).

Membrane

The use of two coils eliminates the need for a strong elastic force which is required in many micropump designs for returning to the rest position. As a result, an optimal membrane must have elastic properties which are negligible compared to the magnetic driving force yet strong enough to prevent deformation from fluid pressure.

Optimal materials which satisfy these requirements are soft elastomers like Latex or silicone based PDMS (*see Table 1*):

- For biological applications, Dow Corning Silastic PDMS membrane Q7-4750 has been selected due to both appropriate mechanical properties and bio-compatible FDA approval.
- For non-biological applications, classical latex membranes, as in latex gloves, can be used to further reduce cost.

Material	Thickness (mm)	Young's Modulus (MPa)	Elongation (%)
Latex	0.10	0.6	400
Q7-4750	0.15	2.1	930

Table 1 - Material properties of selected membranes.

Note: A detailed study regarding the performance and characterization of various membranes is presented later in this chapter.

Magnets

To obtain the optimum actuation properties, the selected magnets need to possess the greatest possible magnetization. The mass of the magnets is of little importance since the magnetic force dominates the inertial effects. In the case of typical rare earth magnets with a remanent flux density $\mathbf{B}_{\text{rem}} > 1.2T$ and a mass density $\rho \approx 7500 \text{ kg} \cdot \text{m}^{-3}$, one obtains a magnetic force density of $F_m = (\mathbf{M} \cdot \mathbf{B}_{\text{coils}}) > 800,000 \text{ N} \cdot \text{m}^{-3}$ with a magnetic field gradient $(B_z) = 0.8T \cdot \text{m}^{-1}$ emanating from the coils; the maximum possible gravitational force (orientation dependent) is $F_g = g \cdot \rho \approx 75,000 \text{ N} \cdot \text{m}^{-3}$. This results in an acceleration of several G's; as a consequence, the velocity of the magnets (in a fluid) will reach steady-state conditions in just a few tens of microseconds, confirming that the inertia of the magnet may be neglected. Therefore, the optimal choice is the magnet which provides the greatest magnetization possible but at a reasonable price (for disposable use). In our design, we have selected rare earth magnets of composition Neodymium-Iron-Boron (NdFeB), grade N52, with a remanent flux density of $1.5T$ and a cost of just a few cents to a dollar each depending on size. The NdFeB magnets used in all trials have been electroplated with only a thin nickel coating to resist corrosion. Therefore, for use in biological applications and to be FDA compatible for use with the Silastic membranes, the magnets will need to be coated with a thin layer of PDMS or similar biocompatible material.

Electromagnetic Coils

The magnetic force created by each coil depends only on its size and current density \mathbf{J} , not on the number of turns or the diameter of the wire used in the coil. However, for a given \mathbf{J} , the associated electric properties will be affected by the gauge of the wire. Each coil will have the following voltage U , current I and power P :

$$U = \langle J \rangle \rho 2\pi \langle r \rangle \frac{S_{coil}}{S_{spire}}$$

$$I = \frac{\langle J \rangle S_{spire}}{\alpha}$$

$$P = \frac{\langle J^2 \rangle \rho 2\pi \langle r \rangle S_{coil}}{\alpha}$$

where $\langle J \rangle$ is the average current density inside the coil (taking into account the air and insulative components); ρ is the resistivity of copper; $\langle r \rangle$ is the average radius of the spires of the coil; S_{coil} is the total cross-sectional area of the coil and S_{spire} is the copper surface of each spire. α is the proportion of the coil cross section occupied by the copper: for a coil in the most compact arrangement, the wires occupy $\frac{\pi}{2\sqrt{3}}$ of the cross-section; taking into account the insulative layer thickness yields $\alpha = \frac{0.9\pi}{2\sqrt{3}}$.

P does not depend on S_{spire} , which means that the energetic efficiency of the actuator does not depend on the wire thickness; its only effect is on U and I levels. Since we desire a maximum U of 9V for battery powered operation and a maximum I of 200mA for efficiency reasons related to battery internal resistance, the dimensions of the coil become: inner radius: 2mm; external radius: 9.5mm; thickness: 2mm, which yields: $\langle J_{max} \rangle = 1.25 \times 10^7 A \cdot m^{-2}$;

$S_{spire} = 1.3 \times 10^8 m^2$; and wire diameter $t = 0.135mm$ (which corresponds to a 36-37AWG wire).

Valves

In the context of the selected pump type and actuation scheme, three types of valves are possible: active valves, nozzle/diffuser valves, and check valves. For low-cost and low-energy consumption systems, check valves are the most attractive solution. However, at the time of prototype production, there were no existing check valves which were satisfactory for this specialized application:

- Commercial check valves such as vacuum valves used in the automotive industry are bulky and cost several dollars. As a result, they cannot be used in the context of ultra-low-cost micropumps.
- Most of the custom check valves which have been fabricated for micropumps as in [55] [56] [57] are used with piezoelectric actuators. Unfortunately, the opening pressure is too high to be compatible with reduced force actuation systems like electromagnetic actuators.

As a result, we designed our own custom check valves to provide the following features: ultra-low-cost, reduced dimensions allowing direct integration within the pump body, and a very small opening pressure to ensure compatibility with reduced force actuators (*see next section*).

Free-Floating Membrane Valve Design

As pump dimensions are reduced, the forward pressure drop associated with passive valves becomes more significant. In many cases this pressure drop may be the dominant factor in determining pump efficiency. Many designs which work well at the macroscopic level, fail as the

scale is reduced. At these reduced scales common check valves designs, i.e. those incorporating a spring, can virtually eliminate all forward flow. As a result, valves based on free floating actuators (ball/slide/membrane) must be utilized.



Figure 13 - Fabricated and tested ball and slider style valves.

Of the three actuator styles, the best design was based on a free floating membrane which provided better performances than commercial vacuum valves for smaller overall dimensions. The device consists of three components assembled and bonded into a single unit: an inlet port with an inner flat surface, an outlet port with a flat, recessed surface in which a rosette pattern has been machined, and an elastomer membrane sandwiched in between, but free to float (see Figure 14). The design has been optimized to provide a fast response time while maintaining a minimal forward pressure drop. These characteristics were selected for optimization because minimizing the forward pressure drop is crucial for obtaining reasonable pump efficiencies, while fast response time is essential for dispensing minute amounts of fluid.

Device Operation

Reverse flow – At any point when there exists a fluid pressure at the outlet of the valve which exceeds the pressure at the inlet of the valve, reverse fluid flow conditions will develop. This reverse flow exists for only a very brief time during which it acts to sweep the membrane towards the flat surface of the inlet port. Once the membrane is in contact with this surface, the membrane acts to cover the hole formed by the inlet port preventing any further reverse flow (See bottom right of Figure 14).

Forward flow – At any point when there exists a fluid pressure at the inlet of the valve which exceeds the pressure at the outlet of the valve, forward fluid flow conditions will develop. This forward flow acts to sweep the membrane towards the flat rosette carved surface of the outlet port, similar to the situation described for reverse flow. Unlike the case of reverse flow however, the outlet port has a rosette pattern machined into it allowing the fluid to flow around the membrane by passing through these rosette channels. The width and depth of these channels, the degree of membrane diameter reduction (with reference to the recessed inlet port diameter), as well as the magnitude of the gap in which the membrane moves back and forth, determine the forward pressure drop of the valve. Unfortunately, the width of the gap also effects the response time of the valve with an inverse relationship to the forward pressure drop. A careful compromise is therefore necessary in order to provide a fast response time while maintaining a minimal forward pressure drop (See bottom left of Figure 14).

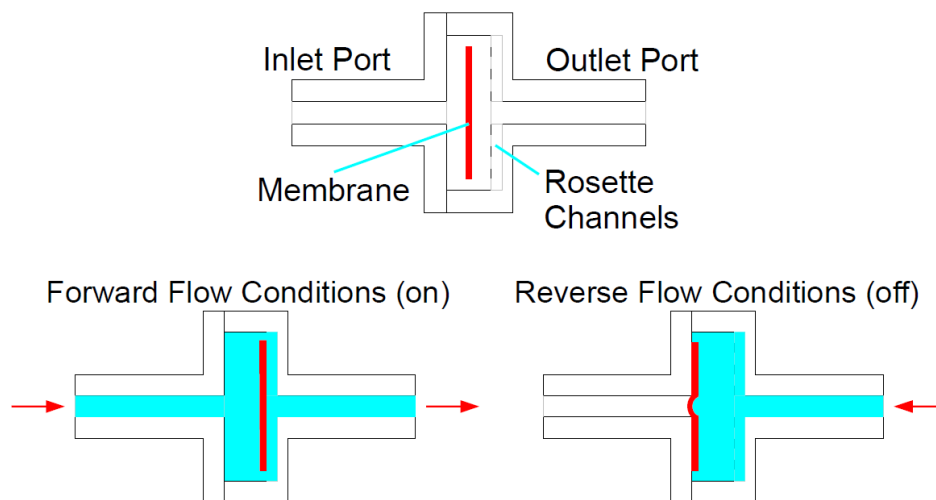


Figure 14 - Diagram and operating principle of a membrane based check valve.

Physical Description

In its discrete form, the device consists of three parts assembled and bonded into a single unit. The parts consist of an elastomer membrane, an inlet port with a flat surface which contacts the membrane, and an outlet port with a flat, recessed surface in which a rosette pattern has been machined. The membrane is designed to have a diameter about 20% less than the diameter of the recessed inlet port surface. The inlet and outlet ports are arranged so that their flat surfaces face each other (ports facing outward) with the membrane sandwiched in between, but free to float. Finally, the two halves are permanently bonded together and the valve is functionally complete. See Figure 1.1.

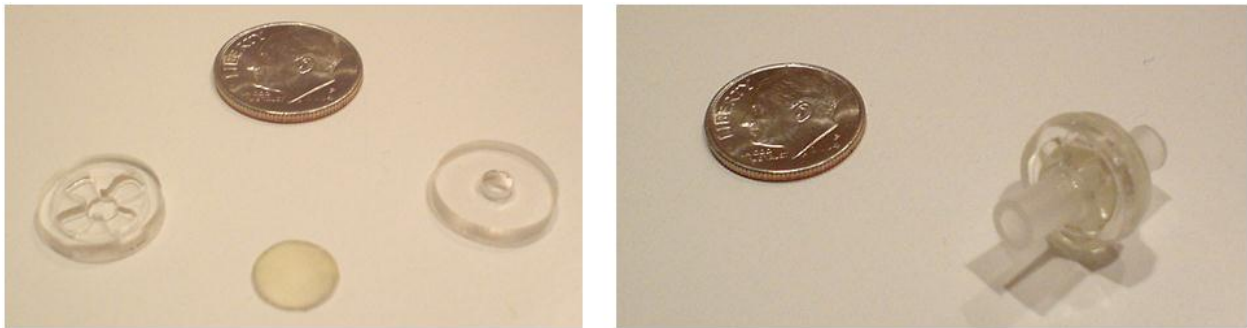


Figure 15 - Discrete check valve components and assembly.

It is important to recognize that although these valves can be produced in a functional and compact discrete form, further device size reduction can be obtained by integrating the simplistic form of these valve bodies directly into the pump. This is exactly which is meant by “integrated check valves” in the context of this pump design. A computer model of this integrated design was presented earlier in Figure 10.

Membrane selection and analysis

In any membrane based device, the performance of the membrane itself is often of principle concern. The material properties of the membrane including, its elasticity, rigidity, thickness, and lifespan frequently define the limiting factors of device performance. While each of these characteristics may be scientifically determined and quantified independently, the most accurate way of defining performance is to physically construct a prototype and test each membrane under "real world" conditions. In this study, we focus on the testing protocol and results of various membranes as evaluated in an embedded low-cost micropump ("Micropump v2.0") suitable for disposable use.

Objectives

The objective is to determine the influence of the membrane on the performance of the micropump. Specifically, we wish to determine the characteristics of the membrane with regards to its:

- Influence on frequency of mechanical resonance
- Influence on the volumetric flow rate
- Hysteresis and elasticity
- Mechanical resistance
- Influence on the power consumption
- Effects on fluid pressure

Accurate, quantifiable, and reproducible tests must be carried out to satisfactorily characterize membrane behavior for each of the above objectives.

Materials

The membrane materials selected for testing include a traditional membrane elastomer latex as well as an FDA approved bio-compatible silicone based Q7-4750 membrane (tested for three different thicknesses). The following table (REF) lists the membranes tested along with their selected material properties.

Material	Thickness (mm)	Young's Modulus (MPa)	Elongation (%)
Latex	0.10	0.6	400
Q7-4750	0.15	2.1	930
Q7-4750	0.25	2.1	930
Q7-4750	0.38	2.1	930

Table 2 - Material properties of selected membranes.

Device

In order to best exploit the results of the experimental testing, care was maintained to provide real operating conditions similar to what will be experienced in the final application. As a result, the pump selected for membrane evaluation is the same pump described in this section “Micropump v2.0”. This pump, which was designed and fabricated in our lab, allows for rapid interchanging of actuator membranes. The basic parts and physical structure of this pump are depicted in Figure 12 and Figure 23.

Protocol

Measurement protocols for each type of test as well as associated procedures are summarized in the subsections which follow:

Flow measurement

The general principle employed in determining volumetric flow rate involves the pumping of a fluid (of known density) from a large reservoir to a small sampling beaker. The collected fluid is then weighed on a precise digital scale and the volumetric flow rate is determined from the mass, density, and elapsed time.

In order to minimize the effects of changing fluid levels on pumping performance, a very large reservoir was used such that the changes in fluid height throughout the tests were negligible. The fluid collection container was much smaller facilitating the use of a precision digital scale without invoking overload conditions. After the fluid collection and weighing of each sample, the sampling container was carefully cleaned and dried and then returned for the next collection.

Hysteresis measurement

To obtain the hysteresis measurement of each membrane, the pump electronics were commanded to slowly sweep the driving voltage over the entire operating range. The actual motion of the magnets was monitored in real-time by the embedded Hall effect sensor. The results of these measurements were then sent to a desktop computer and plotted.

Pressure measurement

The maximum pressure deliverable by the pump was determined through hydrostatic testing. Elevating the output tube just until the point at which the flow ceases reveals the point of static equilibrium between the pumps actuator and the weight of the column of water in the tube. The pressure at the base of the tube is therefore equal to the maximum pressure that the pump can deliver. This pressure is then calculated using the properties of the fluid and the known

gravitational field acting on it, and thus, the maximum pressure deliverable by the pump is revealed.

Power consumption measurement

Since the open-loop drive current is always known, power consumption of the micropump may be determined by applying the familiar electrical power dissipation equation $I^2 \times R$. By varying the drive current, a multitude of datum points were obtained and analyzed to yield the flow rate vs. power consumption for each membrane.

Results

After collecting the data as outlined in the previous sections, the results were tabulated, plotted, and analyzed in an effort to meet the objectives as stated at the beginning of this section. The sections which follow summarize the results of these findings.

Reproducibility

To determine the reproducibility of the flow rate measurements as described in the *Protocol* section, the following measurements were conducted repeatedly:

- Constant current for the following frequencies: 1Hz, 2Hz, and 5Hz. (see Table 3) *Note: the specified drive currents are per coil; each measurement was performed 10 times.*

Trial	Minimum (mL/min)	Average (mL/min)	Maximum (mL/min)	Std. Dev. (δ)
200mA, 0.5Hz	60.8	62.25	60.54	0.17
200mA, 1.0Hz	118.17	118.61	119.07	0.32
200mA, 2.0Hz	163.82	164.20	164.64	0.31

Table 3 - Reproducibility data for a fixed drive current.

- Constant frequency for the following drive currents: 50mA, 100mA, and 200mA per coil.
(see Table 4) *Note: each measurement was performed 10 times.*

Trial	Minimum (mL/min)	Average (mL/min)	Maximum (mL/min)	Std. Dev. (δ)
1Hz, 200mA	118.17	118.61	119.07	0.32
1Hz, 100mA	98.67	99.11	99.36	0.27
1Hz, 50mA	51.17	51.35	51.59	0.18

Table 4 - Reproducibility data for a fixed drive frequency.

It is also of interest to determine the reproducibility of the hysteresis measurement described in the *Protocol* section. To this end, the hysteresis measurement was carried out five times on the same membrane which resulted in the following set of hysteresis curves (Figure 16):

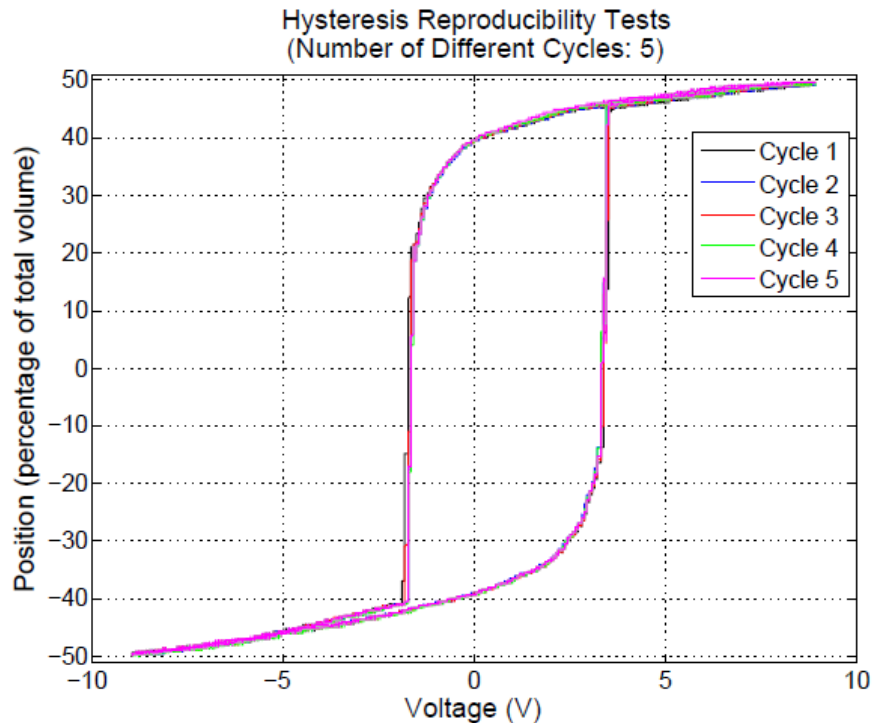


Figure 16 - The experimental results of five consecutive hysteresis measurements performed on the same membrane.

Resonant frequency

The pump can be driven over a large range of frequencies; however, there is one particular frequency for which the pump operates best, its resonance frequency. This frequency can be easily identified by driving the pump (open-loop) over its entire range of operating frequencies and observing which frequency provides the greatest flow rate. Figure 17 depicts the results of this procedure for each of the four membranes tested.

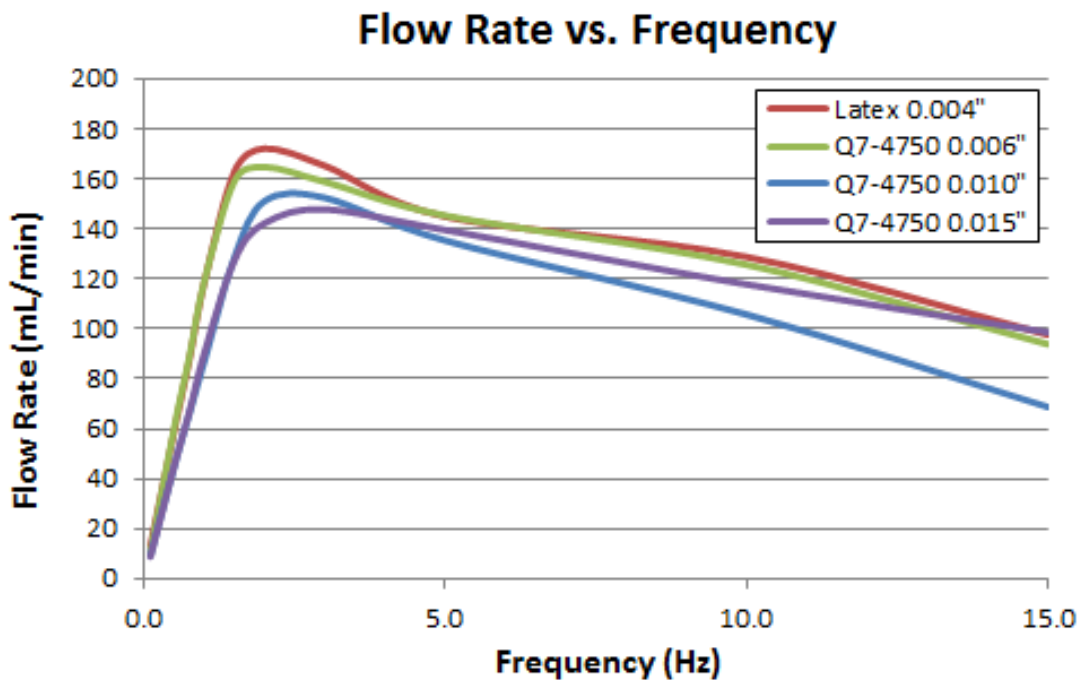


Figure 17 - The experimental results of Flow rate vs. Frequency trials for each of the four membranes tested (200mA per coil).

Flow rate

While it appears in the previous section that all of the membranes tested produce similar flow rates, it is important to note that there is in fact an increased consumption of energy in moving the thicker membranes. To further explore this concept, the volumetric flow rate as a function of drive current was tested (see *Protocol* section for an outline of the testing procedure). The

experimentally collected data for the maximum flow rate as a function of current is depicted in Figure 18.

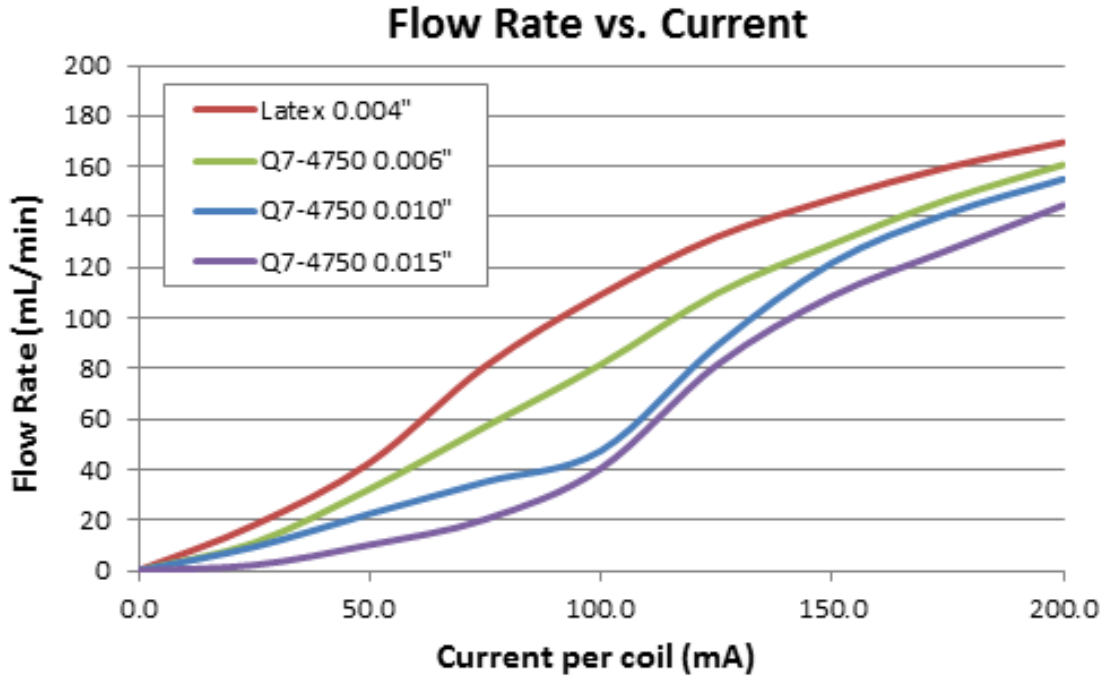


Figure 18 - The experimentally determined volumetric flow rate vs. drive current.

For each case, the coils were excited at the resonant frequency previously determined in *Section Resonant frequency*. Note: the specified drive currents are per coil; each measurement was performed 5 times.

Hysteresis

Any system which exhibits hysteresis exhibits path-dependence. In the case of membrane pumps, path-dependence means that the position depends not only on the driving voltage, but also on the direction of travel. Figure 19 depicts the experimentally determined hysteresis of each membrane utilizing the methods outlined in the *Protocol* section.

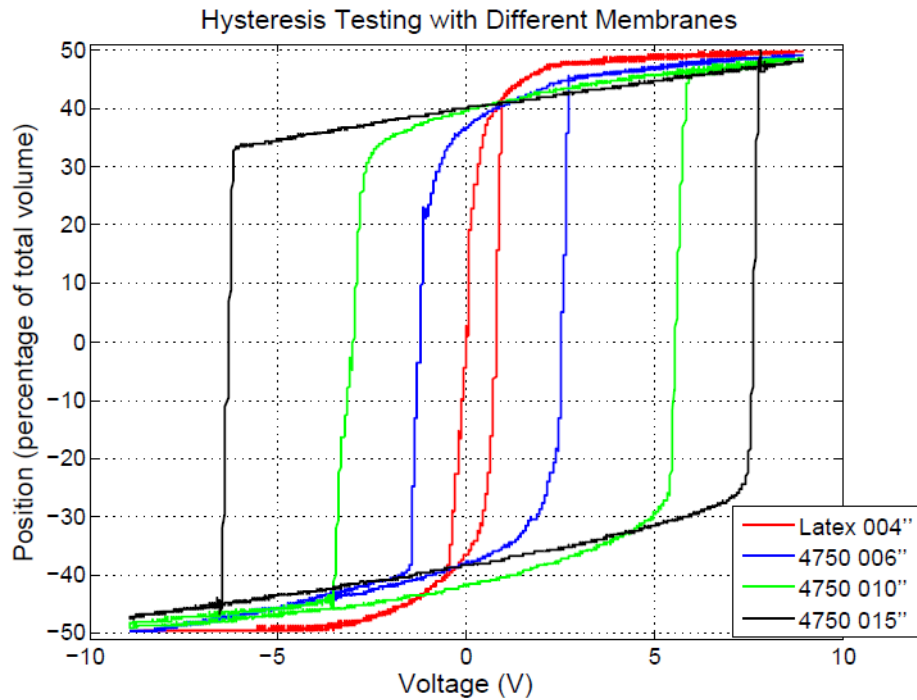


Figure 19 - The experimentally determined hysteresis curves for each of the membranes tested.

Power consumption

The volumetric flow rate as a function of power consumption was obtained using the methods outlined in the *Protocol* section. The results of which are plotted in Figure 20. *Note: the specified power consumptions are per coil.*

Fluid pressure

The maximum fluid pressure attainable for each membrane was determined using the methods described in the *Protocol* section. The results of these trials are contained in Table 5. *Note: the specified drive currents are per coil.*

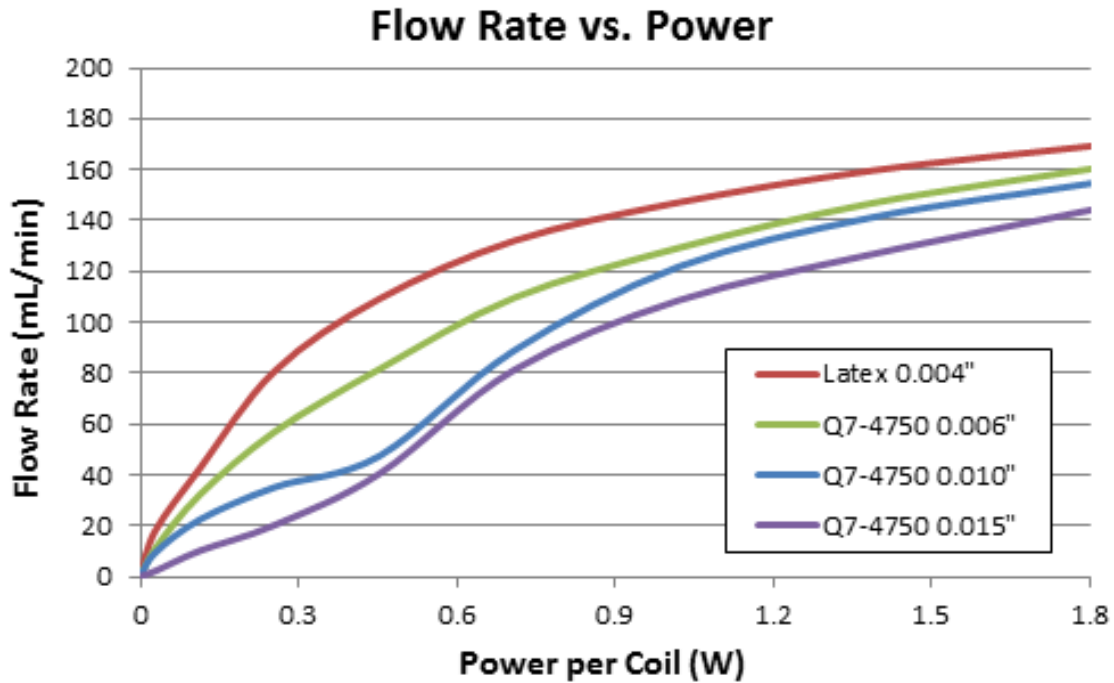


Figure 20 - The experimentally determined volumetric flow rate vs. power consumption.

Membrane	I = 200 mA	I = 100 mA	I = 50 mA
	Max. Pressure (Pa)	Max. Pressure (Pa)	Max. Pressure (Pa)
Latex 0.004"	2550	1545	834
Q7-4750 0.006"	2501	1471	686
Q7-4750 0.010"	2452	1422	466
Q7-4750 0.015"	2010	1079	343

Table 5 - Fluid pressure as a function of drive current.

Resilience

During actuation, the membrane is deformed. The resilience of the membrane to tear failure will depend on the maximum strain reached with respect to the maximum (breaking) elongation.

Figure 21 depicts the distribution of strain inside the membrane while held at the maximum

possible deformation (deformed until reaching a wall). We can see that the strain experienced by each of the different membranes tested have a very low value compared to the elastomers maximum deformations (around 10% - 20% depending on the membrane); except on the boundaries membrane/magnet and membrane/wall. Table 6 contains the values of the maximum strain on the boundaries for each of the membranes tested.

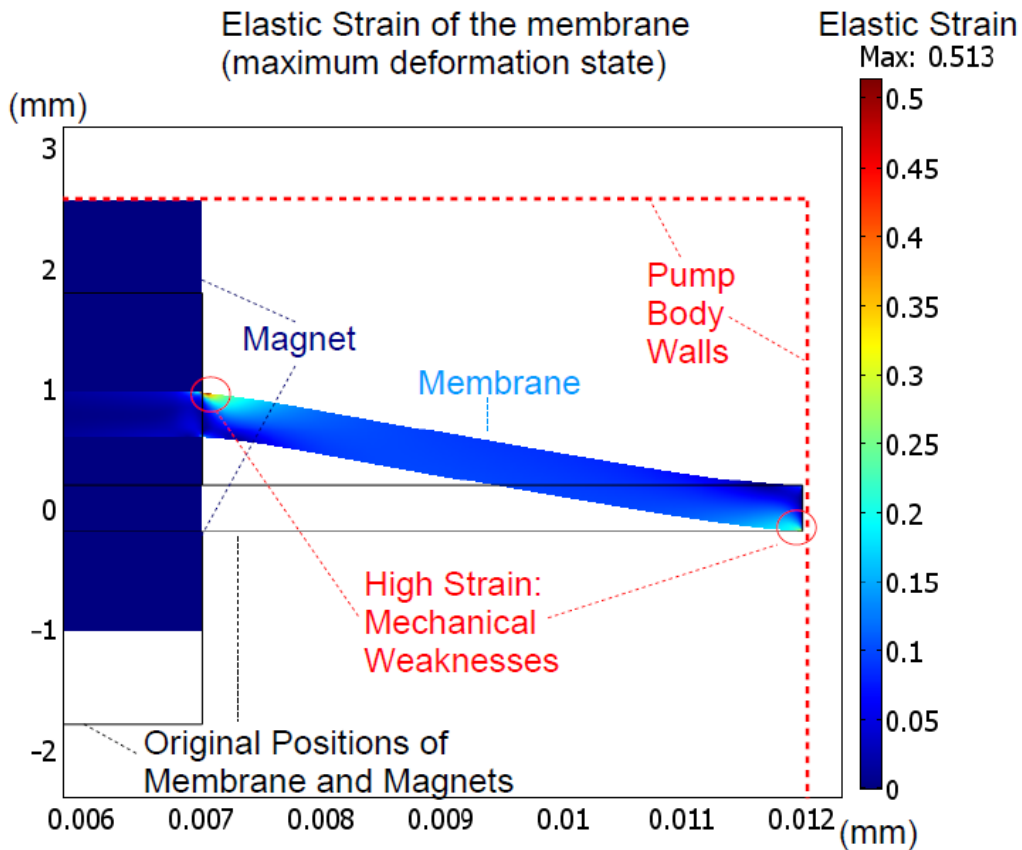


Figure 21 - Strain distribution inside the membrane at maximum deformation.

We can see from Table 6 that even at the weakest points, the strain experienced by the membrane is much lower than the break strain (over the entire range of deformations possible within the pump). Thus, the mechanical resilience does not play a role in the choice of membrane.

Membrane	Thickness (mm)	Maximum Strain	Failure (%)
		Attained (%)	
Latex 0.004"	0.10	30	400
Q7-4750 0.006"	0.15	32	930
Q7-4750 0.010"	0.25	40	930
Q7-4750 0.015"	0.38	51	930

Table 6 - Maximum strain attained during the deformation of the selected membranes.

Summary

The following table (Table 7) compares some key parameters for each of the membranes tested:

Membrane	Max. Flow Rate (mL/min)	Max. Pressure (Pa)	Max. Strain (%)	Hysteresis Area (V·mm)
Latex 0.004"	172.14	2550	30	2.46
Q7-4750 0.006"	164.73	2501	32	12.02
Q7-4750 0.010"	152.45	2452	40	29.33
Q7-4750 0.015"	147.80	2010	51	45.24

Table 7 - Comparison of selected parameters for each membrane tested.

It is obvious from the table (Table 7) that the latex membrane provided the best performances overall. That is, the latex membrane produced the greatest possible flow rate, the maximum output fluid pressure, experienced the least amount of strain, and exhibited the best hysteresis of the membranes tested. In terms of bio-compatible membranes only, the Q7-4750 0.006" membrane performed the best.

The following table (Table 8) compares the electric current and power consumption of each membrane for two fixed flow rates; namely, 70 mL/min and 140 mL/min.

Membrane	Current Consumption (mA)		Power Consumption (W)	
	Flow Rate	Flow Rate	Flow Rate	Flow Rate
	70 mL/min	140 mL/min	70 mL/min	140 mL/min
Latex 0.004"	67.89	138.22	0.215	0.874
Q7-4750 0.006"	88.25	165.24	0.361	1.246
Q7-4750 0.010"	113.62	173.33	0.593	1.366
Q7-4750 0.015"	118.10	193.47	0.639	1.705

Table 8 - The current and power consumption of each membrane for selected flow rates.

It is obvious from Table 8 that the latex membrane provided the best current and power consumption for a given flow rate. Once again however, in terms of bio-compatible membranes only, the Q7-4750 0.006" membrane performed the best.

Membrane Selection

Based on the results of this study, we have found that latex provided a superior performance with respect to the three other membranes tested. The differences are significant enough to necessitate selection of a material with similar mechanical properties and thickness. However, since latex is not a bio-compatible material, for biological applications we recommend selecting a PDMS based membrane from the Silastic Q7-47xx family, similar to the membranes tested but perhaps even thinner and softer (ie. a membrane from the Q7-4720 family).

Fabrication

All of the micropump components were fabricated using standard machining techniques and equipment. This allowed for reduced development costs and ultimately ultra-low mass production costs. This is especially true for the disposable portion of the pump which was

intentionally produced with simple, inexpensive, and rapid fabrication techniques that do not require expensive materials or equipment.

Pump Body and Clamshell

The pump body and clamshell are of a unique design and therefore must be custom fabricated. Fortunately they are made from acrylic plastic which increases the flexibility of production. In industry, there are two standard methods which can be used for their fabrication:

- Employing the use of traditional machine fabrication tools, such as a Computer Numerical Controlled (CNC) mill.
- Plastic injection molding.

We chose to produce our pumps with a CNC mill since we only required a limited number of prototypes and desired the flexibility of making changes to the dimensions throughout the manufacturing run. In the case of mass production however, plastic injection molding is the cheapest and fastest way to produce these parts.

Check Valves

Since the check valves are integrated within the pump body itself, they were fabricated by simply machining the appropriate recessed membrane housings and rosette channel patterns into the side of the pump body. Similar patterns were then machined into the plastic valve cover. The membranes were then inserted and the plastic valve cover was permanently bonded to the pump body.

Electromagnetic Coils

The electromagnetic coils were fabricated by winding 37 gauge magnet wire around a brass bobbin; during winding, a binder was continually added to the wire feeding the spool. This

resulted in electromagnetic coils with a resistance of about 42 Ohms and an inductance of about 3.8mH (see green coil in Figure 23).

Electronic Driver Circuit

Surface-mount printed circuit boards were fabricated using direct resist transfer and hot gas convection reflow of a 63Sn/37Pb SMD solder paste. The resulting printed circuit board is depicted in Figure 22.

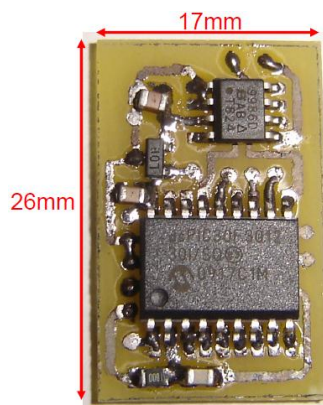


Figure 22 - Electronic driver printed circuit board.

Assembly

In accordance with the desired broader impacts of this research work, it is desirable for the resulting pump designs to be manufacturable using low cost fabrication techniques. Care was therefore taken to ensure that the assembly process remained quick and simple. The actual assembly process is outlined below:

- The magnets are centered on the membrane and held in place by their own magnetic attraction.
- The membrane is cut directly from either a latex sheet or a Dow Corning Q7-4750 sheet and placed between the upper and lower portions of the pump body. The two sections of

the pump body are then fastened together. This can be accomplished using screws, or an adhesive binder.

- The check valve membranes are inserted into their integrated housings and the plastic check-valve covers are permanently bonded to the pump body.
- The coils are glued into the clamshell and the coil supply leads are routed through the body and soldered to the PCB board.
- Finally, the sensor is glued into its dedicated position within the clamshell and connected to the PCB board.

The complete pump is pictured in Figure 23.

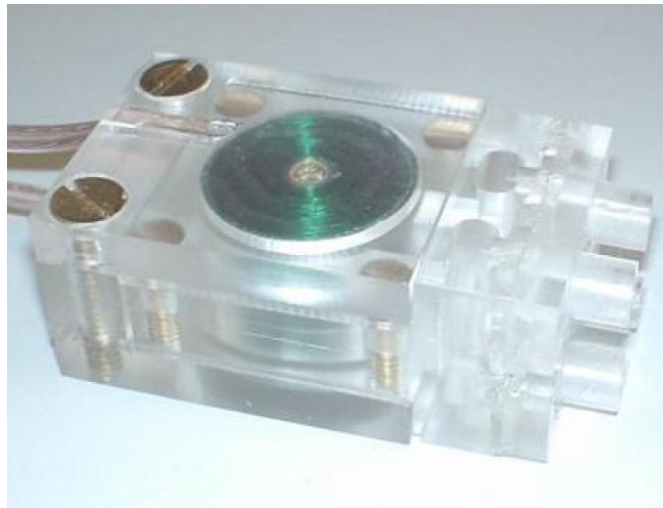


Figure 23 - Complete micropump and clamshell with all parts assembled.

Results and characterization

Performance of the micropump has been characterized for both envisaged membranes (Latex and bio-compatible PDMS) in open-loop (for a better measurement of the intrinsic properties of the pump), for a variety of conditions, namely:

- *Flow rate vs Frequency*: The flow rate as a function of the excitation frequency has been measured (Figure 24). The driving signal is a square wave of amplitude $I = 200\text{mA}$ sent to each coil. The presented results are the average value of 10 measurements.
- *Flow rate vs Current*: The flow rate as a function of the electric current has been measured (Figure 25). The signal is a square wave of frequency $\nu = 2\text{Hz}$ (the previously determined optimum frequency for square waves). The presented results are the average value of 10 measurements.
- *Hysteresis*: The hysteresis cycles have been measured by utilizing the sensing techniques described in Chapter 6 (see Figure 26). Each cycle has a duration of 10 minutes. The presented results are the average value of 10 cycles.
- *Fluid backpressure*: The fluid pressure has been measured as a function of the current (Table 9). The experimental method consists of pumping water into the base of a graduated cylinder, and measuring the maximum height obtained (where 1cm of water = 100Pa).

The general principle employed in determining volumetric flow rate involves the pumping of a fluid (of known density) from a large reservoir to a small sampling beaker. The collected fluid is then weighed on a precise digital scale and the volumetric flow rate is determined from the mass, density, and elapsed time. In order to minimize the effects of changing fluid levels on pumping performance, a very large reservoir was used such that the changes in fluid height throughout the tests were negligible. The fluid collection container was much smaller facilitating the use of a precision digital scale without invoking overload conditions. After the fluid collection and weighing of each sample, the sampling container was carefully cleaned and dried and then returned for the next collection. The results are summarized in Table 10.

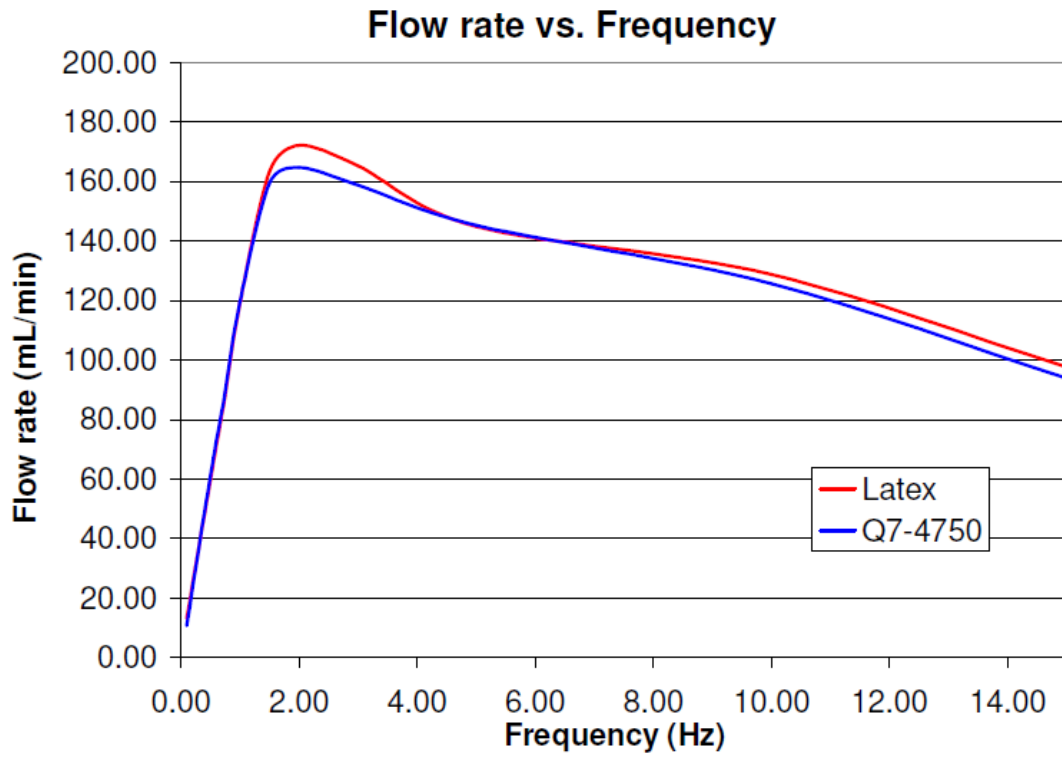


Figure 24 - The experimental results of flow rate vs. frequency trials for each of the membranes tested (200mA per coil).

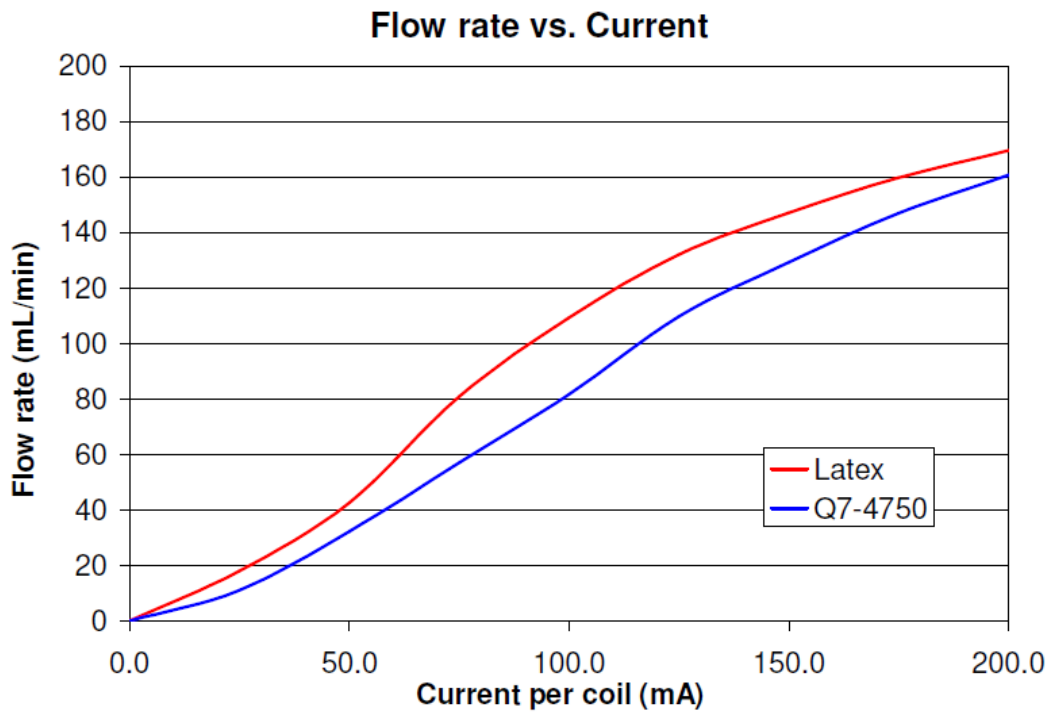


Figure 25 - The experimentally determined volumetric flow rate vs. drive current.

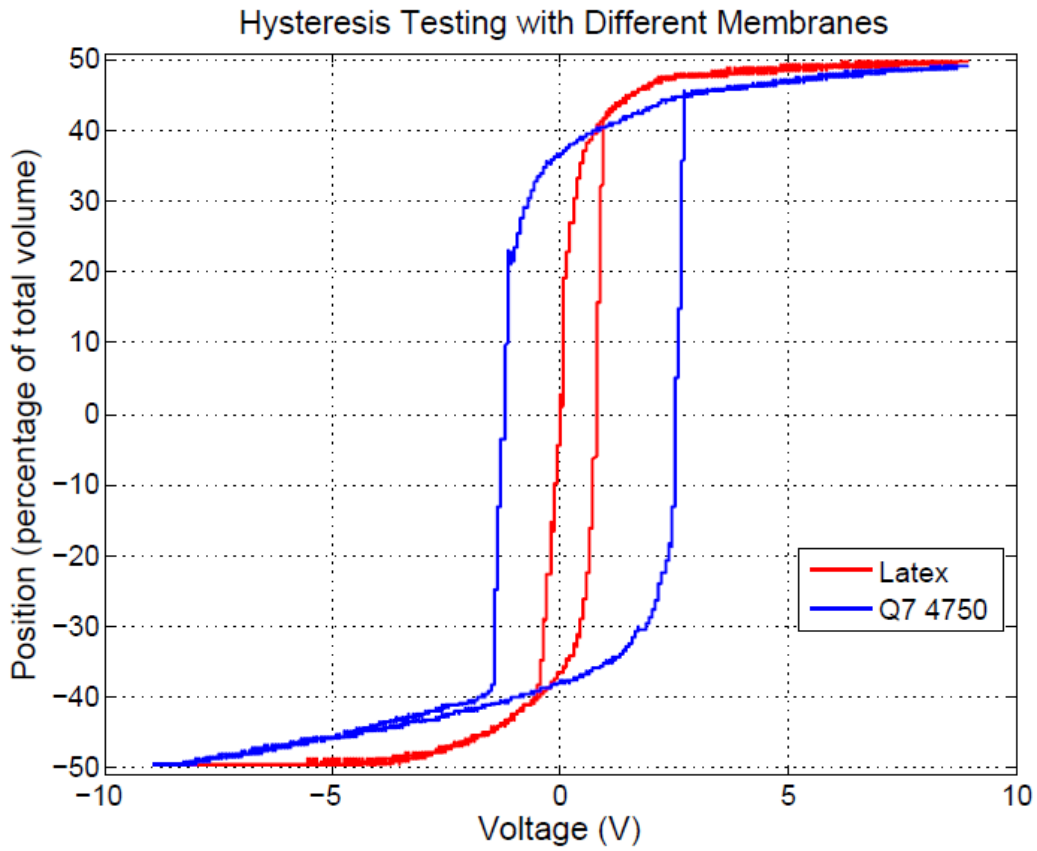


Figure 26 - The experimentally determined hysteresis curves for each of the top performing membranes tested.

Membrane	I = 200mA	I = 100 mA	I = 50 mA
	Max. Pressure (Pa)	Max. Pressure (Pa)	Max. Pressure (Pa)
Latex 0.004"	2550	1545	834
Q7-4750 0.006"	2501	1471	686

Table 9- Fluid pressure as a function of drive current.

Membrane	Max. Flow Rate (mL/min)	Max. Pressure (Pa)	Hysteresis Area (V·mm)	Pump Dimensions (mm)
Latex 0.004”	172.14	2550	2.46	35×25×18
Q7-4750 0.006”	164.73	2501	12.02	

Table 10 - Summary: performances of Micropump v2.0.

The micropump we have developed produces flow rates up to 170mL/min, fluid pressures of 2.5kPa, and dimensions (including the electronic driver) of 35mm×25mm×18mm. These results are competitive with other micropumps of similar dimensions, e.g [58] (flow rate 1.8mL/min, dimensions 44mm×17mm×8mm - not including electronics), [59] (flow rate 0.25mL/min, dimensions 20mm×16mm×16mm - not including electronics), [17] (flow rate 2.1mL/min, dimensions 10mm×10mm×8mm - not including electronics), or [60] (flow rate 6mL/min, dimensions 36mm×25mm×14.5mm - not including electronics). The laboratory test setup created for Micropump v2.0 is pictured in Figure 27.

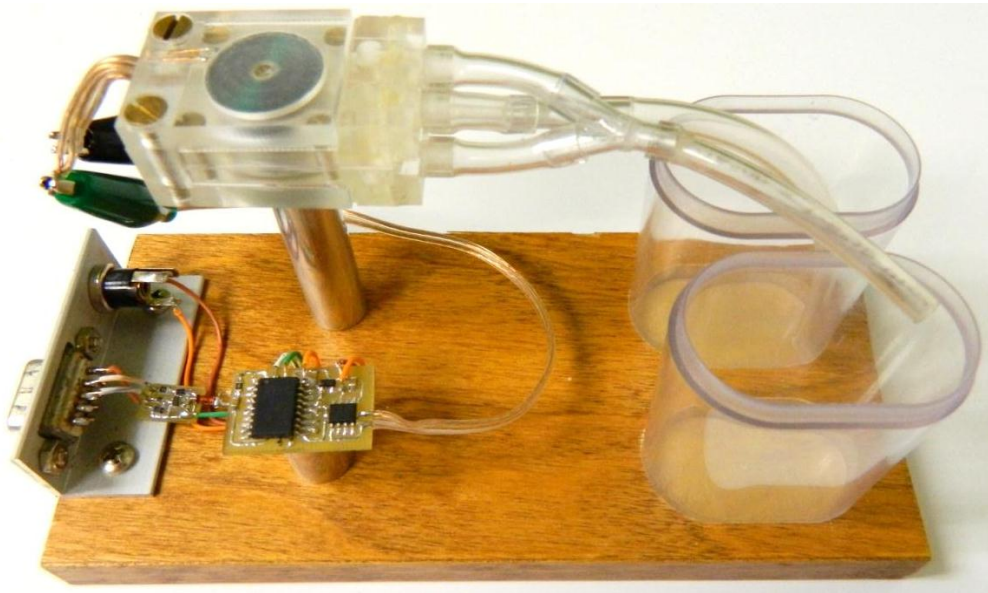


Figure 27 - Laboratory test setup.

CHAPTER 6 – Closed-Loop Sensing and Control

The implementation of closed-loop control is often only adapted to sophisticated and expensive systems, mainly because of the traditionally high cost of sensors and associated electronic systems. In this case, the ability to measure and control the real-time position of the armature magnets is essential. Fortunately, modern advances in electronic manufacturing techniques have yielded the production of economical sensors and electronics which actually allow for a reduction in overall cost when compared to a comparably performing system driven in open-loop.

Methods and Design

For the main application of the pump and embedded drug delivery systems, precise fluidic dosing is required. This is possible in an open-loop configuration only if the system has highly reproducible characteristics during its use and throughout its lifetime. Systems of this nature are very costly to design and fabricate. The performance of these pumps depends on the tension and age of the membrane, the position of the armature magnets, changes in tubing dimensions, the state of the check valves, the temperature of the coils, the charge remaining in the battery, etc.

The use of closed-loop control eliminates the need to keep these parameters stable and greatly reduces the cost for the disposable portion of the pump. However, this is only true if the costly sensing and control components are located in the reusable portion of the pump. This condition necessitates the use of a contactless sensing system. The most interesting solution - simple, cheap, efficient - is to measure the magnetic field that emanates from the permanent magnets, the magnitude of which is dependent on their position. An additional benefit of closed-

loop control is that it prevents collisions between the magnets and chamber walls, which eliminates the possibility of damage and wear, and reduces noise.

Electronics

The main purpose of the pump electronics is to supply power, recondition the sensor signals, and control the pump at a compact and fully embeddable scale. The electronics are contained within the reusable portion of the pump. The electronic component requirements are as follows: (i) inexpensive, (ii) high current delivery capabilities (up to 400mA continuous), (iii) low energy consumption, (iv) small size (smaller than the pump body).

For this application, small-outline surface-mount components are the most appropriate technology available; in this case, the circuit can be limited to as few as three IC components: a voltage regulator, an H-bridge, and a microcontroller. The heart of the circuit is the dsPIC30F3012 microcontroller which essentially controls all operations and peripherals while simultaneously monitoring the information obtained by the feedback sensors. While the microcontroller is responsible for determining the timing and magnitude required to drive the pump coils, the actual power required by the pump exceeds the drive capabilities of the microcontroller itself. This issue is addressed by the addition of the Si9986 Buffered H-Bridge which is capable of handling much higher drive currents and voltages (up to 1 Amp and 13.2 Volts). The balance of the parts are used to regulate voltage levels, stabilize transients, and for signal conditioning.

The microcontroller is essentially a tiny computer for which we have designed, simulated, tested and ultimately programmed our custom operating system into its firmware. The system runs in an endless loop monitoring all system parameters and making real-time

adjustments to keep the system balanced around the desired control point. The control scheme implemented is that of a proportional-integral-differential (PID) controller. The position feedback data of the driver magnets is acquired using a linear hall-effect sensor oriented in an innovative fashion to eliminate signal noise. This resulted in very precise yet low cost and contactless (an important constraint for separating the disposable portion of the pump from the electronic control system) solution.

The system was designed to be battery powered and therefore careful attention was given to overall efficiency. To increase driver efficiency, the entire output driver is digital including the H-Bridge. The signal is pulse-width modulated (PWM) internally within the microcontroller and fed to the inputs of the bridge. The PWM chop frequency is 50 kHz, a frequency well above the range of human hearing (thus ensuring the coils will not produce any audible noise) yet low enough where the transistors are still within their efficient switching frequency range. Furthermore, the microcontroller is put to sleep (an ultra-low power state) whenever possible to eliminate unnecessary power consumption.

For external communication, a serial port interface was also incorporated within the design. This provided a versatile communication port which is compatible with a wide range of existing products and embeddable devices (such as wireless communication modules, PC data transfers and communication, additional sensors, etc.). By developing our own PC based graphical user interface we communicated with the electronic driver circuit, issuing commands and monitoring system performance. This allowed for enhanced testing, tuning, analysis, and demonstrations of pump performance. A schematic of the custom driver circuit complete with provisions for radiometric sensor input is depicted in Figure 28.

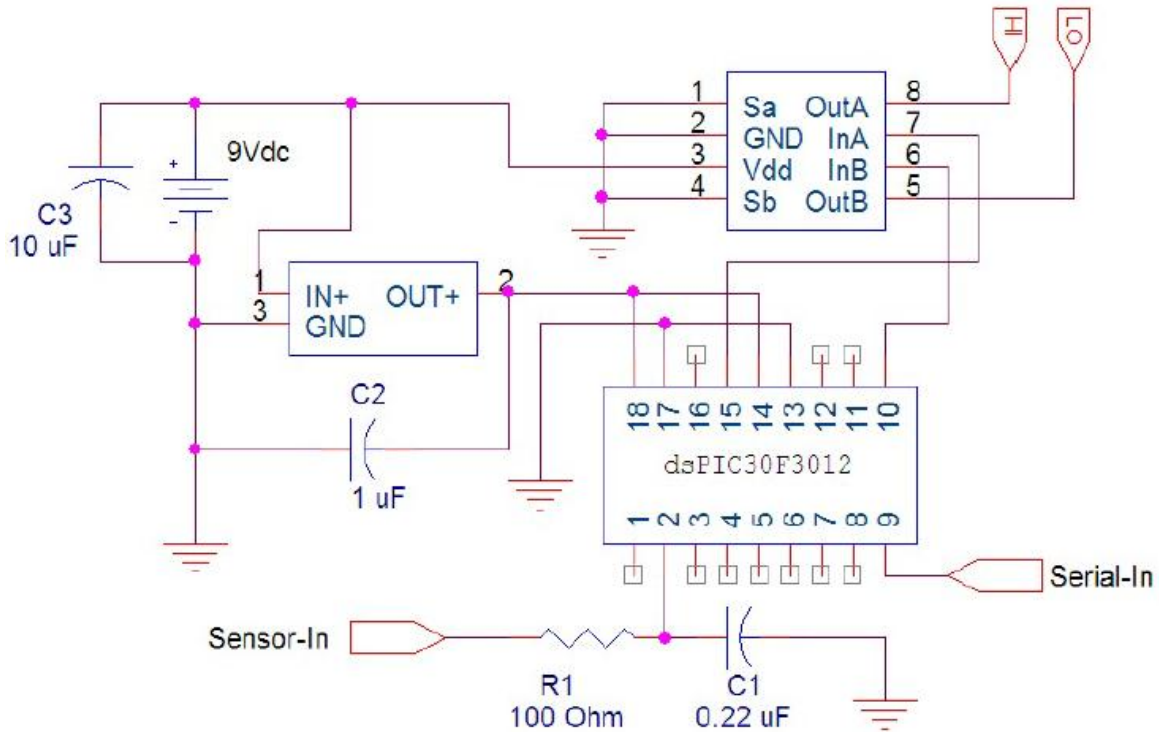


Figure 28 - Schematic of custom electronic driver circuit.

Hardware

The sensor selected is an A1301 linear Hall Effect sensor manufactured by Allegro Microsystems. The A1301 has a sensitivity of 2.5mV/Gauss. The control hardware is based on a dsPIC microcontroller.

Sensing Principle from Theoretical Study

The amplitude of the signal and of the magnetic perturbations is heavily dependent on the position and orientation of the sensor. The Hall Effect sensor is specifically oriented to only be sensitive to the radial component of the magnetic field B_r . To optimize the sensitivity of the system by minimizing the signal to noise ratio, the sensor is positioned in an area where only the permanent magnets create a non-negligible value of B_r (see Figure 29). In this particular sensor location, $B_r(\text{coil-lower})$ and $B_r(\text{coil-upper})$ are negligible while $B_r(\text{magnets})$ are maximized, as

compared to any other possible location outside the pump body (see Figure 30 and Figure 31). The magnetic field B_r created by the magnet is not linear as a function of its distance to the sensor. For this reason, the signal is compared to values in a lookup table to obtain the position. The values have been obtained thanks to a model corrected at the pump level during an auto-calibration step. The geometric orientation and details of the measurement principle are explained in the figure.

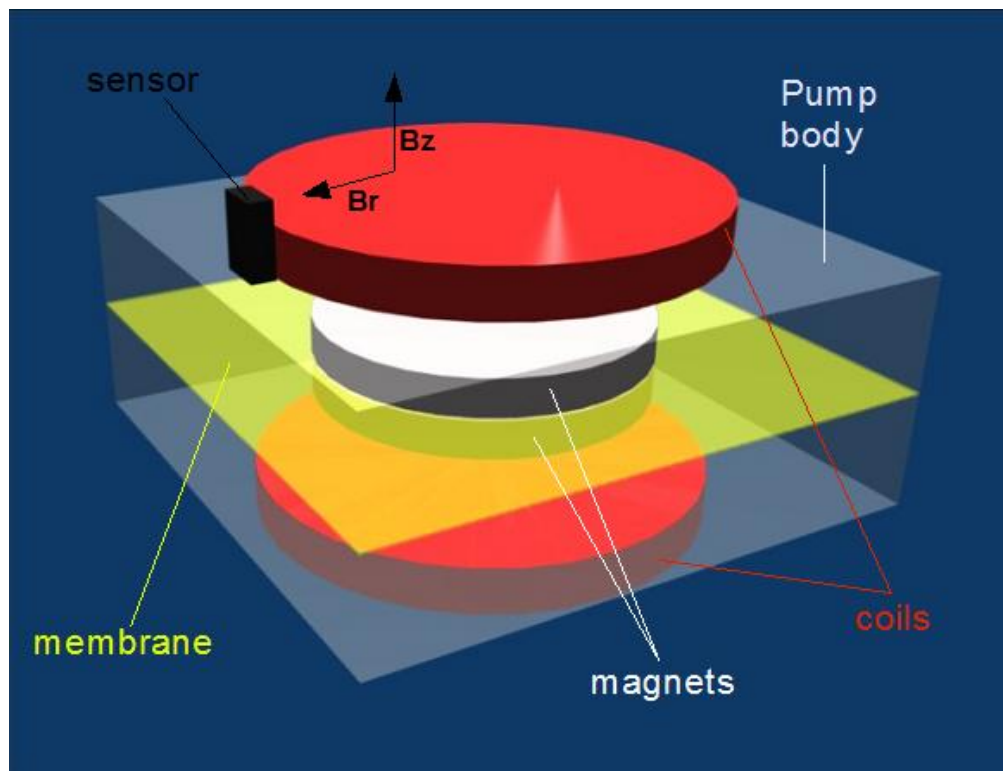


Figure 29 - The sensor location has been selected for an optimized signal to noise ratio. In this orientation, the sensor is only sensitive to the B_r component of the magnetic field.

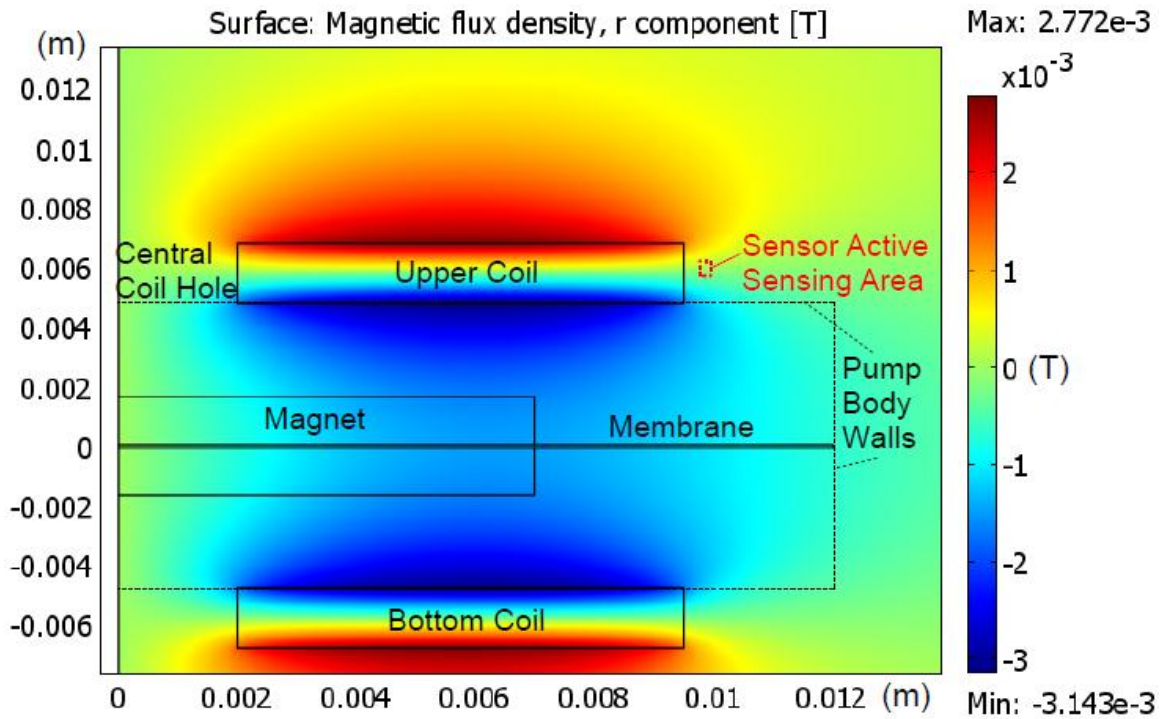


Figure 30 - Cartography around the pump depicting the magnitude of B_r created by the coils.

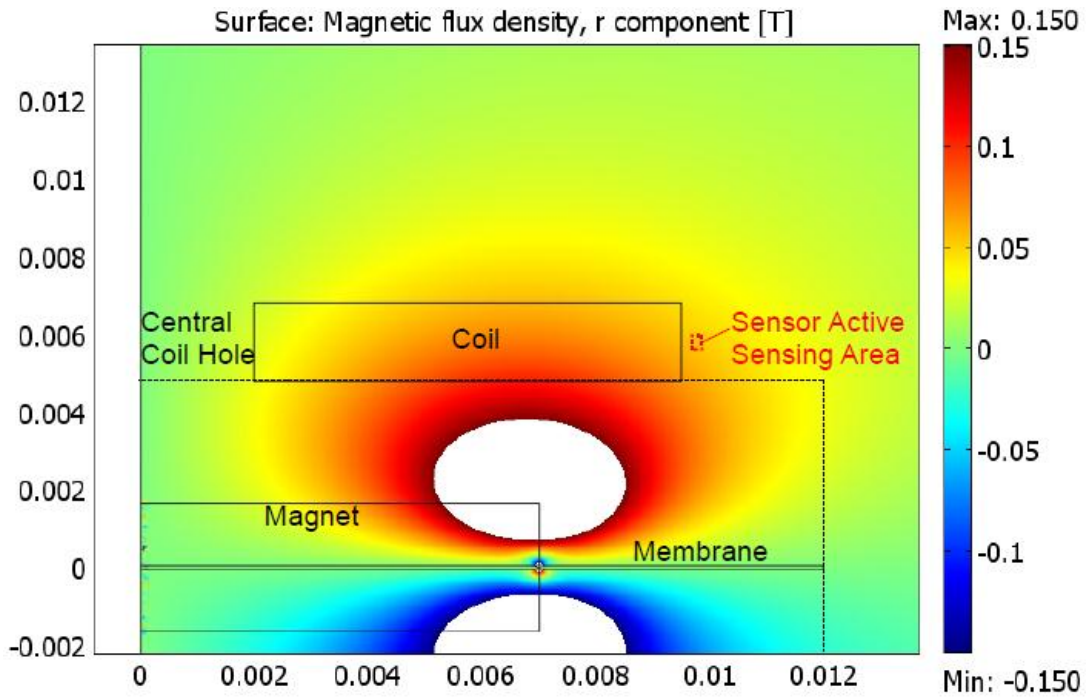


Figure 31 - Cartography around the pump depicting the magnitude of B_r created by the magnets. In this particular sensor location, $B_r(\text{coil})$ is negligible and $B_r(\text{magnet})$ is maximized.

A simplified and more intuitive explanation of the theoretical sensing principle is depicted in Figure 32. The top center of this figure illustrates the virtual absence of a radial magnetic field contribution from the upper coil as a result of the directionally selective fundamental operation of the Hall Effect sensor in the selected orientation. The contribution of the bottom electromagnet is partially shielded by the permanent magnets. Furthermore, the flux density of the bottom electromagnet as well as its greater distance from the sensor compared to the permanent magnets reduces its influence on the sensor reading. This leaves the flux density of the permanent magnets as the main source of sensor signal. The illustration in the bottom left of Figure 32 shows that the signal is greatest when the position of the permanent magnets is closest to the sensor. The illustration in the bottom right shows the converse condition where the signal is weakest with the armature magnets farthest from the sensor.

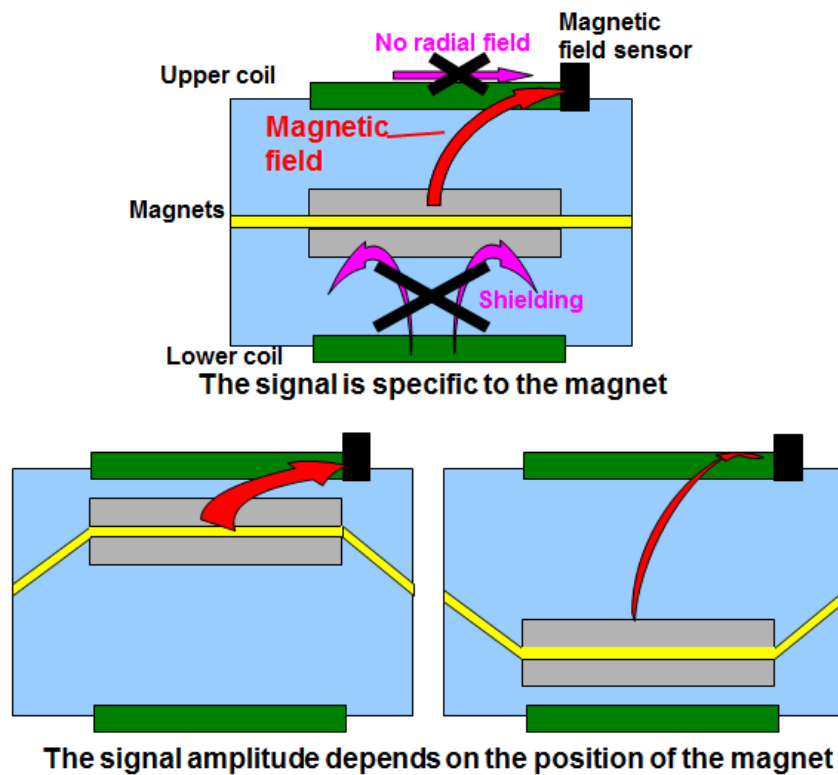


Figure 32 - Graphical depiction of the theory of applied sensing principles.

Laboratory Verification of Sensing Principles

The theoretical and FEM models developed in the previous section indicate that the ideal position for the sensor is located at the radially distal end of one of the electromagnets (see Figure 29). To prove the feasibility of a sensor system of this configuration, the prototype of Micropump v2.0 was fitted with a Hall Effect sensor at this location (see Figure 33), as well as at another location just above the top electromagnet and axially centered. Other locations were also tested to validate this specific position as the optimal location; however, these alternate locations producing intermediate results have been omitted from this report for clarity.

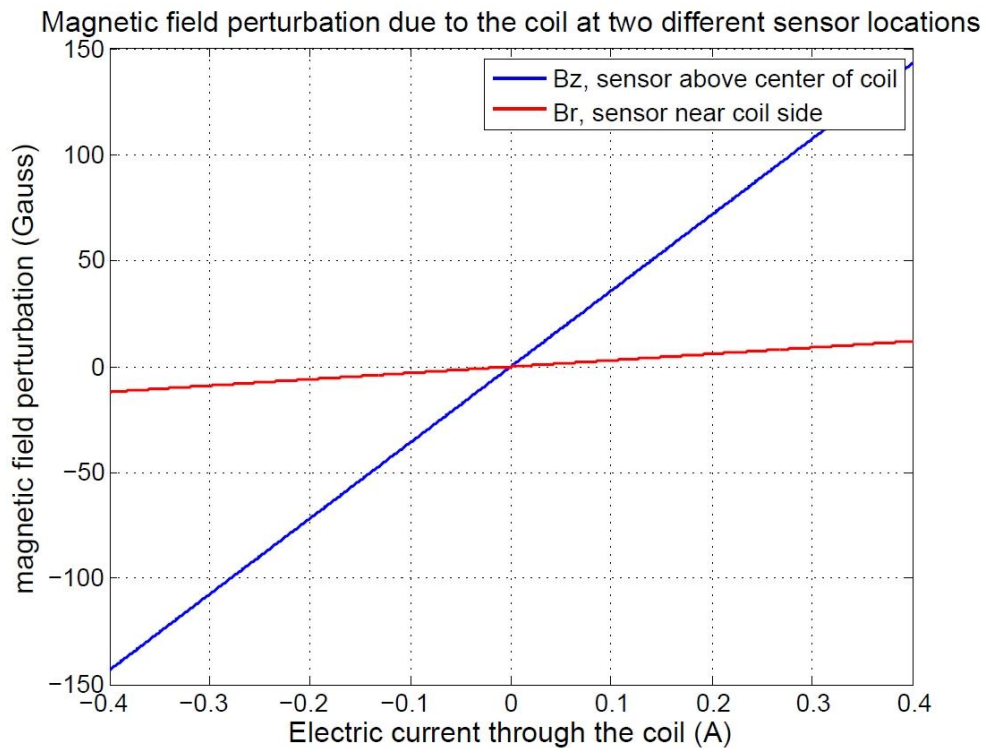


Figure 33 - Effect of the magnetic perturbation of the coils on the sensor measurement for a sensor located at the side location (red) vs. a centered classical symmetrical location (blue).

The sensor output as a result of energizing the two electromagnets (with the armature magnets absent) produced the data plotted in Figure 33. It can be seen that the effects on the magnetic field perturbation is almost 12 times less with the sensor in the theoretically determined

idealized orientation versus the sensor in the top position. Furthermore, it can be seen that this condition holds true for the full range of energizing currents from -400mA through +400mA applied to both coils in parallel with matched impedances. A second test was also performed to measure the magnetic field intensity in the various sensor positions as a function of armature magnet stroke displacement. The results of this test over the entire range of possible displacements, that is, from one side of the pump chamber to the other is plotted in Figure 34. In this test, the magnet was displaced using an externally applied physical force and the experiment was conducted in the absence of applied current to the electromagnets for isolation purposes.

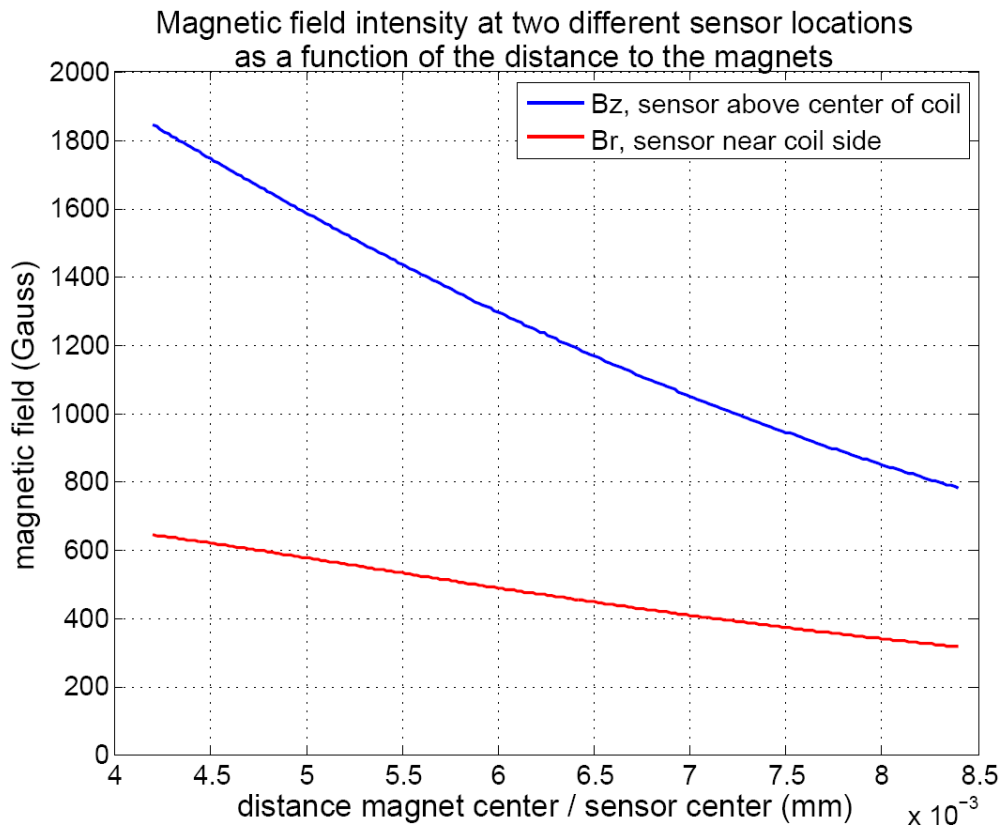


Figure 34 - Magnetic field as a function of the position of the magnet for a sensor located at the side location (red) vs. a centered classical symmetrical location (blue).

The theoretically determined optimal sensor location has proven to be very insensitive to the magnetic field of the coil \mathbf{B}_{coil} (Figure 33) yet still sensitive to the magnetic field of the armature

magnets $\mathbf{B}_{\text{magnet}}$ (Figure 34). In Figure 34 we see that with the sensor positioned at the theoretically optimal location, the signal output is approximately 3 times less than the corresponding signal measured with the sensor centered above the top electromagnet; however, the perturbation of the coils is about 12 times less. The result is a vastly improved signal / noise ratio with the sensor positioned at the idealized location.

The performance of the sensor feedback quality can be further analyzed and quantitatively defined by selecting the worst possible scenario where both $\mathbf{B}_{\text{magnet}}$ is at a minimum while \mathbf{B}_{coil} is at a maximum. In terms of actual operation, this situation is limited by the extent of travel due to the walls of the pump chamber (stroke length) and the maximum current before the resistance effects of the copper wire coil due to Joule heating. Nevertheless, we can calculate the worst case signal to noise ratio for the situation where the armature is furthest from the sensor whereby satisfying the worst possible values of the afore mentioned conditions to obtain a minimum expected value for the signal to noise ratio. The calculations can be summarized as follows:

$$\frac{(\mathbf{B}_{\text{magnet}})_{\text{min}}}{(\mathbf{B}_{\text{coil}})_{\text{max}}} \approx 45$$

$$\frac{\Delta \mathbf{B}_{\text{magnet}}}{\Delta Z} \approx 75 \text{ Gauss/mm}$$

Prototype Implementation

Subsequent to the provisional laboratory model verification of the idealized sensor location, another more specified clamshell was fabricated for the prototype “Micropump v2.0” with a permanently affixed magnetic feedback sensor. Magnetic perturbation data was again collected

for the complete range of coil currents -400mA through +400mA. The results of this test are contained in the plot of Figure 35

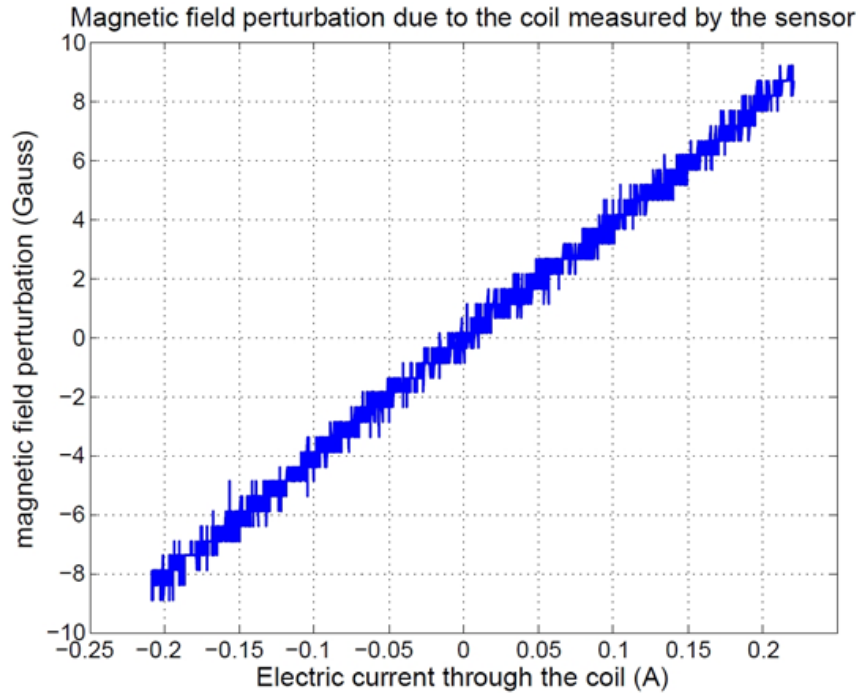


Figure 35 - Measurement of the magnetic perturbation due to the coils with the sensor being at side location.

Figure 35 illustrates the relationship between the electromagnetic energizing current as well as the quantification effects which results from the minimum sensitivity of the Hall Effect sensor. It should be noted that Figure 35 depicts the current carried by a single coil and therefore the x-axis values should be doubled to obtain true dissipation through the impedance matched electromagnetic driver coils. With the new permanently affixed sensor and prototype of “Micropump v2.0”, the idealized location sensor tests of Figure 34 were repeated to evaluate the magnetic field strength and sensitivity of the Hall Effect sensor within the finalized prototype device. The results of this study are contained in Figure 36.

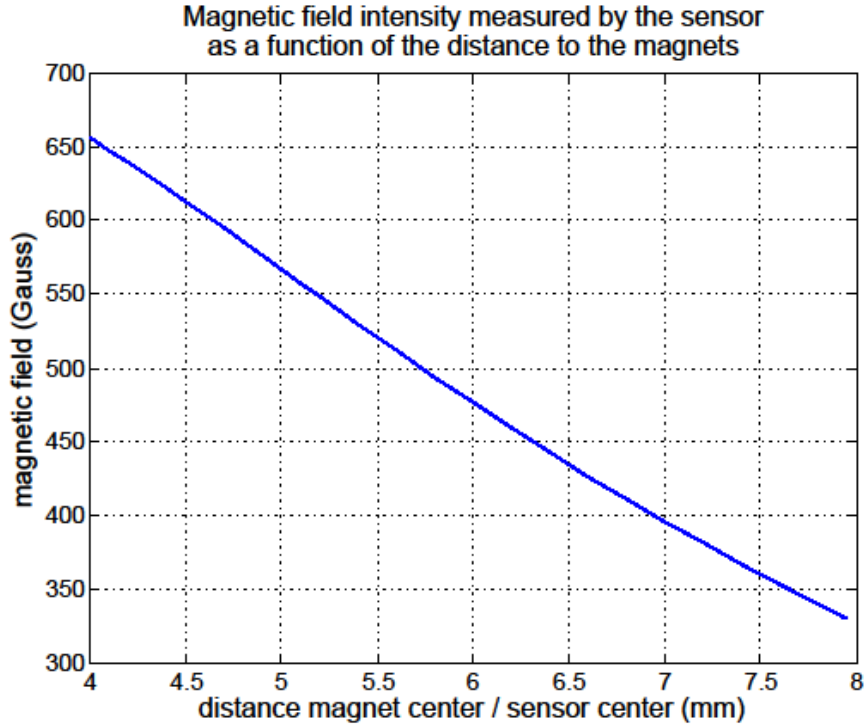


Figure 36 - Measurement of the magnetic field resulting from the displacement of the armature magnets, with the sensor positioned at the theoretically idealized location.

Reevaluating the signal to noise ratio and sensor sensitivity calculations performed earlier on the laboratory model reveal a strikingly similar set of quantitative assessments, namely:

$$\frac{(B_{magnet})_{min}}{(B_{coil})_{max}} = \frac{339 \text{ Gauss}}{8.5 \text{ Gauss}} \approx 40$$

$$\frac{\Delta B_{magnet}}{\Delta Z} = \frac{(661 - 339) \text{ Gauss}}{4 \text{ mm}} \left[\frac{2.5 \text{ mV}}{1 \text{ Gauss}} \right] \approx 201 \text{ mV/mm}$$

Control Principle

The data collected in the previous two sections will prove instrumental to the implementation of an accurate and robust control system. The aim of the embedded control system is to accurately position the magnets at any desired location between the two distal walls of the pump chamber.

Unfortunately, this goal is hindered by the noise present in the sensor feedback loop. To mitigate these effects and enhance the precision of the system, a sophisticated yet inexpensive auto-calibration and filtering solution is proposed and analyzed in the next section. A method of implementing the proposed electromagnetic noise suppression system is then presented in the section which follows.

Electromagnetic Noise Suppression

The proven “idealized” sensor location provides an optimized signal/noise ratio; however, it does not completely suppress the magnetic perturbation of the coils. Therefore, in order to enhance the accuracy of the system, a noise suppression scheme has been devised, based on the separation of the electromagnetic coil and permanent magnet contributions to the magnetic field. This separation is made possible by employing the use of current pulses.

Sensor Response to Pulse Excitation

When a step voltage is applied to the coils at $t = t_0$, the system response can be described as follows:

$$B_{sensor}(t) = B_{sensor}(t_0) + \Delta B_{coil}(t - t_0) + \Delta B_{magnet_displacement}(t - t_0)$$

Where $\Delta B_{coil} + \Delta B_{magnet_displacement}$ is the total change ΔB_{sensor} of the radial magnetic field measured by the sensor after a step voltage has been applied. ΔB_{coil} is the magnetic perturbation due to the coil, which is the total contribution of the coils to this change (a direct result of the magnetic field generated by the coils); $\Delta B_{magnet_displacement}$ is the contribution of the magnets to this change (a direct result of the magnet’s induced motion which alters the distance to the sensor, and therefore, the magnetic field measured by the sensor).

These two terms have different intrinsic response times:

- ΔB_{coil} is proportional to the current I flowing in the coil and therefore exhibits an electrical response time: $\tau_I = L/R$.
- $\Delta B_{magnet_displacement}$ is due to the displacement of the magnets. Once the magnetic field is applied, the magnets accelerate until they reach a nearly constant speed. The time needed to reach this constant speed will be a mechanical response time: τ_M .

Fortunately, in this system, τ_I is much less than τ_M . This implies that when a voltage step is applied, ΔB_{coil} will approach a final value while $\Delta B_{magnet_displacement}$ is still negligible. This yields:

$$\Delta B_{coil}(t) = B_{sensor}(t_0 + t) - B_{sensor}(t_0)$$

Provided the following conditions are satisfied: $t > \tau_I$ and $t \ll \tau_M$. With these conditions met, the ideal choice for t_{sample} can be calculated based on the inductance of the electromagnetic driver coils. For the coils used in this system with a resistance of about 42 Ohms and an inductance of about 3.8 mH, the time constant can be calculated as follows:

$$\tau_I = \frac{L}{R} = \frac{3.8 \text{ mH}}{42 \Omega} = 9.05 \times 10^{-5} \text{ s}$$

Delaying for a single time constant however will only achieve a current of 63.2% of the total steady state value. Delaying for 2, 3, 4 and 5 time constants will result in currents of 86.5%, 95.0%, 98.2%, and 99.3% of the total steady state current respectively. It is obvious that delaying for a longer period of time will bring the system closer to obtaining the steady state contribution of the coils, however, it also provides more time for the armature magnets to overcome inertia and begin physical motion which will reduce the accuracy of the result. An engineering compromise must therefore be enacted to delay the maximum amount of time

possible before the displacement of the armature magnets begins to have a significant effect on the sensor output. In this system, that is somewhere between two and three time constants which yields a current reading in the 90% range of the steady state current at a time t_{sample} of about 200 μs .

The preceding derivations show that it is possible to independently quantify the level of perturbation caused by the coils even while the armature magnets are installed within the pump by utilizing the described system characteristics resulting from current pulses applied to the coils and measuring the response at a time t_1 (before the magnet has time to move).

Measurements and Validation

To validate the effectiveness of the noise suppression system, data was first collected from the installed Hall Effect sensor to determine the actual magnetic contribution of the coils with respect to current. This was measured directly after removing the armature magnets from the pump and energizing the coils alone (see Figure 38, green curve). Note that the measurement is noisy, due to the intrinsic sensor noise level and to the limited analog-to-digital conversion accuracy at this level of precision (1Gauss = 1/2000 of the sensor's measurement range).

Based on the principles of the preceding section, the sensor response to short duration voltage/current pulses (see Figure 37) was measured and used to calculate the magnetic perturbation of the coil $\Delta B_{\text{coil}}(I)$ (see Figure 38, blue curve). To increase the robustness of this calibration, the following protocol was developed which leads to reproducible, accurate values over the full range of motion:

- Five pulses at +10 V are applied for a 1ms duration once every 10ms. Currents $I(t_0)$, $I(t_0 + t_1)$ and magnetic fields $B_{\text{coil}}(t_0)$, $B_{\text{coil}}(t_0 + t_1)$ are recorded.

- Five pulses at -10 V are applied for a 1ms duration once every 10ms. The corresponding currents and magnetic fields are once again recorded.
- $(\Delta B_{coil}(I))/I$ is calculated for each pulse; the average coil perturbation factor of the pulses $A_{coil} = \langle \frac{\Delta B_{coil}(I)}{I} \rangle$ is also calculated.
- A_{coil} is used in real-time during the subsequent measurements to derive the actual B due to the magnets alone, that is: $B = B_{meas} - (A_{coil} * I)$

The total duration of this protocol is 0.1 seconds. The blue curve obtained from this method shows good agreement with the green curve indicating little or no loss of accuracy in determining the contribution of electromagnetic coil perturbation with the armature magnets present. It should be noted that the discussed curve (the blue curve of Figure 38), which plots the value of the electromagnetic noise suppression result also displays quantization similar to the green curve. The quantization is however less apparent due to a faster sweep rate.

To further condition the signal and reduce the effects of signal quantization, a hardware implemented low pass filter was added to sensor feedback loop. Fortunately the quantization effects are fairly high in frequency allowing for the implementation of a low pass filter with a relatively high cutoff frequency. This allows us to filter out the majority of the noise components without introducing unnecessary time delays. The selected components which define the simple one-pole RC low pass filter are a 100 Ω resistor and a 0.22 μ F capacitor (see Figure 28) which yields a -3dB cutoff frequency of about 7kHz. The values which result from the implementation of this filter are plotted in Figure 38 as the red curve.

Notes regarding the measurements and resulting plots of Figure 37 and Figure 38:

- All measurements were made by sweeping the currents/voltages across their full range negative values to the positive values monotonically.
- The reduction of quantization of the electromagnetic noise curve (red line Figure 38) is a result of the filtering alone and not a result of noise canceling.

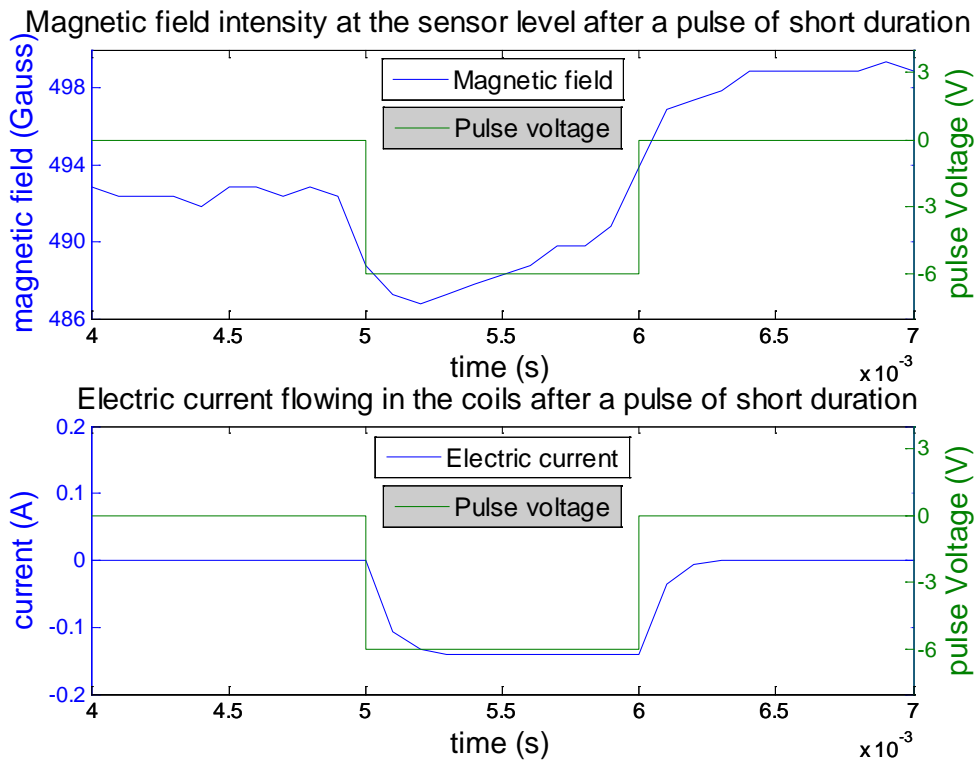


Figure 37 - Sensor response to voltage/current pulses.

The proposed perturbation measurement method is both quick and accurate, and can be used *in situ* with the armature magnets present within the pump. This is the first part of the auto-calibration process of the sensory system. The second part is described in the next section.

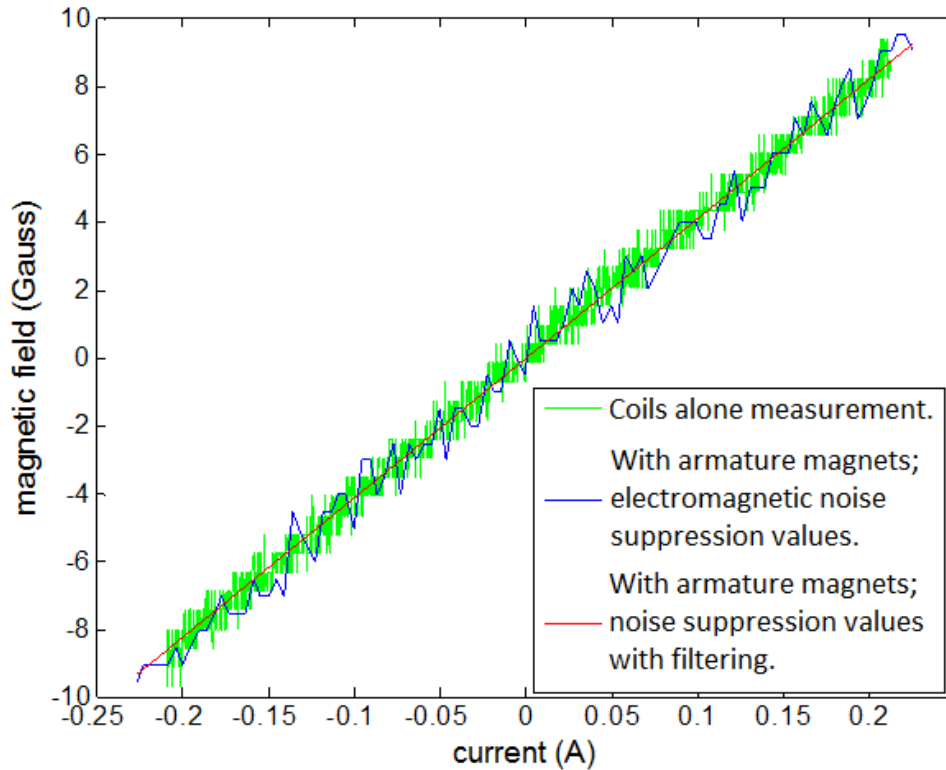


Figure 38 - Measurement of the electromagnetic coil perturbation using three different techniques.

Determination of Position

Once the magnetic perturbations generated by the electromagnetic coils are suppressed utilizing the methods outlined in the previous section, the measured sensor signal corresponds to the magnetic field $\mathbf{B}_{\text{magnet}}$ created by the armature magnets (and only the armature magnets assuming negligible outside interference) at the sensor location. Unfortunately, this signal will not be a linear function of the magnets' position; therefore a position determination algorithm was conceived that transforms the value obtained from the sensor into the magnets' actual position.

A magnet of magnetization \mathbf{M} creates a magnetic field at a point \mathbf{r}' exterior to the magnet defined as:

$$\mathbf{B}(\mathbf{r}') = -\frac{\mu_0}{4\pi} (\mathbf{M} \cdot \mathbf{grad}) \left[\int_{V_{\text{magnet}}} \frac{(\mathbf{r} - \mathbf{r}')}{\|\mathbf{r} - \mathbf{r}'\|^3} dV \right]$$

where \mathbf{r} defines the coordinates of the elementary volume dV inside the total volume of the magnet V_{magnet} .

In this case, the magnets have axisymmetric geometry, such that for each magnet, the above equation can be rewritten as:

$$B_r(z_b) = \frac{B_{rem}}{4\pi} \frac{\partial}{\partial z_s} \int_{z=z_b}^{z_b+h} \int_{r=0}^R \int_{\theta=0}^{2\pi} \frac{(r_s - r \cos\theta)}{[d_{\text{sensor-to-mag}}]^3} r d\theta dr dz$$

$$B_z(z_b) = \frac{B_{rem}}{4\pi} \frac{\partial}{\partial z_s} \int_{z=z_b}^{z_b+h} \int_{r=0}^R \int_{\theta=0}^{2\pi} \frac{(z_s - z)}{[d_{\text{sensor-to-mag}}]^3} r d\theta dr dz$$

$$d_{\text{sensor-to-mag}} = \sqrt{(r \sin\theta)^2 + (r_s - r \cos\theta)^2 + (z_s - z)^2}$$

where the reference (0,0,0) of the r, z, θ coordinates is the center of the pump chamber. B_{rem} is the remanent magnetic field of the magnet. (r_s, z_s) are the coordinates of the center of the sensor; R is the radius of the magnet, h is the thickness of the magnet, and z_b is the coordinate at the bottom of the magnet.

Once the effects of the coils are suppressed, the magnetic field B_{sensor} measured by the sensor is the superposition of the magnetic field of both magnets. This can be stated mathematically as:

$$B_{\text{sensor}} = B_{r_mag1} \left(z_m + \frac{h_m}{2} \right) + B_{r_mag2} \left(z_m - h - \frac{h_m}{2} \right)$$

where $B_r(z)$ is defined by the first triple integral function stated above, h_m is the thickness of the membrane and z_m is the position of the membrane (the center of the magnets) that we wish to determine with the sensor.

Note that this equation for determining B_{sensor} depends only on the variable we wish to measure, z_m . However, this equation cannot be used to directly obtain z_m , as its integrations do not provide an analytic solution and it is therefore impossible to obtain the inverse function. As a result, a lookup table of this equation along with the corresponding reverse lookup table must be created.

The real system is not ideal and the parameters of the equation can only be known to a limited precision. Therefore, the simulated values of z_m as a function of $B_{measured}$ will be different from the real values. However, it is possible to significantly reduce the discrepancies between the real and simulated values by utilizing the corrected simulated values $B_{sim_cor}(z_m)$, namely:

$$B_{sim_cor}(z_m) = B_{sim}(z_m) \cdot \left[f_{max} + \left(\frac{z_m - z_{B_{max}}}{z_{B_{min}} - z_{B_{max}}} \right) * (f_{min} - f_{max}) \right]$$

where:

$$f_{max} = \frac{B_{max_meas}}{B_{max_sim}}$$

$$f_{min} = \frac{B_{min_meas}}{B_{min_sim}}$$

This equation enables the use of the corrected simulated values (which are very close to the real values) to accurately determine the position of the magnet, provided that we know the real values of B for two cases: $z_{B_{max}}$ and $z_{B_{min}}$. Fortunately, $z_{B_{max}}$ and $z_{B_{min}}$ are easy to obtain,

as they represent the position of the magnet when it hits the lower wall ($z_{B_{max}}$) and upper wall ($z_{B_{min}}$).

Utilizing this principle, the position of the magnet may be obtained through the following protocol:

1. According to the dimensions of the pump, the size and material of the magnets, and the position of the sensor, a MATLAB simulation is performed utilizing the equation for B_{sensor} (see Figure 39 green curve).
2. A lookup table is generated and subsequently recorded in the memory of the microcontroller (during the burning of the program).
3. Each time a new pump is inserted, the magnets are driven to their minimum and maximum positions and the corresponding magnetic fields are measured and recorded (see Figure 39 blue curve).
4. The equation defining $B_{sim_cor}(z_m)$ is used to modify the lookup table and create the reverse lookup table which provides z_m as a function of $B_{measured}$ (see Figure 39 red curve).
5. The value of z_m is obtained from $B_{measured}$ in real time using a linear regression of the reverse lookup table entries (see Figure 39 black curve).

The third and fourth steps are performed automatically and do not exceed five seconds in duration. The magnetic field emanating from the magnets was measured by the sensor as a function of the magnets position and plotted (see Figure 39). It is then compared to: (i) the simulated magnetic field; (ii) the corrected simulated values according to the $B_{sim_cor}(z_m)$

equation; (iii) the real-time linear regression of the lookup table which was created using the previously described protocol.

The maximum error between the real values and the calculated reverse lookup table values were determined to be:

$$Error_{max} = 0.03mm = 0.75\%$$

That is, the maximum error of the total range of the armature magnets within the pump chamber is 0.75%. Furthermore, this also indicates that the volumetric precision is 0.75% of the displaced chamber volume.

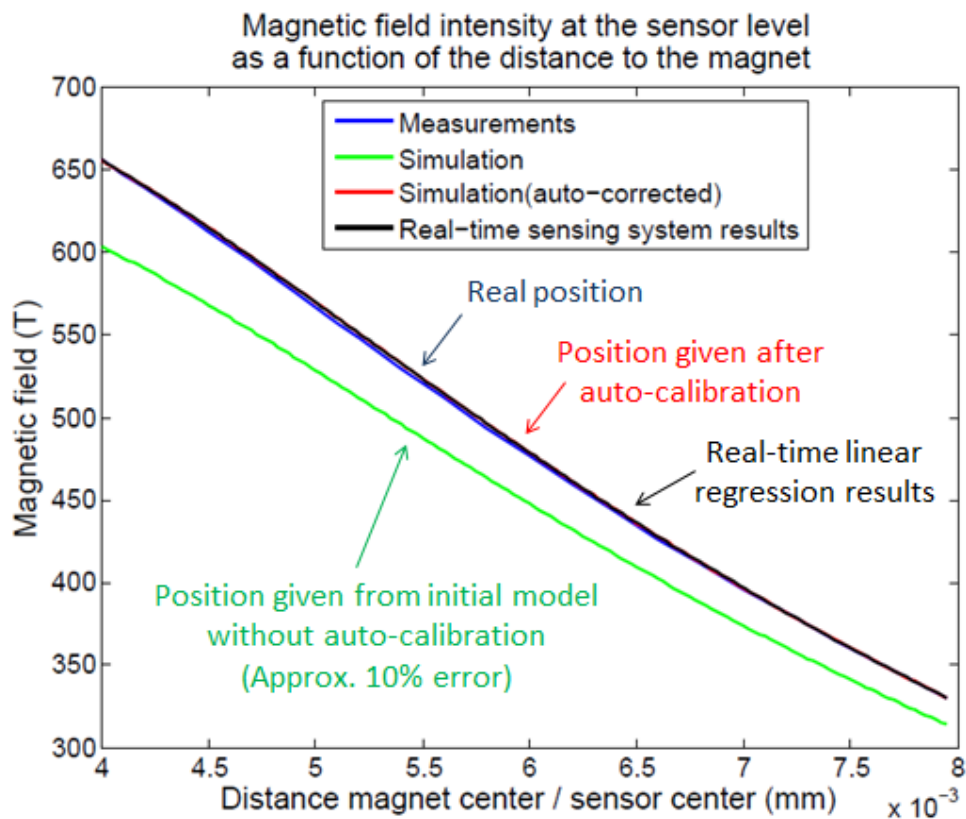


Figure 39 - The experimentally measured magnetic field as a function of the position of the magnets; compared with the simulation, the corrected simulation, and the real-time sensing system results.

To summarize the results of this section, the auto-calibration protocol which is employed, while using a low-cost sensory system, is able to measure the position of the magnets and hence the deformation of the membrane with a precision which exceeds the requirements of most applications.

Control Implementation

The response of the system to a current flowing through the coils has been measured and is depicted in the hysteresis diagram of Figure 40. The system clearly exhibits mechanical hysteresis; moreover, the current - and hence the magnetic field - is neither a linear nor a bijective function of the voltage, due largely to the heating of the coils. This eliminates any possibility of controlling the system with an open loop signal.

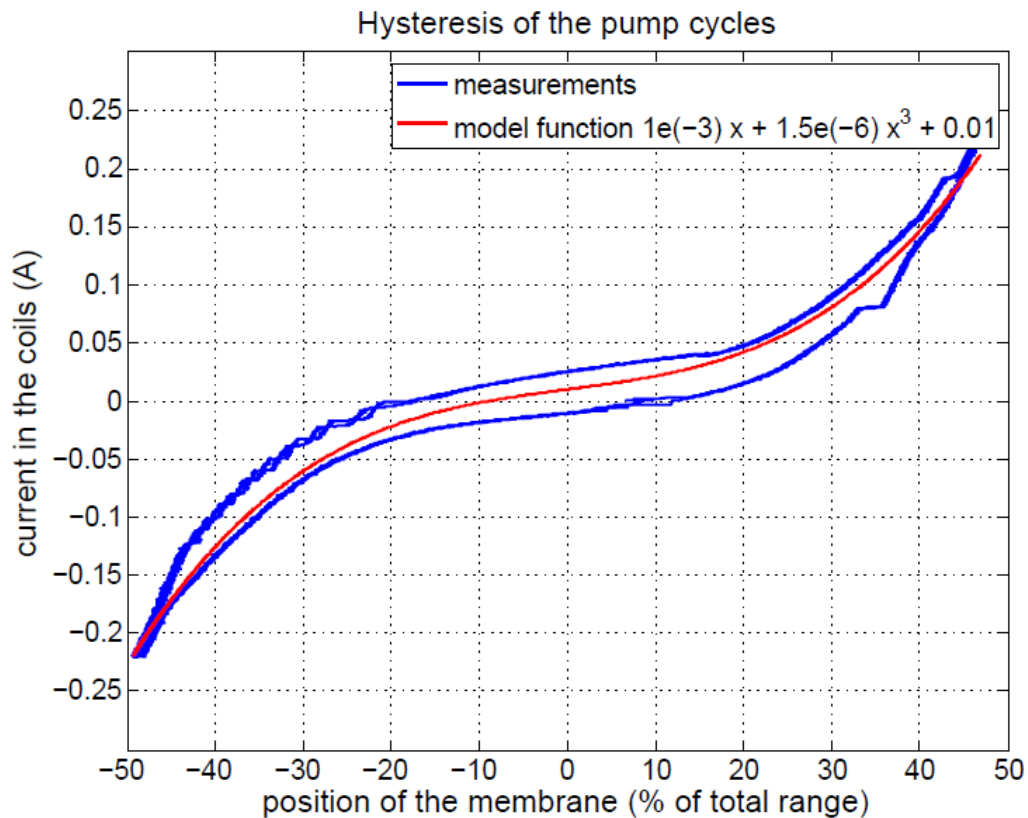


Figure 40 - The experimentally determined mechanical hysteresis as compared to the simulated function model.

To overcome the mechanical limitations of this system, control is accomplished through the implementation of a modified PID controller. The modification mainly consists of restricting the change in set-point rate to avoid oscillations which would otherwise result from the tilting of the magnet. This method is effective at removing the oscillations because the tilting of the magnet is mainly caused by the quick inversion of the surrounding magnetic field. Figure 41 contains a flow chart depicting the principle of control.

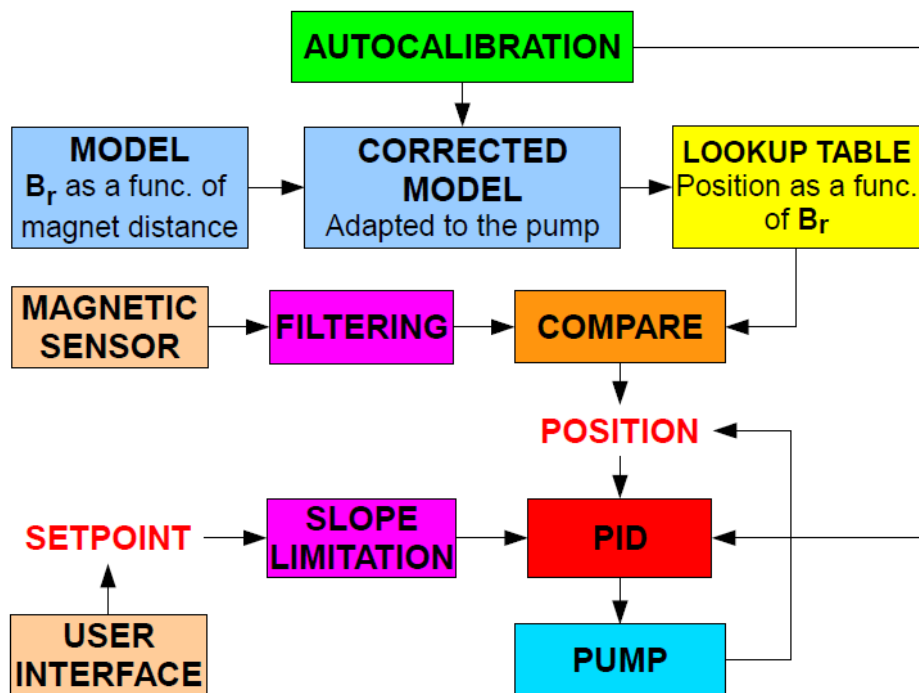


Figure 41 - Flow chart of the sensing and control strategy.

The flowchart of Figure 41 depicts the culmination of all of the characterization and procedures described in the preceding sections as well as the interactive relationships between them. The entire control system is implemented within the embedded microcontroller and support hardware of the controller circuit (see Figure 22 and Figure 28). The results of this implementation and control scheme are presented in the next section.

Results and limitations

This section presents the operational results of the position sensing system which has been developed in this chapter. The performance of the system is evaluated by subjecting the pump to a variety of classical set-point progressions (i.e. step functions, ramp functions and partial steps) while operating under multiple conditions (i.e. in air, or pumping fluid). In each case, overlay plots of the results are presented depicting both the command position with respect to time as well as the real-time response of the armature.

Unloaded System Response

The performance of the loaded system (examined in the next section) is of the greatest concern as it represents the operation of the pump while subjected to real world loads during actual intended operation, however, the performance of the unloaded system cannot be overlooked as it represents the systems response in the event of fluidic loss (i.e. if the pump becomes drained and starts pumping air). Furthermore, examination of the unloaded response can be rather insightful as it provides the natural response of the system without the effects of dampening due to the presence of fluid in the pump chamber. In fact, while the loaded system introduces time delays due to the requirement to overcome inertia and displace fluid through the inlet and outlet ports, tubes, and valves; it turns out that the unloaded system is actually the more difficult system to control as the dampening effects of the fluid in the pump chamber tend to stabilize the system reducing oscillations and overshoot.

While oscillatory and overshoot effects are more prominent in the unloaded system, the robustness of the control implementation allows for exceptional control. The plot of Figure 42 depicts the unloaded system response to a variety of classical set-points. The coefficients of the PID controller were carefully tuned to maximize response time while minimizing overshoot and

oscillations. We can see from this plot that despite the hysteresis (see Figure 40) which typically prevents a system from obtaining results less than the hysteresis amplitude; the Micropump v2.0 prototype response is both quick – time response for high amplitude set-points change – and accurate – zero static error and maximum overshoot of just 2%. Furthermore, for commanded ramp functions where the set-point to actual position error is always relatively small, the system response tracks the commanded position with an exceptional degree of accuracy.

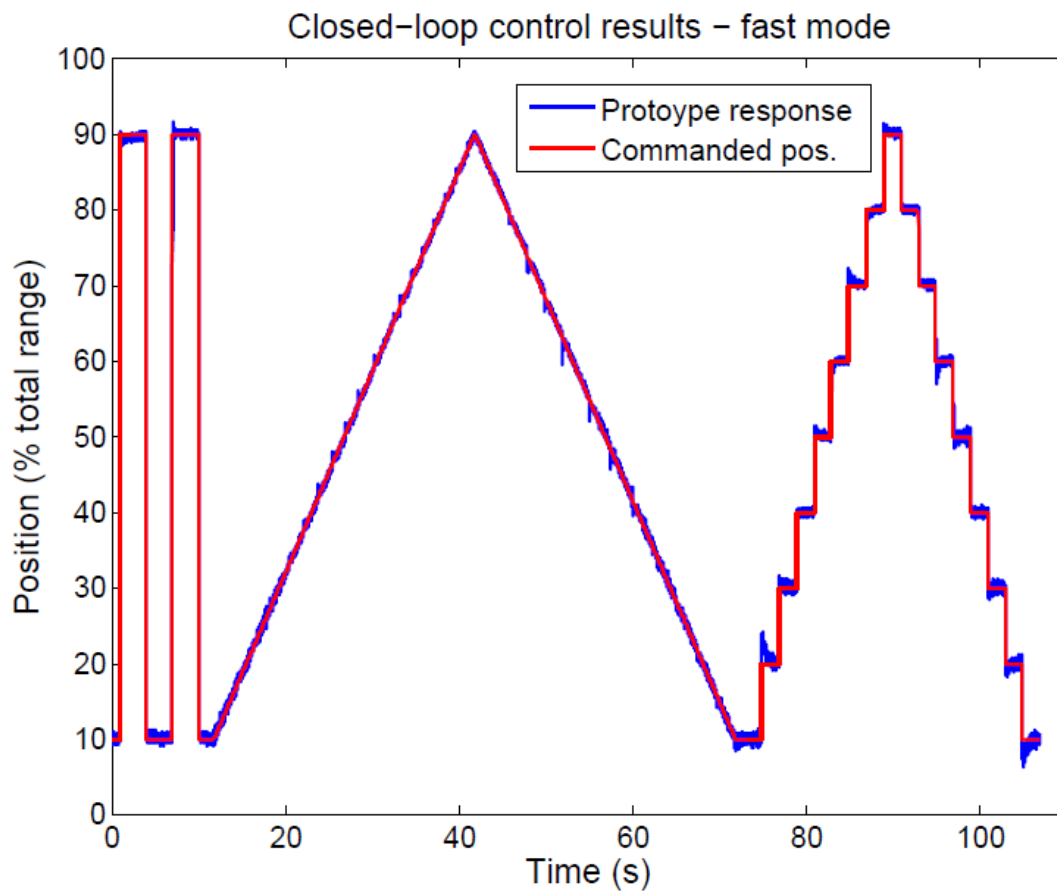


Figure 42 - Controller performances (blue) evaluated for a variety of classical set-point progressions (red).

Loaded System Response

The loaded system response was obtained by allowing the prototype to pump distilled water between two reservoirs while collecting data via the RS-232 serial port of a PC. A photograph of

the pump in action is depicted in Figure 43 where water expelled from the outlet tube is clearly visible above the reservoir on the far right.



Figure 43 - Micropump v2.0 pumping distilled water.

After the pump was fully primed with distilled water, the system was commanded to follow set-points of the following progression:

1. Commanded to the zero position (halfway between the top and bottom walls of the pump chamber).
2. A rapidly rising ramp command (15% per second) ending at +30% of total armature displacement.
3. A slowly decreasing ramp command (7.5% per second) from +30% to -30% of total armature displacement.
4. Commanded to maintain a position at -30% for a period of 2 seconds.
5. A slowly rising ramp command (7.5% per second) from +30% to 0% of total armature displacement.

6. Commanded to maintain position at the zero point.

The system response to this commanded series of ramp progressions are plotted in Figure 44 where the commanded set-point progressions are depicted in red and the actual position of the armature is depicted in blue. Similar to the response of unloaded system, we again see excellent tracking of the armatures position to the commanded set-points. The relatively slow change in set-points combined with the oversized flow channels of the Micropump v2.0 prototype provided ample time for fluid flow virtually eliminating armature deviations from the set-point due to physical interactions with the fluid. Furthermore, as postulated the presence of the water in the pump chamber added further dampening to the system reducing oscillatory behavior about the set-point progressions.

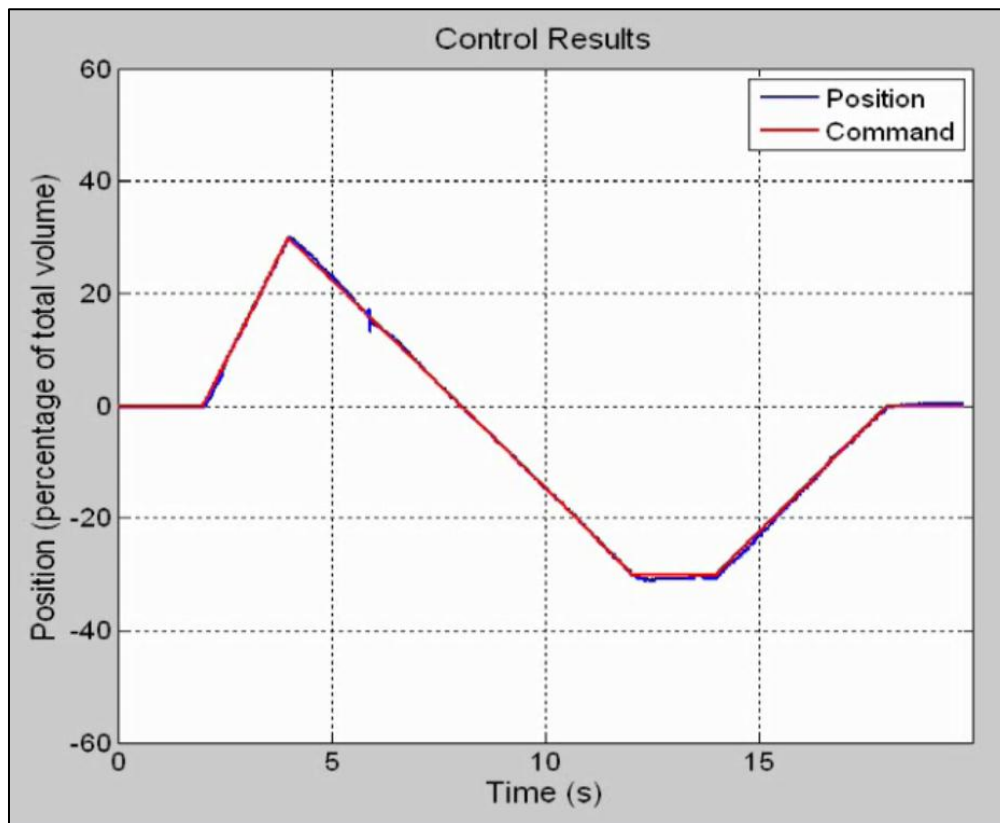


Figure 44 - Pump response to various ramp commands while pumping distilled water.

Another set of system response tests were subsequently conducted again with the pump fully primed with distilled water. This time the system response is evaluated in response to a step set-point progression as follows:

1. Commanded to the zero position (halfway between the top and bottom walls of the pump chamber).
2. Commanded to a position at +30% of total armature displacement for 2 seconds.
3. Commanded to a position at -30% of total armature displacement for 2 seconds.
4. Commanded to maintain position at the zero point.

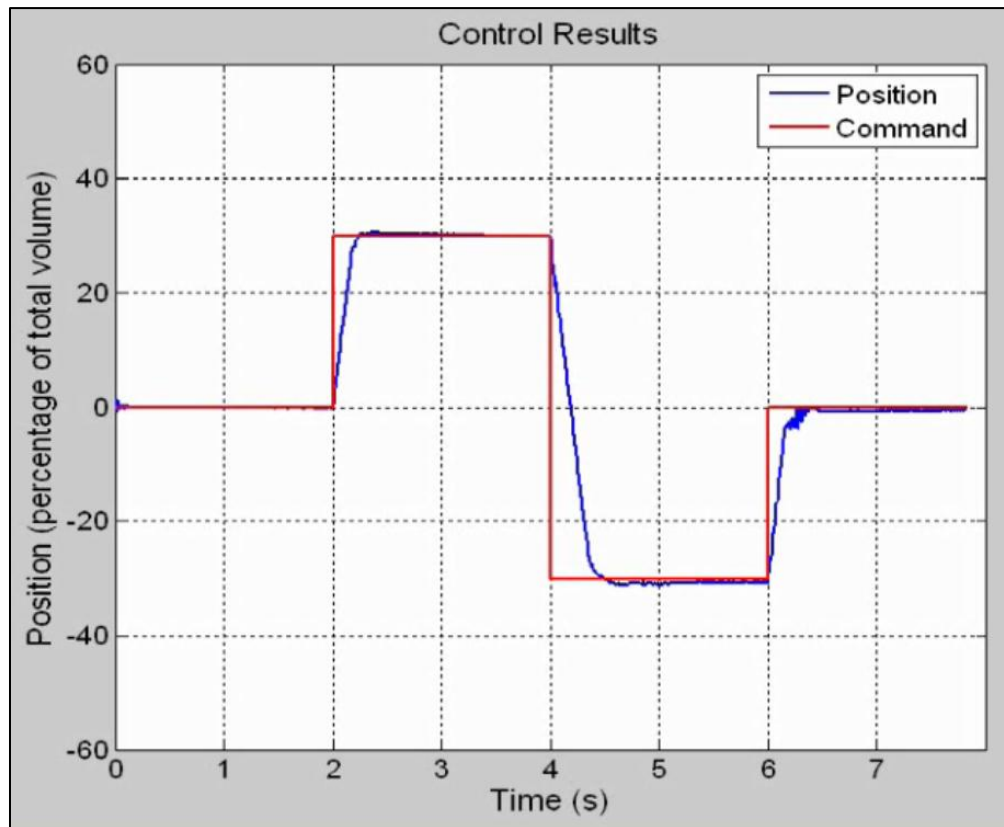


Figure 45 - Pump response to step commands while pumping distilled water.

The system response to this commanded series of step progressions are plotted in Figure 45 where the commanded set-point progressions are depicted in red and the actual position of the

armature is depicted in blue. Unlike the response of the unloaded system, we now see deviations from the set-point due to physical interactions with the fluid; however, the system still provides zero steady state error with a minimum of overshoot. Furthermore, as postulated, the presence of the water in the pump chamber added further dampening to the system reducing oscillatory behavior about the set-point progressions. Since the deviations from the set-point are due to physical interactions with the fluid and not the result of controller inadequacies, the system must simply wait for an appropriate amount of time to allow for the armature to displace the fluid before arriving at the desired set-point. Methods of improving the system response in spite of these physical limitations are discussed in the next section.

Discussion and Limitations

Analysis and characterization of the Micropump v2.0 prototype has led to the novel magnetic positional feedback implementation and devised method of control which was introduced early in this chapter. The theoretical and later laboratory verified sensitivity of the feedback loop was determined to exhibit a high level of accuracy despite the overall low cost of the hardware. Unfortunately, the feedback loop was plagued with noise generated by the electromagnetic driver coils which limited the overall achievable resolution of the armature position.

To overcome these limitations, an innovative electromagnetic noise suppression system was conceived and modeled mathematically. The insight came from the realization that the magnetic field generated by the electromagnetic coils was established far quicker than any positional changes in the resulting physical motion of the armature (delayed mainly due to inertia). By delaying for a short period of time before the displacement of the armature magnets begins to have a significant effect on the sensor output, a sensor reading can be taken which corresponds to the perturbation of the electromagnetic coils alone. Identifying this value

independently allows the control system to subtract its contribution from the overall measured value yielding a signal which almost completely suppresses the perturbations of the coils. Following the development of a mathematical model, laboratory measurements were conducted to collect real-world data and verify the validity of the method. The laboratory testing proved this method to be both quick and accurate at suppressing the perturbations from the coils.

With the magnetic perturbations generated by the electromagnetic coils suppressed, the measured feedback sensor signal corresponds to the magnetic field created by the armature magnets alone. Unfortunately, this signal proved not to be a linear function of the magnets position, and as a result, a position determination algorithm had to be conceived. Using a novel auto-calibration method and a digitally implemented reverse lookup table, positional error of less than 0.75% was obtained.

Using the conditioned and positionally mapped feedback sensor data, a PID based control system was created to accurately drive the armature to any desired position within the pump chamber. The PID controller not only overcomes the effects of hysteresis caused by the membrane but also maintains the armatures position about a desired set-point. This provides a means for delivering sub-stroke volumes of fluid from the pump. The tuned embedded PID controller was found to track the commanded position signal to a high degree of accuracy in all but the loaded step response (see Figure 42, Figure 44, and Figure 45).

Since the response delays of Figure 45 are a result of physical interactions with the fluid and not a shortcoming of the control system itself, the response can be enhanced by simply increasing the available force which can be developed by the armature. This can be accomplished through a variety of methods including increasing the driving voltage, reducing the

resistance of the coil (thereby increasing the current), or increasing the remanent flux density of the armature magnets. Alternatively, the response can be improved (to a point) by reducing the resistive effects of the fluid flow path including reducing the forward pressure drop across the valves, increasing the cross-section of the fluid channels, reducing corners and directional changes of the fluid, reducing the tube length of the inlet and outlet tubes, and reducing the overall head pressure required to be developed by the pump. Unfortunately since many of these later physical optimizations have already been made in this pump prototype, the former method (that of increasing the power delivered to the armature) is the only realistic method available to achieve significant gains.

Nevertheless, the performance of the feedback control system was found to be extremely impressive. Furthermore, it should be noted that while not presented quantitatively, the armature response to external perturbations (position disruptions from pushing the magnets with a plastic rod) showed exceptional recovery response times returning back to the set-point once the disturbance force was removed. The system recovered with a minimal amount of overshoot and exhibited rapid oscillation dampening even when released from a large perturbation displacement.

Unfortunately one key aspect of performance, which has been overlooked in the discussion until this point, reveals a fundamental flaw of using single sensor feedback for this system: armature tipping. While the noise suppression, positional mapping algorithm and control system have all proven to be extremely effective, they can only operate on the information that the sensor itself supplies. In this case, the sensor provides feedback data which is most sensitive to the magnetic field produced by the armature magnet nearest the sensor. This means that the feedback system is unable to resolve, and therefore unable to correct for, tipping

of the armature magnets. This can be a problem for sub-stroke deliveries as the inability to track the tipping of the magnets can lead to volumetric delivery errors. This topic, along with a potential solution is discussed further in the next chapter.

CHAPTER 7 – Future Work

This thesis discusses the development of a feedback controlled, electromagnetically actuated, compact micropump for fluidic/drug delivery applications. The micropump may be considered an extremely low cost and disposable pump thanks to a two-component architecture, non-contact actuation, and the use of standard microfabrication techniques. Closed-loop control of the micropump was achieved by adding inexpensive and accurate sensors to the reusable component without adding the burden of additional cost to the disposable component. Despite its low fabrication cost and small physical size, the micropump performed well and the results were very positive. This is largely due to optimizations of the pump geometry and dimensions. The prototype is small and compact with fully incorporated check valves and an embedded electronic driver circuit. Proposed future work will continue the miniaturization and address enhancements of the flow control for more accurate volumetric delivery applications.

Reduced Scale Pump

To continue the research of miniaturization and challenge the limits of production using traditional micromachining techniques, an alternative prototype was introduced at a reduced scale. From the beginning of the miniaturized pump design phase, scaling issues have hampered the objective performance. First, the embedded valves introduced in Micropump v2.0 which fit conveniently on the front face of the pump body became geometrically impossible to implement with the design of Micropump v2.1 forcing the proposed adoption of a parallel-planer design (see Figure 46).

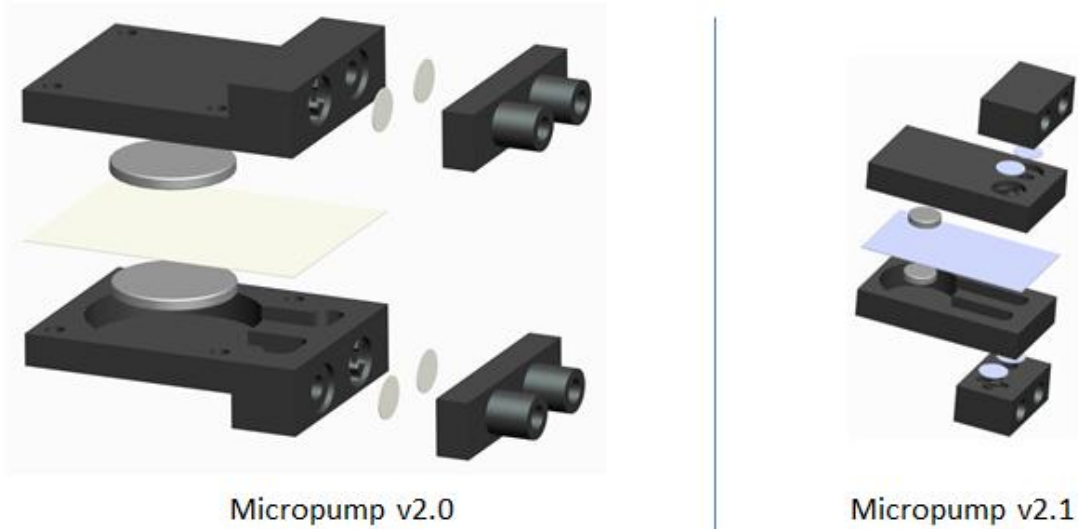


Figure 46 - Comparison of design between Micropump v2.0 and Micropump v2.1.

The new design changes affected the flow profile and additional simulations and analysis were required to optimize the performance and minimize pressure losses. Unfortunately, other unforeseen consequences of scaling and physical interactions at this level proved to dominate performance effects as discussed later in this chapter.

Prototype, Results and Discussion

The reduced scale prototype “Micropump v2.1” achieved overall dimensions of just 9.5 x 17.5 x 13.5 mm (see Figure 47) while still maintaining the isolated dual chamber design of the second prototype “Micropump v2.0” which allows for the simultaneous pumping of two dissimilar fluids. A reduction in driving voltage to just 3 Volts was also obtained by decreasing the resistance of the electromagnetic driver coils.

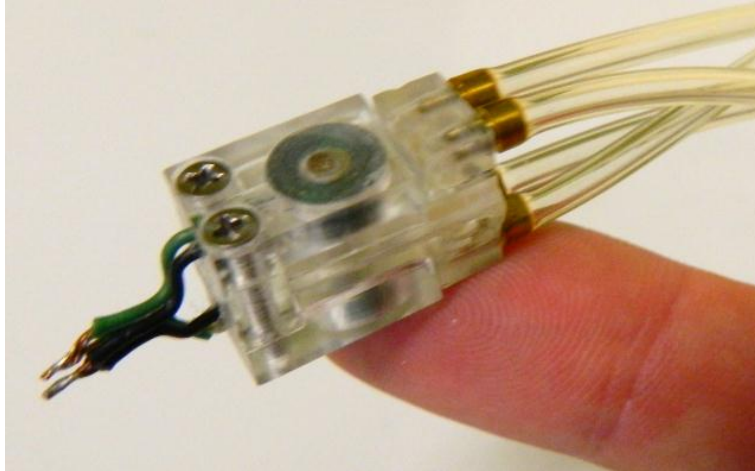


Figure 47 - Photograph of Micropump v2.1 prototype.

Working within the limited conditions of this miniaturized pump, the prototype was primed with distilled water and energized using the same pump controller circuit developed for Micropump v2.0. A software controlled pulse-width-modulated output was used to limit the overall power delivered to the pump. Operating conditions were as follows:

- Total resistance of both electromagnetic coils in parallel: 5.2 Ohms
- Current delivered to each coil: approx. 580 mA
- Driving frequency: Varied from 0 to 15 Hz in 1 Hz steps. (First measurement was taken at 0.1Hz instead of zero to evaluate performance of extremely low actuation periods)

Initial test results of the proposed prototype for each of the sampled frequencies are depicted in the plot of Figure 48. One prominent distinction which can be made as compared to previous prototype test results is the significant increase in resonant frequency; from 2 Hz for the Micropump v2.0 to around 8Hz for Micropump v2.1. This is expected as the resonant frequency of most systems increases as the system is miniaturized. One characteristic which was not expected, however, is the relatively poor performance experienced at low driving frequencies.

Subsequent analysis combined with careful observation revealed that this deficiency of performance was related to valve operation. New issues arose with regard to the performance of the miniaturized free floating membrane valves which were not a factor at the scales of the previously produced prototypes. These issues include both manufacturing issues such as machining burrs and physical issues such as valve membrane stiction.

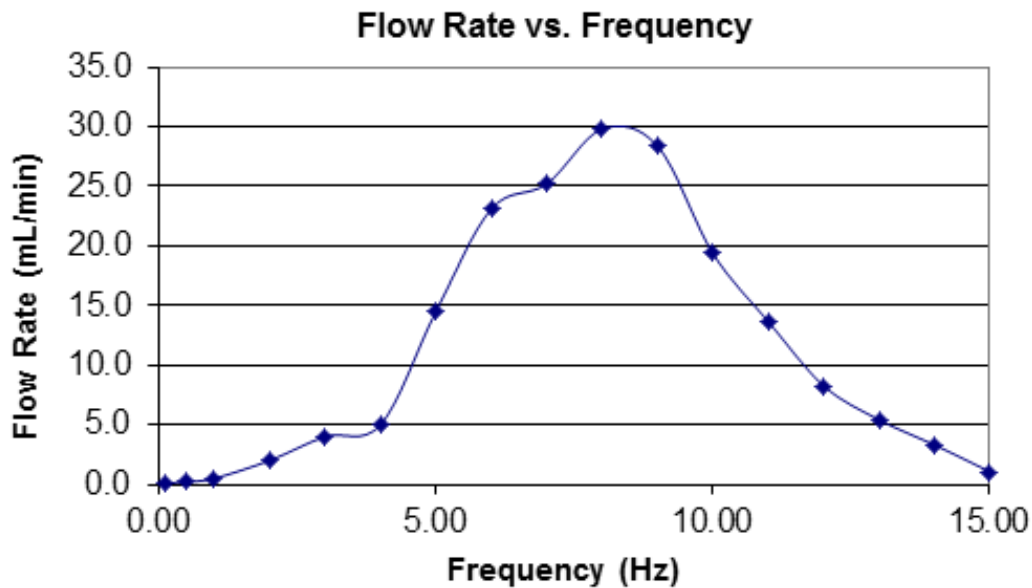


Figure 48 - Flow rate as a function of excitation frequency for the Micropump v2.1 prototype.

Unfortunately, while Figure 48 is a fairly good representation of pump performance, it was difficult to obtain consistent results in testing this prototype due to valve performance issues.

Valve Scaling Issues

This section discusses the main issues related to reduced scale operation of the free floating membrane based valves developed earlier. Specifically, issues related to micromachining such as machining burrs and physical issues such as valve membrane stiction are discussed and the implications explored.

Machining Burrs

Burrs and other artifacts of traditional machining processes which are often cleaned up by hand or neglected in macroscopic designs create challenging problems for the fabrication of micro-machined components which often fail to function without the removal of these artifacts. Complicating the removal process is the sheer scale of these features which often makes manual removal difficult or impossible without the risk of damaging the desired structure.

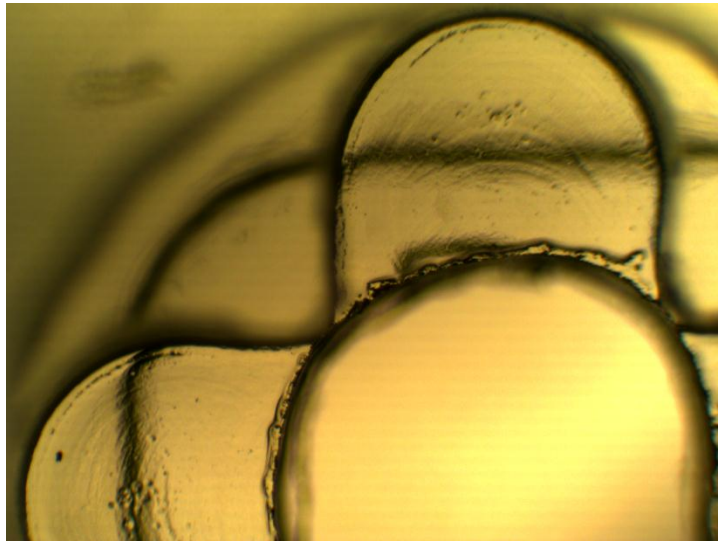


Figure 49 – 40x magnified view of a micro-machined valve used in Micropump v2.1.

In the production of the Micropump v2.1 prototype, machining burrs became a very serious issue especially when they occurred within the valve compartments. The micro-machined holes which looked virtually “perfect” to the naked eye were revealed to contain burrs and other defects when viewed under a microscope (see Figure 49), which in some cases led to leaks around the sealing membrane. This became one of the contributing factors to the loss of valve performance and inconsistent behavior.

Valve Membrane Stiction

Another more serious issue related to valve operation in Micropump v2.1 is that of valve membrane stiction. In this case, we define valve membrane stiction as any adhesion event which results in the membrane (in part or in whole) remaining stuck to a valve upstream wall in spite of fluid flow through the valve. The implications of such event can be disastrous typically resulting in partial or total loss of the rectifying properties of the valve.

These issues arise with valve scaling due to the smaller forces imparted through fluid flow through the valve as well as increased relative contributions of surface adhesion forces due to miniaturization. Possible solutions to this phenomenon include increasing the relative diameter of the free floating membrane to the chamber diameter and/or reducing the surface adhesion effects through a lubricant or change in material selection. Unfortunately the former modification will also result in increased pressure drops across the valve during forward flow operation.

Valve Scaling Conclusion

Valve fabrication and design for reliable operation at these reduced scales has been revealed to be very challenging. In the author's opinion, valve design will prove to be the most challenging aspect of further pump miniaturization and a determining factor of performance. It is therefore suggested that future work focus on resolving the issues associated with valve scaling as a precursor to further reductions in size.

Acknowledgement

I would like to acknowledge that some of the material and figures found in Chapters 5 and 6 of this thesis is also contained in a published article which I co-authored entitled "Low-cost high

performance disposable micropump for fluidic delivery applications” and can be found in the July 2011 issue of *Sensors and Actuators A: Physical*, published by Elsevier B.V.

Bibliography

- [1] B. Iverson and S. Garimella, "Recent advances in microscale pumping technologies: a review and evaluation," *Microfluid Nanofluid*, vol. 5, pp. 145-174, 2008.
- [2] D. Laser and J. Santiago, "A review of micropumps," *Journal of Micromechanics and Microengineering*, vol. 14, no. 6, pp. 35-64, 2004.
- [3] W. Inman, K. Domansky, J. Serdy, B. Owens, D. Trumper and L. Griffith, "Design, modeling and fabrication of a constant flow pneumatic micropump," *Journal of Micromechanics and Microengineering*, vol. 17, no. 5, pp. 891-899, 2007.
- [4] A. Manz, N. Graber and H. Widermer, "Miniaturized total chemical analysis systems: a novel concept of chemical sensing," *Sensors and Actuators B*, vol. 1, pp. 244-248, 1990.
- [5] B. Chen, D. Lee, J. Woolman and G. Carman, "Development of large flow rate, robust, passive micro check valves for compact piezoelectrically actuated pumps," *Sensors and Actuators A: Physical*, vol. 117, no. 2, pp. 325-330, 2005.
- [6] P. Woias, "Micropumps-past, progress and future prospects," *Sensors and Actuators B*, vol. 105, no. 1, pp. 28-38, 2005.
- [7] F. Amirouche, Y. Zhou and T. Johnson, "Current micropump technologies and their biomedical applications," *Microsystem Technologies*, vol. 15, pp. 647-666, 2009.
- [8] E. Meng, "MEMS technology and devices for a micro fluid dosing system," California

- Institute of Technology, Pasadena, 2003.
- [9] N. Tsai and C. Sue, "Review of MEMS-based drug delivery and dosing systems," *Sensors and Actuators A*, vol. 134, pp. 555-564, 2007.
- [10] S. Shoji and M. Esashi, "Microflow devices and systems," *Journal of Micromechanics and Microengineering*, vol. 4, no. 4, pp. 157-171, 1994.
- [11] N. Nguyen, X. Huang and T. Chuan, "MEMS-micropumps: a review," *Journal of Fluids Engineering*, vol. 124, no. 2, pp. 384-392, 2002.
- [12] D. Xu, G. Wang, Y. Zhou, A. Yu and B. Cai, "Characteristics and fabrication of NiTi/Si diaphragm micropumps," *Sensors and Actuators A*, vol. 93, pp. 87-92, 2001.
- [13] S. Guo and T. Fukuda, "Development of the micro pump using ICPF actuator," in *IEEE International Conference on Robotics and Automation*, 1997.
- [14] R. Zengerle, A. Richter and H. Sanhmaier, "A micro membrane pump with electrostatic actuation," in *Micro Electro Mechanical Systems, 1992, MEMS '92, Proceedings. An Investigation of Micro Structures, Sensors, Actuators, Machines and Robot. IEEE*, Travemunde, Germany, 1992.
- [15] O. Francias and I. Durour, "Enhancement of elementary displaced volume with electrostatically actuated diaphragms: application to electrostatic micropumps," *Journal of Micromechanics and Microengineering*, vol. 10, no. 2, pp. 282-286, 2000.
- [16] M. Kock, N. Harris, A. Evans, N. White and A. Brunnschweiler, "A novel micromachined

- pump based on thick-film piezoelectric actuation," *Sensors and Actuators A*, vol. 70, pp. 98-103, 1998.
- [17] S. Bohm, W. Olthuis and P. Bergveld, "A plastic micropump constructed with conventional techniques and materials," *Sensors and Actuators A*, vol. 77, pp. 223-228, 1999.
- [18] C. Schabmueller, M. Koch, M. Mokhtari, A. Evans, A. Brunnschweiler and H. Sehr, "Self-aligning gas/liquid micropump," *Journal of Micromechanics and Microengineering*, vol. 12, pp. 420-424, 2000.
- [19] H. Yin, Y.-C. Huang, W. Fang and J. Hsieh, "A novel electromagnetic elastomer membrane actuator with a semi-embedded coil," *Sensors and Actuators A*, vol. 139, no. 1-2, pp. 194-202, 2007.
- [20] L. Lagorce and M. Allen, "Magnetic and mechanical properties of micromachined strontium ferrite/polyimide composites," *Journal of Microelectromechanical Systems*, vol. 6, no. 4, pp. 307-312, 1997.
- [21] W. Wang, Z. Yao, J. Chen and J. Fang, "Composite elastic magnet films with hard magnetic features," *Journal of Micromechanics and Microengineering*, vol. 14, no. 10, pp. 1321-1327, 2004.
- [22] C. Yamahata, C. Lotto, E. Al-Assaf and M. Gijs, "A PMMA valveless micropump using electromagnetic actuation," *Microfluidics and Nanofluidics*, vol. 1, no. 3, pp. 197-207, 2005.
- [23] O. Jeong and S. Yang, "Fabrication and test of a thermopneumatic micropump with a

- corrugated p+ diaphragm," *Sensors and Actuators A*, vol. 83, pp. 249-255, 2000.
- [24] S. Zimmermann, J. Frank, D. Liepmann and A. Pissano, "A planar micropump utilizing thermopneumatic actuation and in-plane flap valves," in *17th IEEE International Conference on Micro Electro Mechanical Systems*, 2004.
- [25] A. Olsson, G. Stemme and E. Stemme, "A numerical design study of the valveless diffuser pump using lumped-mass model," *Journal of Micromechanics and Microengineering*, vol. 9, pp. 34-44, 1999.
- [26] J. Smits, "Piezoelectric micropump with three valves working peristaltically," *Sensors and Actuators A*, vol. 21, pp. 203-206, 1990.
- [27] S. Shoji, S. Nakagawa and M. Esashi, "Micropump and Sample Injector for Integrated Chemical Analyzing Systems," *Sensors and Actuators A*, vol. 21, pp. 189- 192, 1990.
- [28] A. Olsson, G. Stemme and E. Stemme, "A valve-less planar fluid pump with 2 pump chambers," *Sensors and Actuators A*, vol. 47, pp. 549-556, 1995.
- [29] A. Olsson, P. Enoksson, G. Stemme and E. Stemme, "A valve-less planar pump isotropically etched in silicon," *Journal of Micromechanics and Microengineering*, vol. 6, pp. 87-91, 1996.
- [30] A. Olsson, Valveless diffuser micropumps, Stockholm: Royal Institute of Technology, 1998.
- [31] K. Yun, I. Cho, J. Bu, C. Kim and E. Yoon, "A surface-tension driven micropump for low-

- voltage and low-power operations," *Journal of Microelectromechanical Systems*, vol. 11, pp. 454-461, 2002.
- [32] J. Berg, R. Anderson, M. Anaya, B. Lahlouh, M. Holtz and T. Dallas, "A two-stage discrete peristaltic micropump," *Sensors and Actuators A*, vol. 104, pp. 6-10, 2003.
- [33] E. Zordan and F. Amirouche, "Design and analysis of a double superimposed chamber valveless MEMS micropump," *Journal of Engineering in Medicine*, vol. 221, no. 2, pp. 143-151, 2007.
- [34] T. Pan, E. Kai, M. Stay, V. Barocas and B. Ziaie, "A magnetically driven PDMS Peristaltic Micropump," in *26th Annual International Conference of the IEEE EMBS*, San Francisco, 2004.
- [35] M. Teymorri and E. Abbaspour-Sani, "A novel electrostatic micromachined pump for drug delivery systems," in *ICSE2002*, Penang, Malaysia, 2002.
- [36] Q. Lin, B. Yang, J. Xie and Y. Tai, "Dynamic simulation of a peristaltic micropump considering coupled fluid flow and structural motion," *Journal of Micromechanics and Microengineering*, vol. 17, no. 2, pp. 220-228, 2007.
- [37] C. Wang and G. Lee, "Pneumatically driven peristaltic micropumps utilizing serpentine-shape channels," *Journal of Micromechanics and Microengineering*, vol. 16, no. 2, pp. 341-348, 2006.
- [38] Y. Yang and H. Liao, "Development and characterization of thermopneumatic peristaltic

- micropumps," *Journal of Micromechanics and Microengineering*, vol. 19, no. 2, 2009.
- [39] N. Nguyen and S. Wereley, *Fundamentals and Applications of Microfluidics*, Norwood: Artech House, 2006, pp. 257-258.
- [40] J. Johnson, *Hydraulics for Engineering Technology*, Upper Saddle River: Prentice-Hall, 1996.
- [41] G. Lemarquand, V. Lemarquand, S. Babic and C. Akyel, "Magnetic Field Created by Thin Wall Solenoids and Axially Magnetized Cylindrical Permanent Magnets," in *PIERS Proceedings*, Moscow, 2009.
- [42] J. Coey, *Magnetism and Magnetic Materials*, New York: Cambridge University Press, 2009.
- [43] S. Babic and C. Akyel, "Improvement in the analytical calculation of the magnetic field produced by permanent magnet rings," *Progress in Electromagnetics Research C*, vol. 5, pp. 71-82, 2008.
- [44] R. Ravaud, G. Lemarquand, V. Lemarquand and C. Depollier, "Discussion about the analytical calculation of the magnetic field created by permanent magnets," *Progress in Electromagnetics Research B*, vol. 11, pp. 281-297, 2009.
- [45] B. Azzerboni, E. Cardelli, M. Raugi, A. Tellini and G. Tina, "Magnetic force calculation between thin coaxial circular coils in air," *Magnetics, IEEE Transactions on*, vol. 29, no. 3, pp. 2090-2094, 1993.
- [46] Z. Ren, "Comparison of different force calculation methods in 3D finite element modeling,"

- IEEE Transactions on Magnetics*, vol. 30, no. 5, pp. 3471-3474, 1994.
- [47] P. Graneau, "Compatibility of the Ampere and Lorentz force laws with the virtual-work concept," *Il Nuovo Cimento B*, vol. 78 B, no. 2, pp. 213-234, 1983.
- [48] J. Gieras and M. Wing, *Permanent Magnet Motor Technology: Design and Applications* Second Edition, New York: Marcel Dekker, 2002.
- [49] H. Knoepfel, *Magnetic Fields: A Comprehensive Theoretical Treatise for Practical Use*, New York: Wiley, 2000.
- [50] P. Ciarlet, *Numerical Methods in Electromagnetics*, New York: Elsevier, 2005.
- [51] I. Jelberg, "Maxwell Stress Tensor "pitfall" Example," [Online]. Available: <http://www.comsol.com/community/exchange/71>. [Accessed 22 November 2009].
- [52] A. Feldstein and P. Turner, "Overflow, Underflow, and Server Loss of Significance in Floating-Point Addition and Subtraction," *IMA Journal of Numerical Analysis*, vol. 6, no. 2, pp. 241-251, 1986.
- [53] J. Fish and Belytschko, *Finite Elements*, West Sussex: John Wiley & Sons Ltd., 2007.
- [54] P. Dario, N. Croce, M. Carrozza and G. Varallo, "A fluid handling system for a chemical microanalyzer," *Journal of Micromechanics and Microengineering*, vol. 6, pp. 95-98, 1996.
- [55] H. Li, D. Roberts, J. Steyn, K. Turner, J. Carretero, O. Yaglioglu, Y. Su, L. Saggere, N. Hagood, S. Spearing and M. Schmidt, "A high frequency high flow rate piezoelectrically driven mems micropump," in *Solid State Sensors and Actuators Workshop*, Hilton Head,

- SC, June 2000.
- [56] K. Junwu, Y. Zhigang, P. Taijiang, C. Guangming and W. Boda, "Design and test of a high-performance piezoelectric micropump for drug delivery," *Sensors and Actuators A*, vol. 121, pp. 156-161, 2005.
- [57] H. Ma, B. Hou, H. Wu, C. Lin, J. Gao and M. Kou, "Development and application of a diaphragm micro-pump with piezoelectric device," *Microsystem Technology*, vol. 14, pp. 1001-1007, 2008.
- [58] M. Zhu, P. Kirby, M. Wacklerle, M. Herz and M. Richter, "Optimization design of multi-material micropump using finite element method," *Sensors and Actuators A*, vol. 149, no. 1, pp. 130-135, 2009.
- [59] S. Santra, P. Holloway and C. Batich, "Fabrication and testing of a magnetically actuated micropump," *Sensors and Actuators B*, vol. 87, pp. 358-364, 2002.
- [60] M. Shen, C. Yamahata and M. Gijs, "Miniaturized PMMA ball-valve micropump with cylindrical electromagnetic actuator," *Microelectronic Engineering*, vol. 85, pp. 1104-1107, 2008.